

# The Magnetic Dipole Moment of the $\Delta^+$ (1232) Resonance

INAUGURALDISSERTATION

Zur  
Erlangung der Würde eines Doktors der Philosophie  
vorgelegt der  
Philosophisch-Naturwissenschaftlichen Fakultät  
der Universität Basel  
von

Bénédicte Boillat

aus Delémont, JU

Basel, 2009.

Genehmigt von der Philosophisch-Naturwissenschaftlichen Fakultät auf Antrag von Prof. Dr. Bernd Krusche und Prof. Dr. Michael Ostrick.

Basel, den 25. März 2008

Prof. Dr. H.- P. Hauri, Dekan

*A Papa, qui saura apprécier ce travail mieux que personne.*

Basel, March 11<sup>th</sup>, 2008.



# Contents

0.1	Abstract . . . . .	12
<b>1</b>	<b>Introduction and Motivation</b>	<b>13</b>
1.1	History of Nuclear Physics . . . . .	13
1.2	WHY and HOW study the $\Delta$ Resonance . . . . .	17
<b>2</b>	<b>Theoretical Background</b>	<b>21</b>
2.1	The Standard Model . . . . .	21
2.1.1	The Quark Model . . . . .	22
2.1.2	The SU(3) Symmetry . . . . .	23
2.1.3	Magnetic Moment of Baryons in SU(3) Symmetry . . . . .	26
2.2	Theoretical Calculations around the $\Delta^+$ Resonance . . . . .	28
2.2.1	The Unitary Model . . . . .	29
2.2.2	The Unitary Model for the $\gamma p \rightarrow \pi^0 p$ Reaction . . . . .	29
2.2.3	Chiral Effective Field Theory Calculations . . . . .	34
<b>3</b>	<b>Experiment Setup</b>	<b>41</b>
3.1	Overview . . . . .	41
3.2	The polarized Photon Beam . . . . .	42
3.2.1	The MAMI polarized Electron Beam . . . . .	42
3.2.2	The linearly and circularly polarized Photon Beam . . . . .	43
3.2.3	The Glasgow Tagger Magnet . . . . .	47
3.3	The Hydrogen Target . . . . .	50
3.4	The Crystal Ball Apparatus . . . . .	51
3.4.1	Overview . . . . .	51
3.4.2	The Crystal Ball Detector . . . . .	51
3.4.3	The Particle Identification Detector . . . . .	53
3.4.4	The Wire Chamber . . . . .	54
3.5	The TAPS Apparatus . . . . .	56
3.5.1	The TAPS Detector . . . . .	56
3.5.2	The TAPS Vetos . . . . .	58
3.6	The Trigger and Electronics System . . . . .	59

3.6.1	The Crystal Ball and Trigger Electronics . . . . .	59
3.6.2	The PID Electronics . . . . .	65
3.6.3	The MWPC Electronics . . . . .	66
3.6.4	The TAPS Electronics . . . . .	67
3.6.5	The TAPS Piggyback . . . . .	68
3.6.6	The Data Acquisition . . . . .	70
3.6.7	Overview of the taken Data . . . . .	71
<b>4</b>	<b>Data Treatment for Analysis</b>	<b>73</b>
4.1	Analysis Software AcqRoot . . . . .	73
4.2	Tagger Data . . . . .	76
4.2.1	Tagger Energy Calibration . . . . .	76
4.2.2	Tagger Time Calibration . . . . .	76
4.3	Crystal Ball Data . . . . .	77
4.3.1	Crystal Ball Energy Calibration . . . . .	77
4.3.2	Crystal Ball Time Calibration . . . . .	78
4.3.3	The PID Calibration . . . . .	79
4.3.4	The Wire Chamber Calibration . . . . .	80
4.4	The TAPS Data . . . . .	80
4.4.1	The TAPS Energy Calibration . . . . .	80
4.4.2	The TAPS Time Calibration . . . . .	81
4.4.3	The Response Measurement and Cosmics Calibration . . . . .	82
4.4.4	The Range Setting . . . . .	85
4.4.5	The Determination of the LED Threshold . . . . .	87
4.4.6	The TAPS Particle Identification . . . . .	87
4.4.7	The Cluster Algorithm . . . . .	89
4.4.8	The Proton Energy Correction . . . . .	91
4.4.9	The Walk Correction . . . . .	93
4.4.10	The Tagger Structure Correction . . . . .	95
<b>5</b>	<b>Analysis</b>	<b>97</b>
5.1	Simulations . . . . .	98
5.1.1	Event Generator . . . . .	98
5.1.2	Detector Reconstruction . . . . .	102
5.1.3	Analysis of simulated Events . . . . .	103
5.2	Channel Identification . . . . .	105
5.2.1	The Data Reduction . . . . .	105
5.2.2	Basis Analysis Requirements and Cuts . . . . .	105
5.2.3	The Subtraction of the Tagger's Randoms . . . . .	106
5.2.4	Single $\pi^0$ Background Channel . . . . .	108
5.2.5	Double $\pi^0$ Background Channel . . . . .	112

5.2.6	The Electromagnetic Background . . . . .	116
5.2.7	The Setup Background . . . . .	117
5.2.8	Overview of the Cut Effects . . . . .	118
5.3	Analysis of the single $\pi^0$ Channel . . . . .	121
5.4	Extraction of Polarisation Variables: <i>The Circular Asymmetry</i> . . . . .	124
5.5	Extractions of Cross Sections . . . . .	126
5.5.1	The Components of the Cross Sections . . . . .	126
5.5.2	Final Background Subtraction . . . . .	129
5.5.3	The Empty Target Runs Subtraction . . . . .	131
5.5.4	Systematic Errors . . . . .	132
<b>6</b>	<b>Results and Discussion</b>	<b>133</b>
6.1	Asymmetries . . . . .	133
6.2	Cross Sections . . . . .	137
6.2.1	The single $\pi^0$ Differential Cross Sections . . . . .	137
6.2.2	The $\gamma p \rightarrow \pi^0 p \gamma'$ Differential Cross Sections . . . . .	139
6.3	Conclusion and Outlook . . . . .	149
6.3.1	Degree of Polarisation for Electron Incoming Beam En- ergy of 570.19 . . . . .	159
6.4	The $\gamma p \rightarrow \pi^0 p$ Differential Cross Sections . . . . .	160
6.4.1	Incoming Photon Beam Energy: 325-375 MeV . . . . .	160
6.4.2	Incoming Photon Beam Energy: 375-425 MeV . . . . .	161
6.4.3	Incoming Photon Beam Energy: 425-475 MeV . . . . .	162
6.5	The $\gamma p \rightarrow \pi^0 p \gamma'$ Angular Differential Cross Sections . . . . .	163
6.5.1	Incoming Photon Beam Energy: 325-375 MeV . . . . .	163
6.5.2	Incoming Photon Beam Energy: 375-425 MeV . . . . .	164
6.5.3	Incoming Photon Beam Energy: 425-475 MeV . . . . .	165
6.6	The $\gamma p \rightarrow \pi^0 p \gamma'$ Energy Differential Cross Sections . . . . .	166
6.6.1	Incoming Photon Beam Energy: 325-375 MeV . . . . .	166
6.6.2	Incoming Photon Beam Energy: 375-425 MeV . . . . .	167
6.6.3	Incoming Photon Beam Energy: 425-475 MeV . . . . .	168
6.7	The R-ratio Differential Cross Sections . . . . .	169
6.7.1	Incoming Photon Beam Energy: 325-375 MeV . . . . .	169
6.7.2	Incoming Photon Beam Energy: 375-425 MeV . . . . .	170
6.7.3	Incoming Photon Beam Energy: 425-475 MeV . . . . .	171





# List of Figures

1.1	J.J. Thomson's Experiment . . . . .	14
1.2	Gold Foil Experiment . . . . .	15
1.3	Nucleon and $\Delta$ in Potential . . . . .	17
1.4	Stern Gerlach Experiment . . . . .	18
1.5	Schematic View of the Studied Channel . . . . .	19
2.1	Particles of Matter . . . . .	22
2.2	Baryon Octet and Decuplet . . . . .	26
2.3	Pion Photoproduction T-matrix . . . . .	29
2.4	Diagrams for the $\gamma p \rightarrow \pi^0 p$ Reaction in the $\Delta$ Resonance Region .	30
2.5	Total Cross Section from Unitary Model for $\gamma p \rightarrow \pi^0 p$ and $\gamma p \rightarrow \pi^+ n$ Reaction . . . . .	31
2.6	Diagrams for the $\gamma p \rightarrow \pi^0 p \gamma'$ Reaction in the $\Delta$ Resonance Region	32
2.7	T-matrix for $\gamma p \rightarrow \pi^0 p \gamma'$ Reaction . . . . .	33
2.8	Energy Differential Cross Section from Unitary Model . . . . .	34
2.9	The Pseudo-scalar Meson Octet . . . . .	36
2.10	Diagrams for $\gamma p \rightarrow \pi^0 p \gamma'$ Reaction in the NLO $\delta$ -expansion . . . .	38
2.11	Results of the Effective Field Theory Calculations . . . . .	39
3.1	Overview of Experimental Setup . . . . .	41
3.2	Racetrack Microtron . . . . .	43
3.3	Bremsstrahlung Momentum Pancake . . . . .	44
3.4	Linear Accelerator . . . . .	45
3.5	Photon Beam Polarization . . . . .	47
3.6	The Glasgow Tagging System . . . . .	48
3.7	Tagger Spectrum . . . . .	48
3.8	Tagging Efficiency . . . . .	50
3.9	The Liquid Hydrogen Target . . . . .	50
3.10	The Crystal Ball Apparatus . . . . .	51
3.11	Crystal Ball Detector . . . . .	52
3.12	PID . . . . .	53

3.13	MWPC	55
3.14	Picture CB + TAPS	56
3.15	BaF <sub>2</sub>	57
3.16	PSA	58
3.17	CB Electronics	60
3.18	SADC Pulse	62
3.19	Trigger	65
3.20	PID Electronics	66
3.21	MWPCS Electronics	67
3.22	TAPS Piggyback	68
4.1	AcquRoot Software Structure	74
4.2	AcquRoot Analyser Structure	75
4.3	CB Energy Calibration	78
4.4	PID Position Calibration	79
4.5	MWPC Calibration	80
4.6	Cosmics Spectrum	81
4.7	TAPS Time Calibration	82
4.8	Mini TAPS	83
4.9	TAPS Response of two Rings	84
4.10	TAPS Response of three Rings	84
4.11	Bloc D in TAPS	86
4.12	LED Threshold Determination	87
4.13	PSA Steps	88
4.14	Time Of Flight	89
4.15	BaF <sub>2</sub> Cluster Energy	90
4.16	BaF <sub>2</sub>	91
4.17	2D Plot for Proton Energy Correction	92
4.18	P3 Fit for Proton Energy Correction	92
4.19	Signal Amplitude Nuisance	93
4.20	Walk Correction1	94
4.21	Walk Correction2	95
4.22	4x4 Tagger Structure Correction	96
5.1	Generated/Real Photon Beam Distribution	99
5.2	Energy and $\theta$ of generated $\pi^0$	100
5.3	Energy and $\theta$ of generated $p/\gamma'$	101
5.4	Reconstructed Setup	103
5.5	$\pi^0$ Invariant Mass	106
5.6	Random Substraction	107
5.7	Single $\pi^0$ Cross Section	108

5.8	Opening Angles between Photon Pairs . . . . .	110
5.9	Time Differences between $\gamma s'$ . . . . .	110
5.10	Missing Mass Proton . . . . .	111
5.11	Energy of the Radiative Photon . . . . .	112
5.12	Double $\pi^0$ Cross Section . . . . .	113
5.13	Missing Mass A and B . . . . .	114
5.14	Comparison Missing Mass C Data/double $\pi^0$ simulations . . . . .	114
5.15	$M_{\pi^0\gamma'}$ . . . . .	115
5.16	Energy Balance . . . . .	116
5.17	Polar Angle of the Radiative Photon . . . . .	117
5.18	Polar Angle of the Proton . . . . .	117
5.19	Final MMPi0Gamma, combined . . . . .	121
5.20	Cuts of the single $\pi^0$ Analysis . . . . .	122
5.21	$\theta$ angle of the $\pi^0$ in CM in $\gamma p \rightarrow \pi^0 p$ . . . . .	123
5.22	Degree of Polarisation . . . . .	125
5.23	Angle Definition for Circular Asymmetry . . . . .	125
5.24	Detector Efficiency . . . . .	127
5.25	Detector Efficiency single $\pi^0$ channel . . . . .	128
5.26	$\gamma p \rightarrow \pi^0\pi^0 p$ background "Efficiency" . . . . .	130
5.27	Empty target DCS with fit . . . . .	131
6.1	Circular Asymmetry on $\phi$ angle . . . . .	134
6.2	Circular Asymmetry on $\phi$ angle . . . . .	134
6.3	Circular Asymmetry on $\phi$ angle . . . . .	135
6.4	Circular Asymmetry on $\phi$ angle . . . . .	135
6.5	Angular DCS Single $\pi^0$ , 350 MeV . . . . .	137
6.6	Angular DCS Single $\pi^0$ , 400 MeV . . . . .	138
6.7	Angular DCS Single $\pi^0$ , 450 MeV . . . . .	138
6.8	Angular Differential Cross Sections . . . . .	139
6.9	Angular Differential Cross Sections . . . . .	140
6.10	Energy Differential Cross Sections . . . . .	141
6.11	Energy Differential Cross Sections . . . . .	142
6.12	New NLO Diagrams for $\gamma p \rightarrow \pi^0 p \gamma'$ reaction in [Pas07] . . . . .	143
6.13	Rescattering Loops in [Pas07] . . . . .	143
6.14	Weight Function for $\sigma^0$ . . . . .	145
6.15	Ratio Differential Cross Sections . . . . .	147
6.16	Ratio Differential Cross Sections . . . . .	148
6.17	New NLO Diagrams for $\gamma p \rightarrow \pi^0 p$ reaction in [Pas07] . . . . .	148
6.18	$N^*$ Resonances . . . . .	150



# List of Tables

1.1	Table of Theoretical Predictions in 2001 . . . . .	20
2.1	The four Interactions of the Standard Model . . . . .	21
5.1	Nomenclature of the Reaction Products . . . . .	97

## 0.1 Abstract

The magnetic dipole moment of the  $\Delta^+(1232)$  resonance is a fundamental observable and provides a stringent test of baryons structure calculations. A pioneering measurement was performed in year 2002 and delivered a result of  $(2.7 \pm 2.2(\text{exp}))\mu_N$ <sup>1</sup>. However, a higher precision is needed to allow a clear selection between different structure models.

A new dedicated experiment using the Crystal Ball and TAPS detectors has been performed 2004/2005 at MAMI, offering a superior  $4\pi$ -acceptance and particle identification.

Exploiting the circular and linear polarized photon beam, two polarization observables  $\Sigma$  and  $\Sigma_{\text{circ}}$  and in addition differential cross sections will be extracted. The progress in the development of the theoretical calculations<sup>2 3 4</sup> allows a well directed interpretation of the data in order to describe the reaction  $\gamma p \rightarrow \pi^0 \gamma' p$  and to extract the magnetic dipole moment. Preliminary results will be presented.

---

<sup>1</sup>M. Kotulla et al., Phys. Rev Lett. 89:272001, 2002

<sup>2</sup>W.T. Chiang, M. Vanderhaeghen, S.N. Yang, D. Drechsel, Phys. Rev. C71:015204, 2005

<sup>3</sup>A.I. Machavariani, Amand Faessler Phys. Rev. C72:024002, 2005

<sup>4</sup>V. Pascalutsa, M. Vanderhaeghen, Phys. Rev. Lett. 94:102003, 2005

# Chapter 1

## Introduction and Motivation

### 1.1 History of Nuclear Physics

Looking backwards into history, physics always tried to understand smaller and smaller structure of our world, this leading to *nuclear and particle physics*.

Let us start in 1543, period of the *Scientific Revolution*, which corresponds to an important turn from ancient to classical physics and to the start of the detachment of physics from philosophy.

The scientific revolution begins with the publication of Copernicus *The Revolution of the Celestial Spheres*. One of the multiple outputs of this revolution is the replacement of the aristotelian *Air-Earth-Fire-Aether* theory by the rival *Atomistic* or *Corpuscular* theory. Another important point of the scientific revolution is the beginning of "experimentations" as, up to this time, only a natural approach has been used, not inducing any artificial circumstances. The interest for mathematics also grows at this time, in the view that mathematics may be an important tool to progress in physics. The best known physicists of the scientific revolution are Copernicus, Galileo Galilei - who had already mathematically analysed his astronomical observations - , Johannes Kepler with his laws of planetary motions and of course Isaac Newton with his development of calculus and his advanced theory of universal gravitation.

The XVIII<sup>th</sup> century is the time of the thermodynamics' progress with the works of Thomas Young and David Bernouilli.

The first step towards nuclear physics is undertaken by John Dalton's thoughts about the existence of atoms. He proposes that chemical combination consists in the interactions of *Atoms* with definite and characteristic weight. He also writes

the very first table of atomic weights and the famous *Law of Multiple Proportions* describing the chemical analysis (stoichiometry):



Dalton's theory is developed and partially corrected in 1811 by Amedes Avogadro, who offers more accurate estimates of atomic masses and asserts the difference between *Molecules* and *Atoms*.

Atoms are considered as the smallest possible division of matter until 1897, when J.J. Thomson discovers the electron through his work on cathode ray tubes (see fig 1.1).

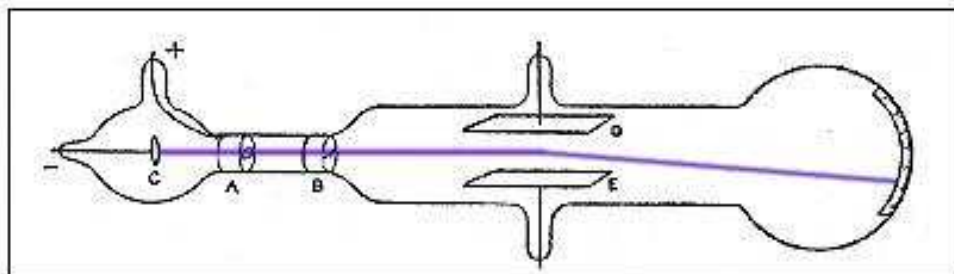


Figure 1.1: Cathode ray tube in which Thomson observed the deflection of cathode rays by an electric field

Thomson concludes that the rays, rather than being waves, are composed of negatively charged particles he called *Corpuscles*, that are the building blocs of the atom. As the atom itself is known to be neutral, Thomson proposes the *Plum-Pudding Model*, where the negative corpuscles are distributed in a uniform sea of positive charges.

The atom picture remains the same until 1909, when Ernest Rutherford suggests the existence of the *nucleus*, in accordance with the results of the gold foil experiment (see fig 1.2) performed by Hans Geiger and Ernest Marsden. This experiment consists in shooting  $\alpha$  particles through a gold sheet. Considering the small electron mass, the high momentum of the  $\alpha$  particles and the approach of the plum pudding model, one expects all the  $\alpha$ s, either passing through with only minimal deflection, or being absorbed. The result shows a small fraction of the  $\alpha$  particles being strongly deflected. Thereafter, Rutherford proposes the planetary-like model of the atom, where a mass of compact positive charge, the *nucleus*, is surrounded by orbit electrons (see fig.



1.2, RIGHT).

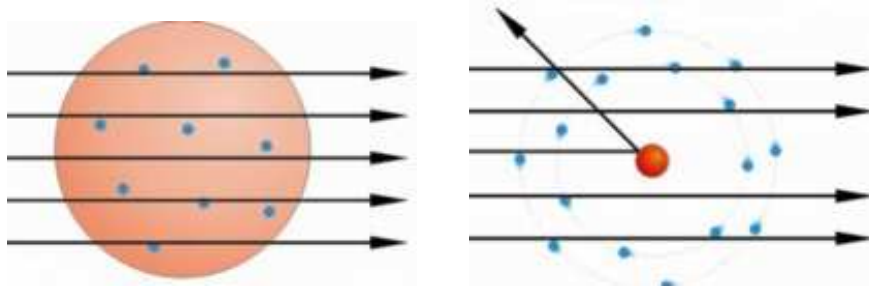


Figure 1.2: LEFT: Expected result deduced from the plum model, RIGHT: Observed results leading to the existence of an atom *nucleus*

Rutherford confirms the existence of the proton in 1918: he bombards nitrogen gas with  $\alpha$  particles and observes that hydrogen nuclei are emitted from the gas. He concludes that they are "provided" by the nitrogen nuclei and, combining this information with the observed fact, that many atom masses are multiples of the hydrogen mass, he proposes that hydrogen nuclei are singular particles and a basic constituent of all atomic nuclei. He also notices that the nuclear mass of the atoms is higher than the sum of their proton masses and thus brings the idea of the existence of *Neutrons*.

The discovery of the neutron is due to James Chadwick, who received for this work the Nobel prize in 1935.

The following years, Einstein's equivalence of mass and energy is demonstrated with the atomic bomb.

After the invention of the cyclotron by Ernest O. Lawrence in the 30's, the postwar research is known as the "Big Science" period, mainly concentrated on building expensive accelerators subsidized by the governments. The therewith performed experiments bring the discovery of numerous new particles not observable in the nature. To better understand and classify these particles, the *Standard Model* is proposed in the 60's, based on Gell Mann's *Quark Model*.

The quark model divides the hadrons <sup>1</sup> in two groups: the *mesons* made of two quarks, like the pions, and the *baryons* made of three constituent quarks like the nucleons. The different particles built with the same constituent are then the different possible states of these quarks in the nucleus potential, usual-

---

<sup>1</sup>particles made of quarks

ly associated to a harmonic oscillator potential. In addition to the quantum numbers delivered by the quantum states, some quantum numbers have been introduced to make possible the classification of all the known particles.

Considering the several groups of particles and the number of their components, (pions: 3, nucleons: 2,  $\Delta$ s: 4) the quantum number *Isospin*:  $I$  has been introduced in the quark model in analogy to the spin. The particles of the same group have the same isospin  $I$ , but differ in the  $I_z$  value of the isospin which gives the orientation of the isospin vector in space. The number of possible orientations  $2 \times I + 1$  gives the number of particles in the group of isospin  $\vec{I}$ . The "visible" difference between the group participants is, however, seen by the charge  $Q$  that directly derives from  $I_z$  via the relation:

$$Q = (I_z + \frac{1}{2}A)e$$

The quantum number  $A$ , called *baryon number*, has a value of 1 for baryons, -1 for anti-baryons and 0 for mesons.

The use of the upper information allows the description of the nucleon's doublet :

$$I = \frac{1}{2}, I_z = \pm \frac{1}{2}, A = 1, Q = \begin{cases} (+\frac{1}{2} + \frac{1}{2})e & \text{for p} \\ (-\frac{1}{2} + \frac{1}{2})e & \text{for n} \end{cases}$$

Similarly the  $\Delta$ s' group has an isospin of  $\frac{3}{2}$  which provides  $2 \cdot \frac{3}{2} + 1 = 4$  states in the group:

$$I = \frac{3}{2}, I_z = \pm \frac{3}{2}, \pm \frac{1}{2}, A = 1, Q = \begin{cases} (+\frac{3}{2} + \frac{1}{2})e & \text{for } \Delta^{++} \\ (+\frac{1}{2} + \frac{1}{2})e & \text{for } \Delta^+ \\ (-\frac{1}{2} + \frac{1}{2})e & \text{for } \Delta^0 \\ (-\frac{3}{2} + \frac{1}{2})e & \text{for } \Delta^- \end{cases}$$

Nucleons and  $\Delta$ s containing the same constituent quarks *up* and *down*, we here already see the several state possibilities offered by the quark model.

The usual notation used for the states of a particle combines the different quantum numbers and looks like the following for the nucleon:

$$\begin{aligned} S &= \frac{1}{2}, \text{ the spin} \\ L^\pi &= 0^+, \text{ the angular momentum with the parity } \pi \\ J^\pi &= \frac{1}{2}^+, \text{ the spin-angular momentum combination with} \\ &|L - S| \leq J \leq L + S \text{ and the parity } \pi \\ \text{The parity } \pi &\text{ given via } \pi = (-1)^l \end{aligned}$$

Resonances are written with the following notation:

$$L_{2,I2,J}(M)$$

$L$  is the orbital angular momentum of the nucleon - pion (or other pseudoscalar meson) pair from the decay of the resonance ( $S = 0, P = 1$ , etc.).  $I$  and  $J$  are as described before,  $M$  delivers the mass of the resonance in  $\text{MeV}/c^2$ .

Thus the  $P_{33}(1232)$  resonance has an isospin of  $I = 3/2$ , a spin-angular momentum of  $J = 3/2$  and the angular momentum between its decay products, i.e. the  $\pi^0$  and the proton equals to 1. Its mass is 1232 MeV.

## 1.2 WHY and HOW study the $\Delta$ Resonance

If we consider the quarks and quantum numbers of the  $\Delta$  resonance ( $P_{33}$ ) delivered by the quark model, we notice that the latter is the nearest "cousin" of the building blocs of our world: the **nucleons**.

Figure 1.3 shows a potential view of this cousinhood, the  $P_{33}$  reached from the nucleon by a simple spin flip (see fig. 1.3).

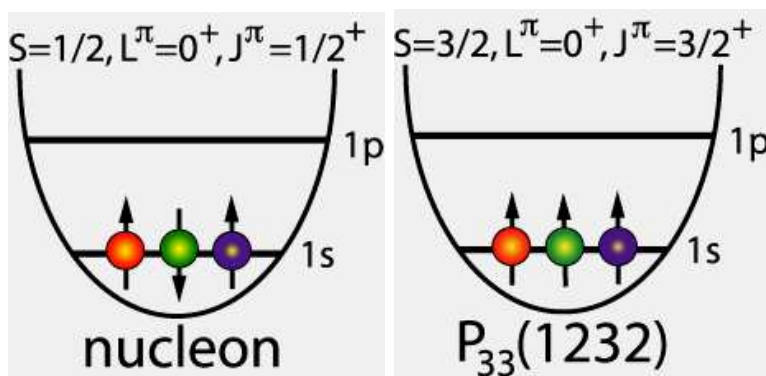


Figure 1.3: Potential view of the Nucleon and the  $\Delta$

It appears therefore as logical, while the nucleons' properties are nowadays well known, to continue the research on their excited states, the nearest ones: The  $\Delta$  Resonances. The present work focuses on the  $\Delta^+$  resonance, the first excited state of the proton.

The  $\Delta$  has been discovered in 1952 by the Fermi's group at Chicago University/USA. At this time, many scattering experiments are performed with,

among others, the pion beam delivered by the Chicago's 450 MeV synchrotron. Fermi's article *Total Cross Section of Positive Pions in Hydrogen* reports a surprising result: By scattering  $\pi^+$  on the proton, an unforeseen enhancement in the cross section is observed, which can be explained with the presence of the  $\Delta$  resonance. Thenceforward, many new resonances have been discovered. Theorists and experimentalists have then been working hand in hand, the theorists to deliver the best predictions, the experimentalists to provide trustable measurements of the  $\Delta$ 's static properties. The mass and the mean lifetime of our  $\Delta^+$  are well known today:

$$t_{\Delta^+} = 6 \times 10^{-24} \text{sec} \quad m_{\Delta^+} = 1232 \text{ MeV}/c^2$$

An additional and especially interesting variable to investigate is its *Dipole Magnetic Moment*  $\mu_{\Delta^+}$ .

The *Dipole Magnetic Moment* is an important experimental variable as already shown in the physics history: The measurement of the magnetic dipole of the proton  $\mu_p$  by Stern and Gerlach in 1933 showed discrepancy with the theoretical expected value from Dirac:

$$\mu_p^{Dirac} = \frac{e}{2m_p} =: \mu_N \quad \text{and} \quad \mu_n^{Dirac} = 0\mu_N$$

The results of this experiment:  $\mu_p^{exp} = 2.75\mu_N$  and  $\mu_n^{exp} = -1.91\mu_N$  opened the door to the **substructure of the nucleon**.

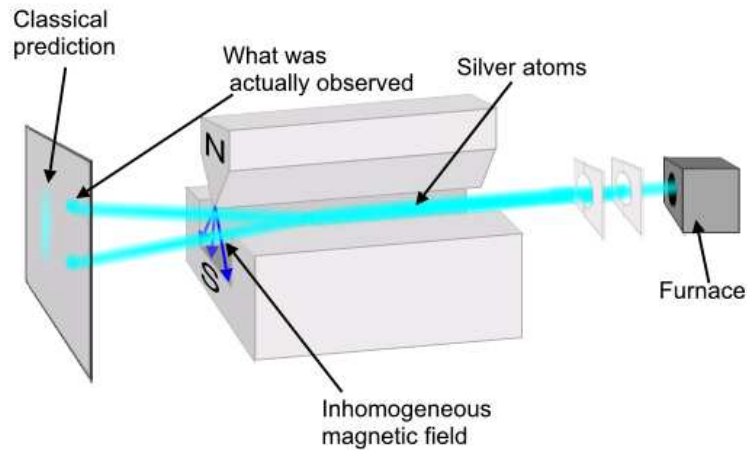
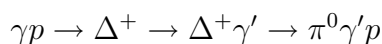


Figure 1.4: Stern Gerlach Experiment. Determination of the magnetic moment of the proton via spin deflection in an inhomogenous field:  $H_z = \mu_z \cdot \frac{\partial B}{\partial z}$

Later, the usual way to measure dipole moments becomes the spin precession in a homogenous magnetic field. In our case, this way to proceed is not possible, as the  $\Delta$  has a too short lifetime to deliver a precession frequency. The idea of the present experiment is to use the short lifetime (or broad width) of the  $\Delta$  to approach its spin information. A particle with a large width offers the opportunity of reactions inside "itself", typically an electromagnetic transition  $\Delta \rightarrow \Delta\gamma'$ . Considering the parity of the multipole emissions  $El : P = (-1)^l$  and  $Ml : P = (-1)^{l+1}$  for the parity conservation, the triangle angular momentum conservation  $|J_1 - J_2| \leq l \leq |J_1 + J_2|$  and  $J_{\Delta^+}^P = \frac{3}{2}^+$ , only M1, M3 and E2 are allowed in this case and can be in principle measured. However, the M1 is the strongest one thanks to its lowest order. Due to the fact that time reversal invariance forbids E2 transitions between the same two states, E2 is strongly suppressed.

In short, the goal of the present work is the study of the reaction:



where  $\gamma'$  is a radiative photon emitted within the width of the  $\Delta^+$  resonance.

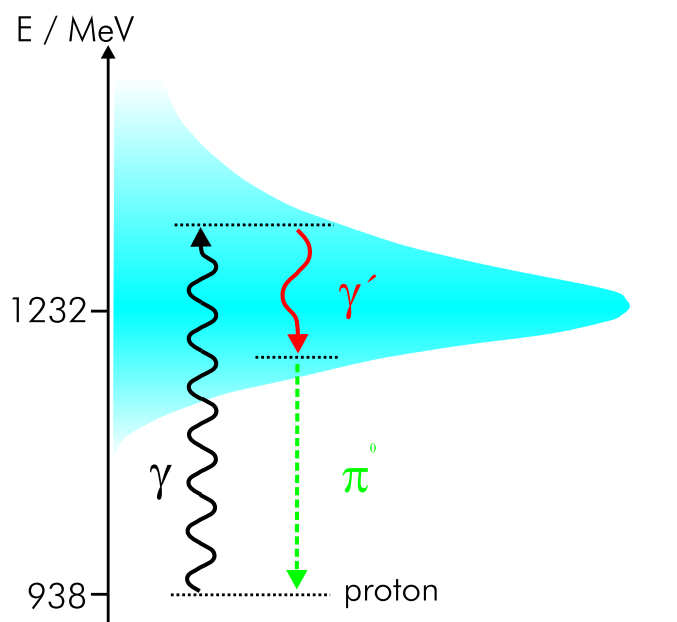


Figure 1.5: Schematic View of the studied channel:  $\gamma p \rightarrow \Delta^+ \rightarrow \Delta^+ \gamma' \rightarrow \pi^0 \gamma' p$

A first pioneer measurement of the  $\Delta^+$  magnetic dipole moment has been

performed by Martin Kotulla [Kot01]. At that time, however, the provided statistics was too low (too large error bars) to allow any prediction about the fiability of the theoretical models (see table 1.1 below).

Model	$\mu_{\Delta^+}/\mu_N$
Experiment [Kot01]	$2.7 \pm 1.7 \pm \sigma_{theo}$
SU(3) $\mu_{\Delta} = Q_{\Delta} \cdot \mu_p$	2.79
RQM [Sch93]	2.38
Lattice QCD [Lei92]	$2.5 \pm 0.3$
$\chi$ PT [But94]	$2.1 \pm 0.2$
$\chi$ QSM [Kim98]	2.19
LCQSR [Ali00]	$2.1 \pm 0.4$

Table 1.1: Result of the first measurement of the  $\Delta^+$ 's MDM in comparison to some theoretical predictions. (RQM: Relativistic Quark Model,  $\chi$  PT : Chiral Perturbation Theory,  $\chi$  QSM: Chiral Quark Soliton Model, LCQSR: Light Cone QCD Sum Rules)

This measurement has nevertheless shown that the method of studying this specific channel for the determination of the  $\Delta^+$  magnetic dipole moment is promising. It has been therefore decided to repeat this experiment with a much higher statistics and detectors, covering a much larger solid angle leading to **the present experiment**.

# Chapter 2

## Theoretical Background

### 2.1 The Standard Model

The *Standard Model* of particle physics is a theory describing three of the four fundamental interactions in our world listed in the table below:

Interaction	Source	Mediators	Rel. Strength	Range [m]
Strong	Colour Charge	Gluons	$10^{38}$	$10^{-15}$
Electromagnetic	Electric Charge	Photon	$10^{36}$	inf
Weak	Weak Charge	$W^{\pm}, Z^0$	$10^{25}$	$10^{-17}$
Gravitation	Mass	Gravitons	one	$\infty$

Table 2.1: The four interactions of the Standard Model and their properties

The quantum mechanical view of these three fundamental forces (excluding gravity) is, that particles of matter (fermions) interact with each other using their specific charges (interaction source) and exchanging gauge bosons (mediators). For example, the electromagnetic interaction only happens between electrically charged particles, by exchanging photons. Similarly, the strong interaction takes place through gluon exchange, between particles carrying the colour charge, i.e. quarks and gluons (see table 2.1).

The particles of matter of our standard model are spin  $1/2$  particles (fermions) and are of course elementary. They are divided in two main groups: the *Leptons* which do not carry the colour charge and the *Quarks*. Their properties are summarized in figure 2.1.

Leptons $spin = 1/2$			Quarks $spin = 1/2$		
Flavor	Mass $GeV/c^2$	Electric charge	Flavor	Approx. Mass $GeV/c^2$	Electric charge
$\nu_e$ electron neutrino	$<1 \times 10^{-8}$	0	<b>u</b> up	0.003	2/3
<b>e</b> electron	0.000511	-1	<b>d</b> down	0.006	-1/3
$\nu_\mu$ muon neutrino	$<0.0002$	0	<b>c</b> charm	1.3	2/3
<b><math>\mu</math></b> muon	0.106	-1	<b>s</b> strange	0.1	-1/3
$\nu_\tau$ tau neutrino	$<0.02$	0	<b>t</b> top	175	2/3
<b><math>\tau</math></b> tau	1.7771	-1	<b>b</b> bottom	4.3	-1/3

Figure 2.1: Particles of Matter

We further concentrate our study on the quarks, as the  $\Delta$  resonance is composed of three of them.

### 2.1.1 The Quark Model

The quark model is a classification scheme of hadrons based on their **valence quarks**, i.e. it does not consider the influence provided by the *sea quarks* and the *gluons*. Each hadron is defined by its own "ID", which is a combination of *quantum numbers*. The latter derive from the Poincaré symmetry<sup>1</sup> and are collected in the form  $J^{PC}$ , where  $J$  is the angular momentum,  $P$  the intrinsic parity and  $C$  the charge conjugation parity. Hadrons may also carry additional, so called *flavour* quantum numbers, like the isospin  $I$  or the strangeness  $S$ .

The resulting quantum numbers of a hadron are obtained by the combination of the quantum number of its valence quarks. Note that antiquarks have

<sup>1</sup>full symmetry including translations, rotations, boosts



the opposite quantum numbers of their corresponding quark.

The hadrons are divided in two groups:

- The **mesons**, made of a valence quark-antiquark pairs, are strong interacting *bosons*. A typical meson showing up in the studied reaction of this work is the pion  $\pi^0$ .
- The **baryons**, composed of three quarks are strongly interacting *fermions*. The baryons carry an additive quantum number: the baryon number "B", defined as equivalent to  $\frac{1}{3}$  for each quark and thus delivering  $B = 1$  for hadrons. (Of course  $B = \frac{1}{3} + (-\frac{1}{3}) = 0$  for the mesons).

Excited baryon or meson states are known as resonances, due to their short lifetime and accordingly large width. Our  $\Delta^+$  resonance is an excited state of the famous baryon proton!

The mathematical method to reach the quark model classification and the resulting hadrons (via their quantum numbers) is the *special unitary group of degree n*. This method is developed below for  $n=3$ , i.e. in the  $SU(3)$  symmetry.

### 2.1.2 The SU(3) Symmetry

The SU(3) symmetry gives a simple approach of determining the numerous baryon wave functions from their three valence quarks.

The total wave function  $\Psi$  of the baryons is built of "fractional wave functions" relating to a specific baryon's property:

$$\Psi = \xi(\text{position})\phi(\text{colour})\chi(\text{spin})\zeta(\text{flavour}) \quad (2.1)$$

The fact that baryons are made of 3 fermions (the quarks) and that up and down quarks are seen in the isospin form as identical particles (only different  $I_z$ ), their total wave function  $\Psi$  has to be *antisymmetric* for permutation. Keeping this goal in mind, we look at the different possibilities offered by the fraction wave functions:

1. The position wave function  $\xi$  is for the ground state, where no orbital momentum is involved, *symmetric*
2. The colour wave function  $\phi$  is restrained by the condition that all the hadrons are colour neutral. Therefore remains only one single combination which will be the same for all baryons:

$$\phi(\text{colour}) = \frac{1}{\sqrt{6}}(rgb + gbr + brg - rgb - bgr - grb), \text{antisymmetric}$$

3. The spin wave function  $\chi$  has to be considered separately for the two possible resulting spin values based on three quarks of spin 1/2:
  - $J = \frac{3}{2}$ , the three spins are parallel to each other. The function is *symmetric*
  - $J = \frac{1}{2}$ . This case is more difficult to treat, as for  $J = \frac{1}{2}$ , the spin wave function  $\chi$  does not have any defined symmetry by permutation of two quarks. See e.g. the case:

$$\frac{1}{\sqrt{2}}(\uparrow\downarrow - \downarrow\uparrow)\uparrow \quad (2.2)$$

This wave function behaves differently depending which quarks are permuted. It is according to this *mixed symmetric*

4. The flavour wave function  $\zeta$  based on three flavours (up, down, strange) offers  $3^3 = 27$  possibilities. 10 of them are *symmetric* by permutation, one is *antisymmetric* and the last 16 are *mixed symmetric*. Below the symmetric ones, building a decuplet:

$$\begin{aligned} ddd & \quad \frac{1}{\sqrt{3}}(ddu + udd + dud) & \quad \frac{1}{\sqrt{3}}(duu + udu + uud) & \quad uuu \\ & \quad \frac{1}{\sqrt{3}}(dds + sdd + dsd) & \quad \frac{1}{\sqrt{3}}(dsu + uds + sud) & \quad \frac{1}{\sqrt{3}}(uus + suu + usu) \\ & \quad \frac{1}{\sqrt{3}}(dss + sds + ssd) & \quad \frac{1}{\sqrt{3}}(sus + ssu + uss) \\ & & & \quad sss \end{aligned} \quad (2.3)$$

The singlet antisymmetric function:

$$\frac{1}{\sqrt{6}}(dsu + +uds + sud - usd - sdu - dus) \quad (2.4)$$

These k-plets of the wave flavour function can be written in the notion of group theory as:

$$3 \otimes 3 \otimes 3 = 10 \oplus 8 \oplus 8 \oplus 1 = 27 \quad (2.5)$$

Using the different 1., 2., 3., 4. possibilities, we should find the combinations that lead to an antisymmetric total wave function  $\Psi$ . As the position and colour wave functions are the same for all baryons and build together a antisymmetric function, we need a spin and flavour symmetric combination.

1. For the spin  $J = \frac{3}{2}$  baryons,  $\chi(\text{spin})$  is symmetric  $\Rightarrow \zeta(\text{flavour})$  must be symmetric  $\Rightarrow \text{flavour decuplet}$
2. For the spin  $J = \frac{1}{2}$  baryons,  $\chi(\text{spin})$  is mixed symmetric  $\Rightarrow \zeta(\text{flavour})$  also mixed symmetric  $\Rightarrow \text{flavour octet}$

As example the spin-flavour wave function of the proton:

$$\chi\zeta_p = \frac{1}{\sqrt{18}}(2|u \uparrow u \uparrow d \downarrow\rangle - |u \uparrow u \downarrow d \uparrow\rangle - |u \downarrow u \uparrow d \uparrow\rangle) + \text{for each two permutations} \quad (2.6)$$

The spin-flavour wave function of the neutron is obtained by exchanging the **u** and **d** quarks in the proton state.

The baryons classification resulting from the SU(3) is shown below, with the flavour decuplet (notice the corresponding state configuration of formula 2.3) and the famous octet containing the nucleons. Note the presence of the additional information like the strangeness quantum number  $s$  and the charge  $q$ :

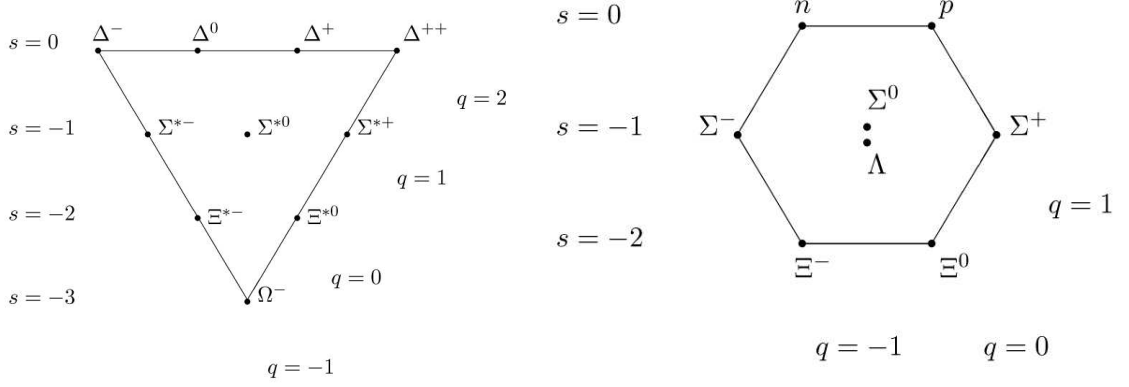


Figure 2.2: flavour decuplet ( $J = \frac{3}{2}$ ) and octet ( $J = \frac{1}{2}$ ) of the baryon SU(3) classification

The SU(3) symmetry can be extended to SU(6) by considering spin and flavour together in one degree of freedom. Two possible spin directions combined with three quark flavours lead to the  $n = 6$  dimension of the group.

### 2.1.3 Magnetic Moment of Baryons in SU(3) Symmetry

The magnetic moments of the baryons can be determined, in absence of orbital angular momentum, by building the sum of the magnetic moments of the three constituent quarks:

$$\vec{\mu}_B = \vec{\mu}_1 + \vec{\mu}_2 + \vec{\mu}_3 \quad (2.7)$$

For the spin 1/2 particles like our constituent quarks, we obtain from the Dirac theory:

$$\vec{\mu} = \frac{q}{2m} \cdot \vec{\sigma} \Rightarrow \mu = \pm \frac{q}{2m} \quad (2.8)$$

$q$  is the charge and  $m$  the mass of the quark. The latter parameters depend only on the spin and flavour wave function, so that we use for the determination of  $\mu$  of baryons only the  $\chi(\text{spin})$  and  $\zeta(\text{flavour})$  part of  $\Psi$ . Example in case

of the proton:

$$\mu_p = \langle \Psi_p | \vec{\mu}_p | \Psi_p \rangle = \sum_i \langle \chi_{\zeta_p} \uparrow | (\vec{\mu}_i)_z | \chi_{\zeta_p} \uparrow \rangle \quad (2.9)$$

Applying this to the proton (and neutron) spin-flavour function of the last chapter, the resulting magnetic moment is:

$$\begin{aligned} \mu_p &= \frac{1}{18}(8\mu_u - 4\mu_d + 0\mu_u + \mu_d) \cdot 3 = \frac{4}{3}\mu_u - \frac{1}{3}\mu_d \\ \mu_n &= \frac{4}{3}\mu_d - \frac{1}{3}\mu_u \end{aligned} \quad (2.10)$$

The factor three represents the permutations.

With the following quarks masses:  $m_u = 338 \text{ MeV}$ ,  $m_d = 322 \text{ MeV}$  and  $m_s = 510 \text{ MeV}$ , we obtain for the quarks magnetic moments:

$\mu_u = 1.852 \mu_N$ ,  $\mu_d = -0.972 \mu_N$  and  $\mu_s = -0.613 \mu_N$ , where  $\mu_N = \frac{e\hbar}{2m_p}$  is the *nuclear magneton*. Applying this further to determine the proton and the neutron, it results:

$$\begin{aligned} \mu_p &= \frac{4}{3} \cdot 1.852 - \frac{1}{3} \cdot (-0.972) \mu_N = 2.145 \mu_N, \mu_p(\text{measured}) = 2.793 \mu_N \\ \mu_n &= \frac{4}{3} \cdot (-0.972) - \frac{1}{3} \cdot 1.852 = -1.913 \mu_N, \mu_n(\text{measured}) = -1.913 \mu_N \end{aligned} \quad (2.11)$$

Considering their rough bases, the predictions of the SU(3)/SU(6) are not so far from the experimental values.

The most interesting value for this work is the theoretical evaluation of the magnetic moments of the decuplet baryons ( $J = \frac{3}{2}$ ) and especially the  $\Delta$ s.

By locating them in the decuplet of figure 2.2 and taking the corresponding wave function out of equation 2.3, we obtain:

$$\begin{aligned} \mu_{\Delta^{++}} &= 3\mu_u = 5.556 \mu_N \\ \mu_{\Delta^+} &= 2\mu_u + \mu_d = 2.732 \mu_N \\ \mu_{\Delta^0} &= \mu_u + 2\mu_d = -0.092 \mu_N \\ \mu_{\Delta^-} &= 3\mu_d = -2.916 \mu_N \end{aligned} \quad (2.12)$$

Remembering the  $\mu_{\Delta^+}$  experimental determination of Martin Kotulla's pioneer measurement:  $2.7 \pm 1.7 \pm \sigma_{theo}$ , the discrepancy remains reasonable.

## 2.2 Theoretical Calculations around the $\Delta^+$ Resonance

The theoretical calculations on the  $\Delta^+$ 's magnetic dipole moments have been improved in the last years and performed at different places and by different groups. Some published articles on the subject:

- *Unitary Model* from Chiang, Vanderhaegen, Yang, Drechsel [Chi05].
- *Chiral effective field theory calculations* from Pascalutsa and Vanderhaegen [Pas05].
- *Soft photon theorem and the magnetic moment of the  $\Delta$  resonance* from A.I. Machavariani and Amand Faessler [Mac07].
- *Covariant baryon charge radii and magnetic moments in a chiral constituent-quark model* from K. Berger, R. F. Wagenbrunn, and W. Plessas [Ber04].

Here, the two first theoretical calculations will be discussed.

We have to make the difference between the *Unitary Model* and the *Chiral effective field theory calculations*, the first one being a "model" using experimental data to extract coupling constants and the second one is a model-independent analysis of the  $\gamma p \rightarrow \pi^0 p \gamma'$  reaction, within the framework of chiral effective field theory.

At this stage, we note the following important fact:

As the extraction of the  $\mu_{\Delta^+}$  can exclusively be done via the use of theoretical calculations, one expects them to be as near as possible to the reality, i.e they should take into account as many *background reactions* as possible. By *background reactions*, we mean all reactions other than the interesting one, starting from a  $\gamma p$  state and ending with a  $\pi^0 \gamma' p$  as there is no experimental way to get rid of them. Another important feature expected from the theoretical calculations is the consideration of *rescattering reactions*, like typically rescattering loops.

As shown in the next two parts, large improvements of these goals have been

reached in recent theoretical works.

### 2.2.1 The Unitary Model

The basic idea of the *unitary model* is to start with the description of a well known channel:  $\gamma p \rightarrow \pi^0 p$  and then "couple" a radiative photon therein to lead to the description of the wanted  $\gamma p \rightarrow \pi^0 p \gamma'$  reaction. The exhaustive description of the  $\gamma p \rightarrow \pi^0 p$  reaction is reached by the use of experimental data providing the numerous coupling constants needed.

The application of the unitary model on the  $\gamma p \rightarrow \pi^0 p \gamma'$  reaction in the  $\Delta$  resonance region proceeds in two steps:

1. Description of the  $\gamma p \rightarrow \pi^0 p$  reaction in a unitary model and fit on experimental data to extract all the parameters of the strong interaction.
2. Adaptation of the unitary model of 1. to the  $\gamma p \rightarrow \pi^0 p \gamma'$  reaction in the  $\Delta$  resonance region.

### 2.2.2 The Unitary Model for the $\gamma p \rightarrow \pi^0 p$ Reaction

The description of the reaction  $\gamma p \rightarrow \pi^0 p$  in a unitary model is obtained with a transition potential derived from an effective Lagrangian with Born terms and vector meson exchange, in addition to the  $\Delta$  excitation mechanism. Thus, the unitarity is reached by the explicit inclusion of the final states  $\pi N$  interactions. The T-matrix is divided in two terms as shown on fig 2.3:

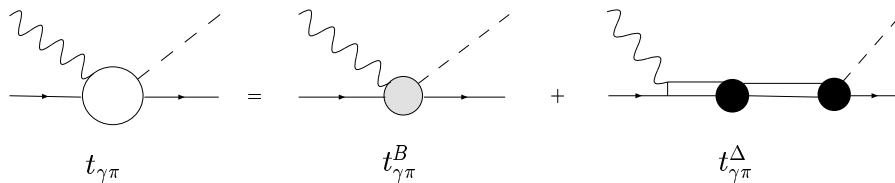


Figure 2.3: schematic view of pion photoproduction T-matrix

The corresponding transition potential  $v_{\gamma\pi}$  contains the two terms  $v_{\pi}^{\Delta}$  and  $v_{\gamma\pi}^B$ , where  $v_{\pi}^{\Delta}$  corresponds to the resonance contribution  $\gamma p \rightarrow \Delta \rightarrow \pi N$  and  $v_{\gamma\pi}^B$  describes the background to be derived from an effective Lagrangian.

Diagrams contributing and taken into account for the  $\gamma p \rightarrow \pi^0 p$  reaction in the  $\Delta$  resonance region are collected in figure 2.4.

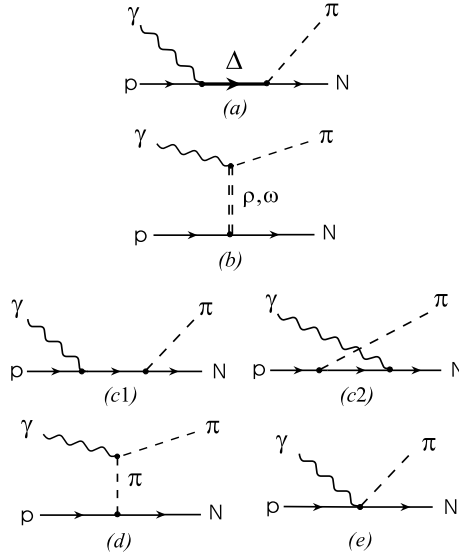


Figure 2.4: diagrams for the  $\gamma p \rightarrow \pi^0 p$  reaction in the  $\Delta$  resonance region. (a): resonance excitation, (b): vector meson exchange, (c1-c2): nucleon pole terms, (d): pion pole term, (e): Kroll-Rudermann term

(a) corresponds to  $v_{\pi}^{\Delta}$ , (b)-(e) are tree diagrams inserted in the non resonant operator  $v_{\gamma\pi}^B$ .  $g_{\rho\pi\gamma}$  and  $g_{\omega\pi\gamma}$ , referring to figure 2.4(b) are obtained from the radiative decays:  $\rho \rightarrow \gamma\pi$  and  $\omega \rightarrow \gamma\pi$ . The electromagnetic  $\gamma NN$  and  $\gamma\pi\pi$  vertices, as well as the nucleon anomalous magnetic moment  $\kappa_N$ , are extracted from experimental measurements. The resonance contribution of figure 2.4(a) is calculated by using a *Rarita-Schwinger* propagator [Ami92] and the coupling constants are extracted from measurements of  $\Delta \rightarrow \pi N$  decays.

The results of the unitary model for the total cross section of the  $\gamma p \rightarrow \pi^0 p$  and  $\gamma p \rightarrow \pi^+ n$  reactions are shown in figure 2.5 in comparison with experimental data [McP64],[Fis96],[MCo96], [Ahr00].



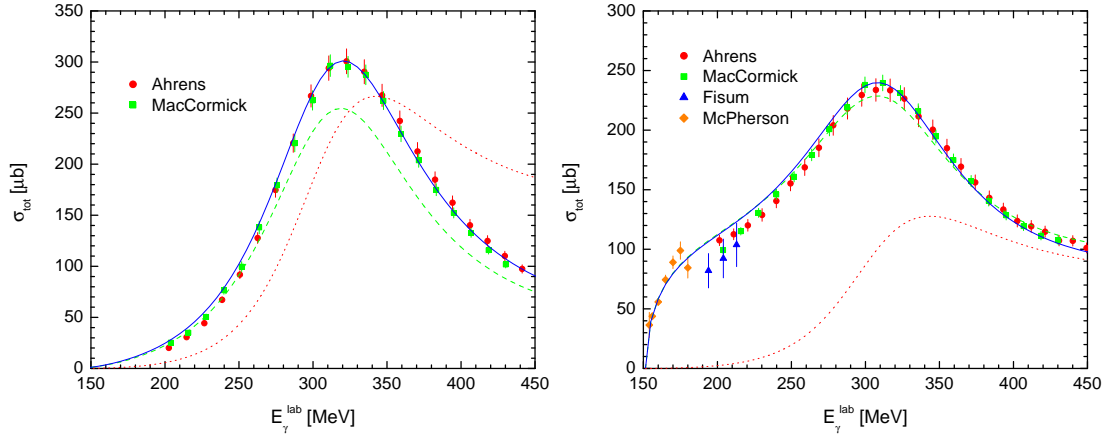


Figure 2.5: Total cross section of unitary model for  $\gamma p \rightarrow \pi^0 p$  and  $\gamma p \rightarrow \pi^+ n$  reaction. The solid curve is the full result of the unitary model, the dashed curve indicates the result of the tree-level calculation and the dotted curve shows the unitarized  $\Delta(1232)$  contribution

### The Unitary Model for the $\gamma p \rightarrow \pi^0 p \gamma'$ Reaction

This is the extension of the previously for  $\gamma p \rightarrow \pi^0 p$  described model to the  $\gamma p \rightarrow \pi^0 p \gamma'$  reaction in the  $\Delta$  resonance region. The start is the coupling of a photon to all charged particles of figure 2.4. The resulting diagrams are shown in figure 2.6.

The vector meson exchanges and pion poles, as well as the Kroll-Rudermann terms, can be evaluated with the interaction Lagrangians of the  $\gamma p \rightarrow \pi^0 p$  reaction or by minimal substitution of pion-nucleon Lagrangians. The  $\Delta$  resonance diagrams can be also similarly evaluated, except for the diagram (a2) of figure 2.6 which contains informations on  $\kappa_\Delta$ . Thus, the only new parameter entering in the description of  $\gamma p \rightarrow \pi^0 p \gamma'$ , in comparison to  $\gamma p \rightarrow \pi^0 p$  is the  $\Delta$  anomalous magnetic moment  $\kappa_\Delta$ :  $\mu_\Delta = 1 + \kappa_\Delta$ .  $\kappa_\Delta$  (via  $\gamma\Delta\Delta$  vertex) is a function of  $k_{\gamma'}^2, p_\Delta^2, p'_{\Delta}{}^2$ , i.e., the four momenta of the radiative photon and the initial and final  $\Delta$ . We then make use of the following assumptions:

- Transition induced by a real photon  $\Rightarrow k_{\gamma'}^2 = 0$ .
- Restriction in the  $\Delta$  resonance region only  $\Rightarrow p_\Delta^2 = M_\Delta^2 \Rightarrow \kappa_\Delta$  only depending on  $p'_{\Delta}{}^2$ .
- Soft photon limit  $\Rightarrow p'_{\Delta}{}^2 = M_\Delta^2$ , so treating  $\kappa_\Delta$  as constant at the soft photon limit.

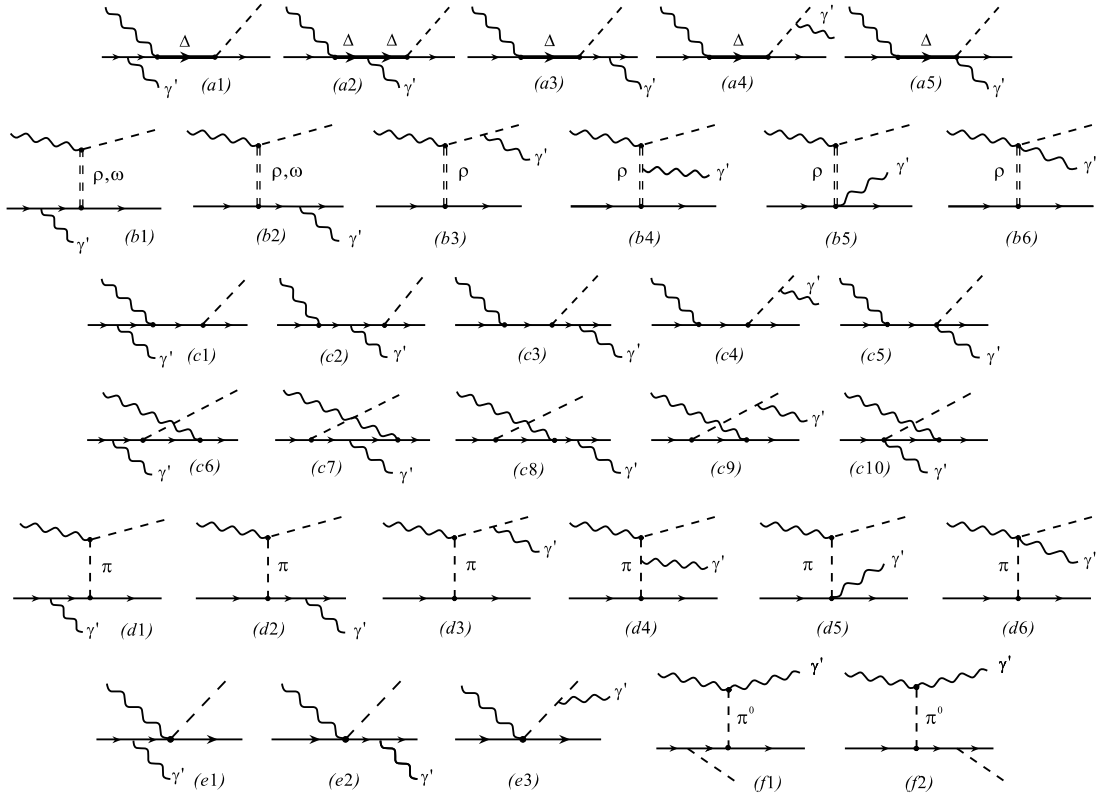


Figure 2.6: Diagrams for the  $\gamma p \rightarrow \pi^0 p \gamma'$  reaction in the  $\Delta$  resonance region. (a1-a5):  $\Delta$  resonance, (b1-b6): vector meson exchange, (c1-c10): nucleon pole terms, (d1-d6): pion pole term, (e1-e3): Kroll-Rudermann terms, (f1-f2): anomaly diagrams

The status concerning the rescattering reactions is the following:

- Consideration of the *on-shell* rescattering only.
- In the soft photon limit, T-matrix of  $\gamma p \rightarrow \pi^0 p \gamma'$  proportional to the one of  $\gamma p \rightarrow \pi^0 p$

Rescattering contributions beyond the soft photon limit are more complicated and therefore not treated here, especially the aim of the present calculations is the comparison with experimental data relatively close to the soft photon limit, i.e.  $E_{\gamma'} \approx 100$  MeV.

The resulting construction of the T-matrix for the  $\gamma p \rightarrow \pi^0 p \gamma'$  reaction is shown on figure 2.7:

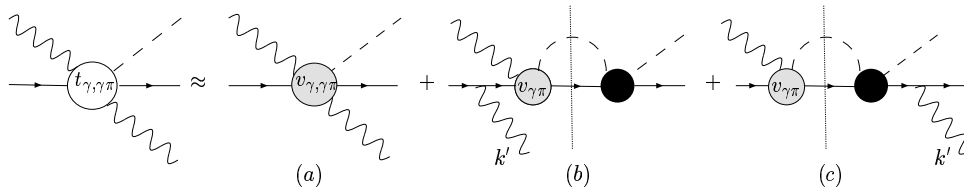


Figure 2.7: schematic view of the T-matrix used for the description of the  $\gamma p \rightarrow \pi^0 p \gamma'$  reaction in the  $\Delta$  resonance region

Diagram (a) corresponds to the diagrams of figure 2.6. The rescattering contributions (diagrams (b) and (c)) are evaluated in the soft-photon approximation for the final photon,  $k_{\gamma'} \rightarrow 0$ . The transition potential  $v_{\gamma\pi}$  corresponds to the diagrams of figure 2.6. The black blob corresponds to the full T-matrix  $t_{\pi N}$  for  $\pi N$  scattering. The vertical dotted lines indicate that the  $\pi N$  intermediate state is taken on-shell (K-matrix approximation).

The resulting predictions of the unitary model for the  $\gamma p \rightarrow \pi^0 p \gamma'$  for the  $\gamma'$  energy and angular cross sections are shown in figure 2.8:

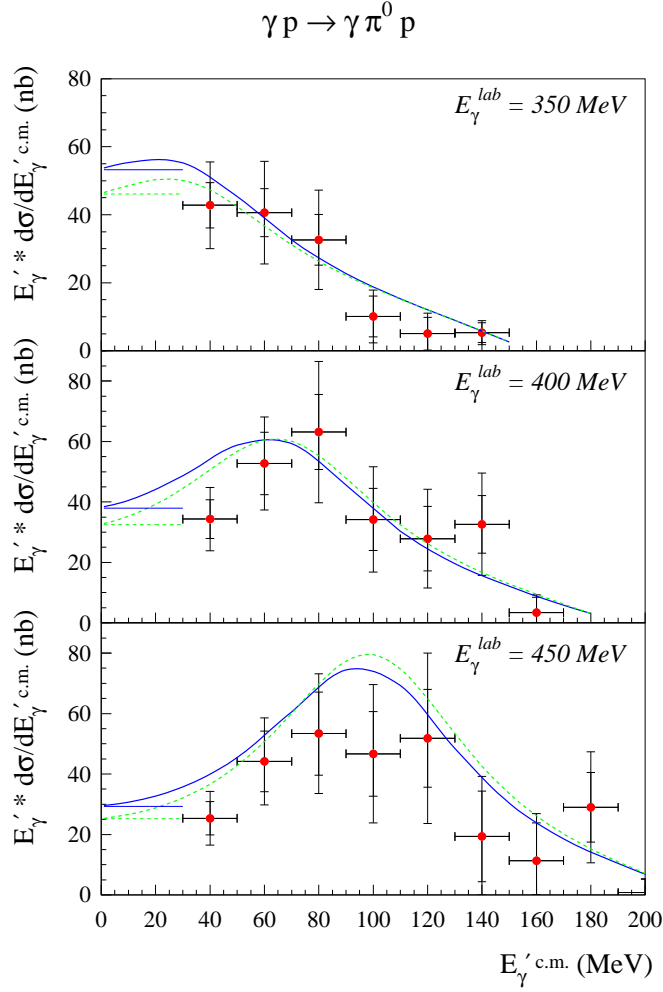


Figure 2.8: Differential cross section of  $\gamma p \rightarrow \pi^0 p \gamma'$  reaction on the energy  $E_{\gamma'}^{CM}$  of the radiative photon, divided by  $E_{\gamma'}^{CM}$ . Data from [Kot02]

### 2.2.3 Chiral Effective Field Theory Calculations

The aim of these calculations is a model independent extraction of  $\mu_{\Delta^+}$ . There are relativistic chiral effective field theory calculations of radiative pion production ( $\gamma p \rightarrow \pi^0 p \gamma'$ ) in the  $\Delta$ -resonance region, to next-to-leading order in the " $\Delta$ -expansion". The present calculations are sufficient for a chiral extrapolation of lattice QCD results for magnetic moments.

The starting Lagrangian is the one from the chiral perturbation theory ( $\chi PT$ )

with pions and nucleon fields [Ga88], where the  $\Delta$  has been included explicitly in the so called " $\delta$ -expansion scheme" [Pas03].

### The Effective Lagrangian in Chiral Effective Field Theory

The  $\chi PT$  is the effective low-energy theory of the Quantum Chromodynamics (QCD). The QCD is formulated for quark and gluon degrees of freedom and its fundamental coupling constant is the strong coupling constant  $\alpha_s$ . The asymptotic spectrum of the theory consists of mesons and baryons, which implies that a full solution to QCD must include the phenomenon of confinement of quarks and gluons and ensure that these emerge in the asymptotic states of theory. The standard QCD Lagrangian has the following form:

$$\mathcal{L} = \mathcal{L}_g + \mathcal{L}_q + \mathcal{L}_m \quad (2.13)$$

$$\mathcal{L}_g = -\frac{1}{4g^2} \text{Tr}(G_{\mu\nu}G^{\mu\nu})$$

$$\mathcal{L}_q = \sum_{f=1}^{N_f} \bar{\psi}_f i D_\mu \gamma^\mu \psi_f$$

$$\mathcal{L}_m = \sum_{f=1}^{N_f} m_f \bar{\psi}_f \psi_f$$

$$D_\mu = \partial_\mu - ig A_\mu \quad (2.14)$$

$$G_{\mu\nu} = [D_\mu, D_\nu] \quad (2.15)$$

$A_\mu$  is the gluon field,  $\psi_f$  is the quark field of the  $f$ -th flavour ( $\psi_f = (u, d, c, s, t, b)$ ),  $D_\mu$  is the covariant derivative,  $G_{\mu\nu}$  is the field strength tensor and  $g$  is the colour charge.  $\mathcal{L}_g$  describes pure gluon dynamics,  $\mathcal{L}_q$  corresponds to the quarks kinetic energies and quark-gluon interaction,  $\mathcal{L}_m$  is responsible for the quark mass. In the massless limit, the QCD Lagrangian ( $\mathcal{L}_g + \mathcal{L}_q$ ) depends only on one dimensionless parameter  $g$ . Moreover, the coupling constant  $\alpha_s(\mu)$  becomes scale dependent due to renormalization. The scale parameter of QCD is experimentally determined.

Provided the quarks are massless, the chirality (helicity) of a quark is conserved and the QCD Lagrangian is symmetric with respect to rotations in the flavor space independently for right- and left-handed quarks. Thus the massless QCD has the global symmetry described by the group  $SU(N_F)_R \times SU(N_F)_L$ . While the Lagrangian is chirally symmetric, the ground state of the massless QCD (vacuum) does not have the same property because the chiral symmetry is spontaneously broken: The characteristic feature of this spontaneous symmetry breaking is the emergence of massless pseudoscalar particles: the *Goldstone bosons*. In the case of three flavours,  $N_F = 3$ , they correspond to the members of the pseudo-scalar meson octet (see fig 2.9).

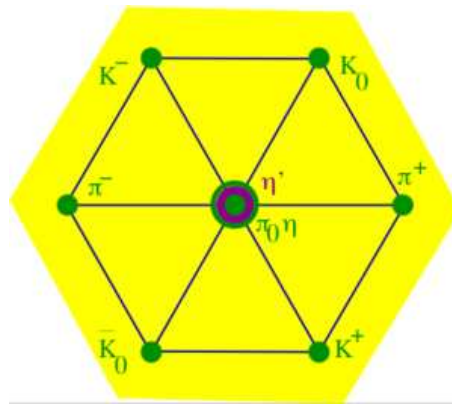


Figure 2.9: The octet of the pseudo-scalar mesons obtained with SU(3) symmetry

The essence of the chiral perturbation theory is to consider the quark mass term  $\mathcal{L}_m$  as a perturbation. The mass term explicitly breaks the chiral symmetry, so that the Goldstone bosons get nonzero masses and in the leading order the pion mass squared is proportional to the quark mass:  $\chi PT$  is an effective field theory constructed as an expansion in momenta and masses of physical particles, which are considered to be small on a hadronic scale of about one GeV. This approach is extended in the baryon chiral perturbation theory, so that the meson interaction with "heavy" baryons can be treated as well.

The  $\chi PT$  is limited to a low-energy domain where the momentum of the particles  $p$  are much lower than the masses  $\Lambda$  of "new degrees of freedom" not taking part in the Lagrangian:  $p \ll \Lambda$ . In the pion-nucleon case, this limit is set by the excitation energy of the  $\Delta$  resonance:  $\Delta = M_\Delta - M_N \approx 293$  MeV. It has been already observed that  $\chi PT$  is in very good agreement with experiment up to a photon energy of about 100 MeV, but fails above 150 MeV. A new

power-counting scheme for  $\chi PT$  that includes  $\Delta$  degrees of freedom has been performed by V. Pascalutsa [Pas03], it is the so called  $\delta$ -expansion scheme.

### The $\delta$ -expansion Scheme

The scheme is both closely connected to the usual  $\chi PT$  (i.e. without  $\Delta$ , assuming  $m_\pi \ll \Delta$ ) in the low energy region where the photon energy  $\omega$  is in the region of the pion mass and applies in the  $\Delta$  resonance region:  $\omega \sim \Delta$ . This is reached with the following hierarchy of scale:

$$m_\pi \ll \Delta \ll \Lambda \quad (2.16)$$

Using this 3-scale hierarchy equation 2.16, we have in principle two small expansion parameters:  $m_\pi/\Delta$  and  $\Delta/\Lambda$ . Assuming the breaking-down scale is now set by the next excitation energy,  $\Lambda \approx 1535 - 938 \approx 600$  MeV, our two ratios are not far from each other and we can introduce the small parameter:

$$\delta = \frac{\Delta}{\Lambda} \sim \frac{m_\pi}{\Delta} \quad (2.17)$$

Each graph taking part in the Lagrangian may thereafter be characterized by a  $\delta$ -counting index " $\alpha$ ", which delivers the size  $\delta_\alpha$  of the graph. The index  $\alpha$  has two different expressions, depending on the  $\omega$  region ( $m_\pi$  or  $\Delta$ ). For a graph with  $L$  loops,  $N_\pi$  pion propagators,  $N_N$  nucleon propagators,  $N_\Delta$  delta propagators and  $V_i$  vertices of dimension  $i$ , we have:

$$\begin{aligned} \text{For } \omega \sim m_\pi, \quad \alpha &= 2\alpha_{\chi PT} - N_\Delta \\ \text{For } \omega \sim \Delta, \quad \alpha &= \alpha_{\chi PT} - N_\Delta \end{aligned} \quad (2.18)$$

Where  $\alpha_{\chi PT} = \sum_1 iV_i - 2 + 4L - N_N - 2N_\pi$  is the index of  $\chi PT$  with no  $\Delta$  s.

The graphs considered for the determination of the  $\mu_{\Delta^+}$  are shown in figure 2.10:

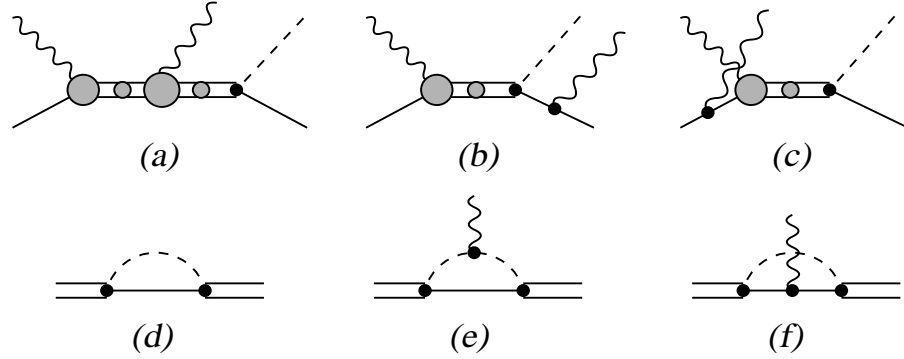


Figure 2.10: Diagrams for  $\gamma p \rightarrow \pi^0 p \gamma'$  reaction in the NLO  $\delta$ -expansion. Double lines represent the  $\Delta$  propagator

The results of these effective field theory calculations are shown in figure 2.11 in terms of cross sections and asymmetries. The Ratio  $R$  is defined as follows:

$$R = \frac{1}{\sigma_\pi} \cdot E'_\gamma \frac{d\sigma}{dE'_\gamma} \quad (2.19)$$



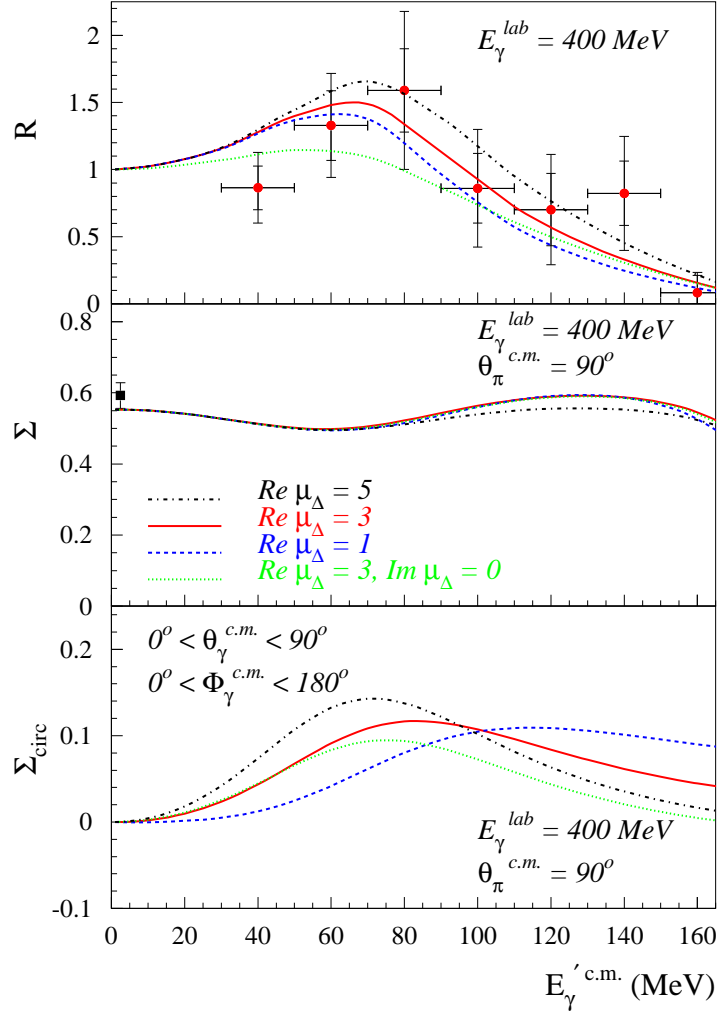


Figure 2.11: Results of the effective field theory calculations. TOP: Ratio (equ 2.19) of the  $\gamma p \rightarrow \pi^0 p$  and  $\gamma p \rightarrow \pi^0 p \gamma'$  cross sections on  $E_{\gamma'}^{C.M.}$ . Data from [Kot02]. MIDDLE: Linear photon asymmetry of the  $\gamma p \rightarrow \pi^0 p$  cross-sections differential w.r.t. the outgoing photon energy and pion c.m. angle. The data point at  $E_{\gamma'} = 0$  corresponds with the  $\gamma p \rightarrow \pi^0 p$  photon asymmetry from [Bec99]. LOW: the circular-polarization photon asymmetry (as defined in [Chi05]), where the outgoing photon angles have been integrated over the indicated range.



# Chapter 3

## Experiment Setup

### 3.1 Overview

The experiment has been performed in the A2 experimental hall at the "MAInzer Microtron (MAMI), Mainz, Germany.

An important improvement compared to the last  $\mu_{\Delta^+}$  measurement is the almost  $4\pi$  steradians covering detector setup. This is reached by the combination of the Crystal Ball detector with the TAPS detector as forward wall detector.

The photon beam is delivered via bremsstrahlung and tagging of the polarized electron beam of MAMI C with the Glasgow tagger. The use of crystal radiator offers the opportunity of an as well circularly as linearly polarized photon beam.

The proton target is obtained with the use of liquid hydrogen.

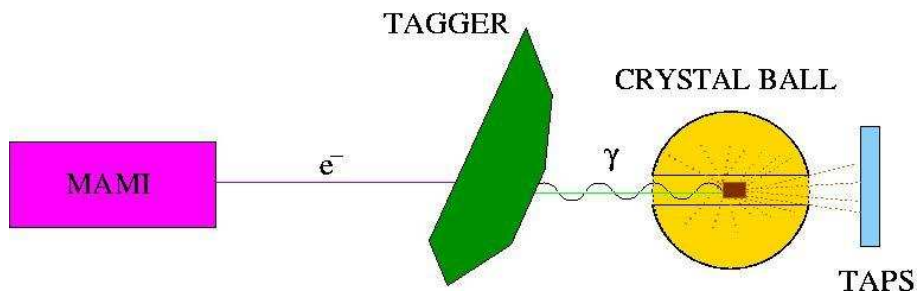


Figure 3.1: Overview of Experimental Setup

## 3.2 The polarized Photon Beam

The real photon beam is produced by the collision of the electron beam provided from MAMI with a radiator foil and emission at this stage of bremsstrahlung photons.

The radiator is needed for the absorption of momentum, as free charged particles cannot radiate real photons because of the energy-momentum conservation. The comparison of the nucleus mass to the very light electron permits to neglect the energy transfer to the nucleus and thus the following equation may be used:

$$E_\gamma = E_{e_{in}^-} - E_{e_{out}^-} \quad (3.1)$$

The emitted photons fly in the forward direction to the target, as the recoil electrons  $e_{out}^-$  are deviated in the huge tagger magnet, according to their remaining kinetic energy and are stopped in the tagger focal plane detectors.

The precise determination of the recoil electron hit location in the tagger focal plane detectors allows a near to perfect determination of its energy  $E_{e_{out}^-}$  using the deflection law and therethrough the corresponding emitted photon energy.

### 3.2.1 The MAMI polarized Electron Beam

The accelerator MAMI is a racetrack microtron accelerator, which uses the high frequency acceleration system. In order to optimize the acceleration without using a very long accelerator, the electrons pass many times through the linear high frequency path. They gain energy at each passage and thus make each time a trajectory with a larger radius through the magnets. They so use every time a new linear path, as shown on figure 3.2. The beam is very clean, without any halo. This layout is called *racetrack microtron*.

The electron accelerator MAMI at the experiment time consisted of three cascaded racetrack microtrons with a 3.5 MeV injector linac. The last stage delivered the beam from 180 MeV to 855 MeV in 15 MeV steps.

The polarization of the electron beam is produced by photoelectric emission from InGaP- or GaAsP-crystal cathodes [Aul99,Aul00].

The helicity of the electron beam can be inverted by changing the circular polarization of the irradiating light. The Wien filter just behind the source allows the adjustment of the spin orientation at a determined place, which, in

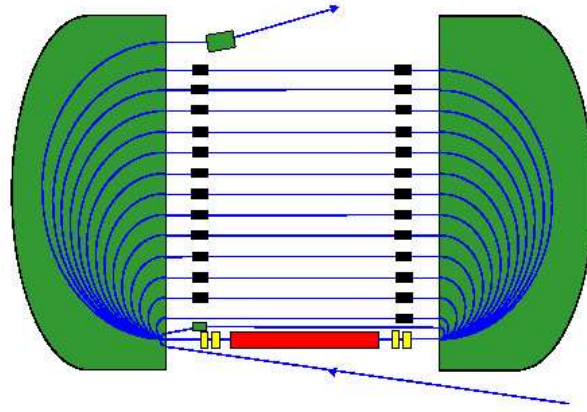


Figure 3.2: Racetrack Microtron

our case, is situated just near by the tagger radiator. The error limits delivered by the accelerator team on the spin direction is the following:

$$\text{max: } E_e = 883.28 \text{ MeV}, 13.91^\circ, \text{ min: } E_e = 883.06 \text{ MeV}, 5.81^\circ$$

### 3.2.2 The linearly and circularly polarized Photon Beam

#### The Bremsstrahlung Generalities

The bremsstrahlung is the process whereby a charged particle is slowed down by an electric field with the emission of a real photon. This is in our case the scattering of electrons on a radiator foil, the latter being needed for the energy/momentum balance. Due to the huge mass of the foil nuclei in comparison to the electron mass, the energy transfer to the nuclei can be neglected.

We can thus use the following relations:

$$\begin{aligned} \vec{p}_\gamma &= \vec{p}_0 - \vec{q} - \vec{p}'_e \\ E_\gamma &= E_0 - E'_e \\ \vec{q} &: \text{momentum transfer to the nucleus} \end{aligned} \quad (3.2)$$

The energy and angle distributions of the emitted photons follow approximately the following relations:

$$\begin{aligned}\frac{d\sigma}{dE_\gamma} &\propto \frac{1}{E_\gamma} \\ \frac{d\sigma}{d\theta} &\propto \frac{\theta}{(\theta^2 + \theta_c^2)}\end{aligned}\quad (3.3)$$

Where  $\theta_c$  is the characteristic opening angle of bremsstrahlung. Thereafter, the proportion  $P$  of photons inside a cone with opening angle  $\beta$  is approximately:

$$P(\beta) \approx \frac{1}{1 + (\theta_c/\beta)^2} \quad (3.4)$$

Considering this relation, 50 % of the photons are found in the cone with opening angle  $\beta = \theta_c$

### Linearly polarized Photons

Linearly polarized photons are obtained by coherent bremsstrahlung on a crystalline radiator, in our case a 100  $\mu\text{m}$  thick diamond foil.

The bremsstrahlung process is azimuthal symmetric around the direction of  $\vec{p}_0$ . Thus, the momentum transfer  $\vec{q}$  can be split in a longitudinal  $q_l$  and transversal  $q_t$  component with respect to  $\vec{p}_0$ . Using this property we can determine the allowed region in the momentum space:

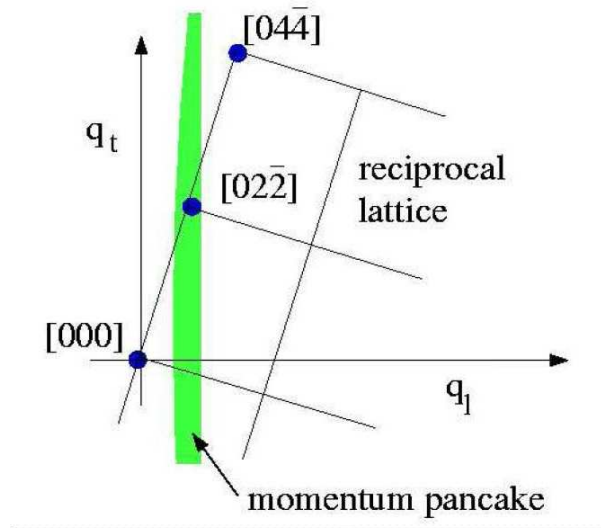


Figure 3.3: Representation of the allowed momentum pancake in the momentum space and the reciprocal lattice

The condition for a coherent bremsstrahlung is that the momentum transfer corresponds to a reciprocal lattice vector  $\vec{g}$  of the crystal (Bragg condition):

$$\begin{aligned} \vec{q} &= \vec{g} \\ \text{with } \vec{g} &= \sum_{i=1}^3 h_i \vec{b}_i \\ \vec{b}_i &: \text{reciprocal lattice basis vector} \\ h_i &: \text{set of Miller indices} \end{aligned} \quad (3.5)$$

The ideal crystal for coherent bremsstrahlung should have a tight lattice, a low  $Z$  and a high Debye temperature. Due to this fact, diamond is the best choice by far.

Only an *ideal* crystal would deliver a pure coherent spectrum. Real crystal lattices are affected by the thermal movements of the atoms and consequently always deliver a part of *incoherent* bremsstrahlung. The incoherent scattering produces photons with a continuous angular distribution, independent of  $k$  and characterized by  $\frac{m_e}{E}$  (see fig.3.4, Nickel). The coherent radiation is tightly collimated along the electron direction at the peak position (see fig. 3.4, Diamond).

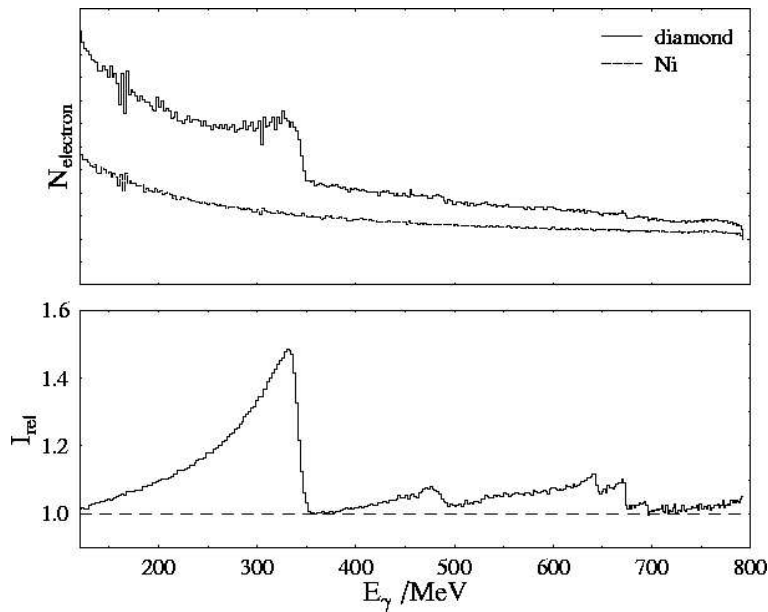


Figure 3.4: UP: Electron spectra seen in the tagger, with coherent (diamond) and incoherent (nickel) bremsstrahlung. DOWN: same spectrum normalised to the incoherent part:  $I_{rel} = I_{diamond}/I_{incoherent}$ .

The photons situated in the peaks are mostly linearly polarized, and the peak positions depend on the orientation of the crystal related to the electron beam. This is monitored with the so called *Goniometer*, in which the different radiators are placed and chosen.

### Circularly polarized Photons

The circular polarization of the photons is reached by the use of longitudinal polarized electrons in the bremsstrahlung process. A transfer of helicity occurs from the electrons to the emitted photons. Thus, as the helicity of the photon beam depends directly on the spin direction of the electrons, the information concerning the electron polarization delivered by MAMI allows the determination of the helicity status of the corresponding photon.

Thanks to the Wien filter (speed-filter) situated directly after the electron source and a precise determination of the final electron energy at RTM3 <sup>1</sup>, the spin direction of the electron by the radiator foil can be precisely monitored.

Each variation in the electron energy induces a spin deviation. Typically,  $\frac{E}{\Delta E} = \pm 1.4 \cdot 10^{-3}$  rotates the spin by  $\pm 60^\circ$  [Tio02]. The spin deviation delivered by the accelerator team for the minimum and maximum electron energy during the MDM beamtimes are the following:

$$\begin{array}{ll} 883.28 & \text{MeV} : 13.91^\circ \\ 883.06 & \text{MeV} : 5.8^\circ \end{array} \quad (3.6)$$

The final degree of polarization of the photon beam can be calculated as the following [Ols59]:

$$P_\gamma = P_e \frac{4x - x^2}{4 - 4x + 3x^2}$$

where  $x = \frac{E_\gamma}{E_0}$  and  $P_e$  gives the degree of polarization of the electron beam. The value delivered by the MAMI team for our case is  $82 \pm 5 \%$ .

---

<sup>1</sup>Third and last microtron of the electron beam



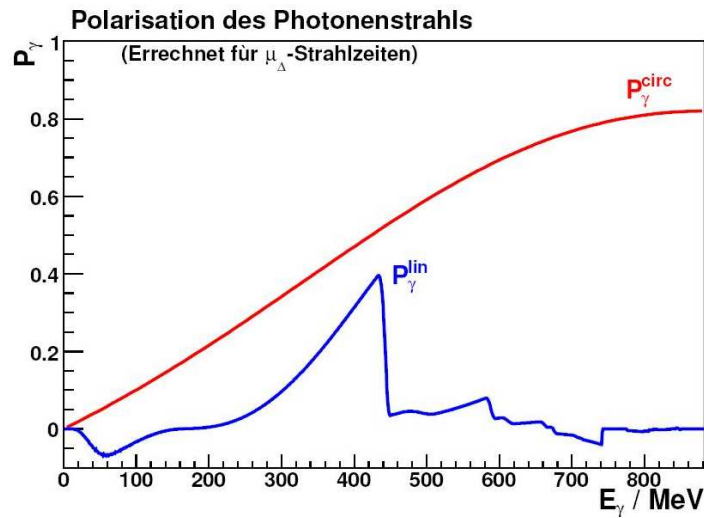


Figure 3.5: Linear and circular degree of polarization of the photon beam, depending on its energy.

The determination of the degree of polarization of the photons is crucial and can be obtained with calculations. Anyhow, those calculations have to be checked with measurements. For this purpose, the photoproduction of  $\pi^0$  mesons from  ${}^4\text{He}$  has been used. As a nucleus of spin=0,  ${}^4\text{He}$  has an analysing power of 100% for linearly polarized photons. The degree of linear polarization reached during our measurement is  $\approx 37\%$ .

### 3.2.3 The Glasgow Tagger Magnet

The precise determination of the photon beam energy, as well as the recoil electrons flux, is done by the tagger system.

The Glasgow Tagger Magnet consists of a large dipole magnet and a focal plane detector system. The dipole primarily "cleans" the photon beam from the outgoing electrons, but first of all traps those electrons in its 353 focal plane scintillators.

As shown in picture 3.4, the recoil electrons are bent to different paths, which guide to different scintillators, this depending on their remaining kinetic energy. The electrons that did not produce bremsstrahlung are directly bent to the Faraday cup of the beam dump.

Since working with the coincidence principle, the information of the initial elec-

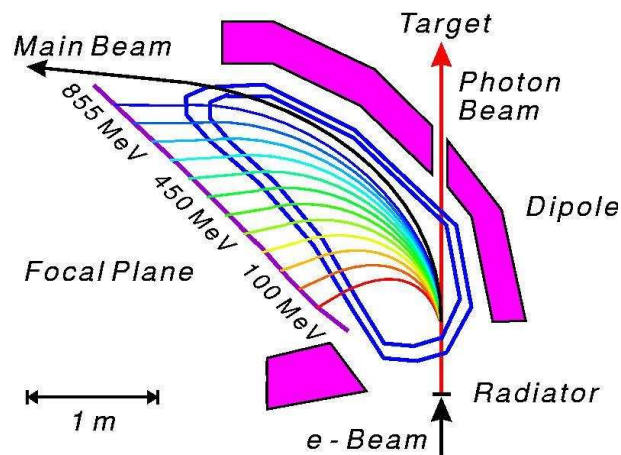


Figure 3.6: The Glasgow Tagging System

tron beam energy and the corresponding outgoing electron energy associated to a tagged photon, deliver the energy of the latter photon via the relation 3.1

In order to obtain a first reduction of the background, the scintillators are built in brick configuration. Each detector overlaps its two neighbours, so that each true bremsstrahlung electron fires two scintillators. Events induced by only one hit are ignored, which results in 352 coincidence channels for the tagger.

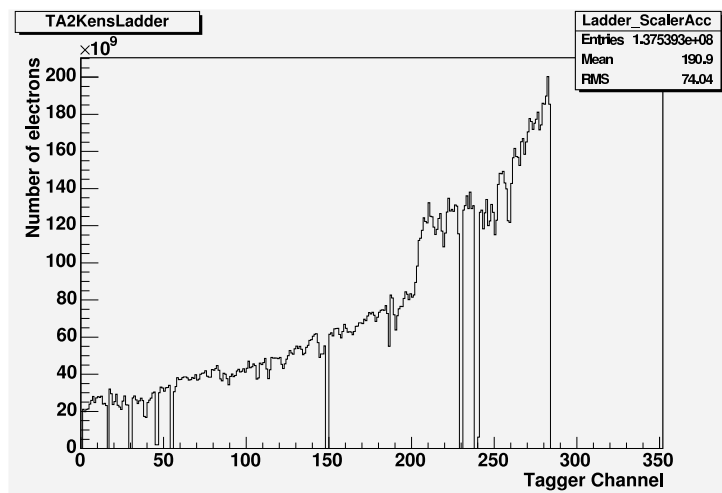


Figure 3.7: Distribution of the electrons on the focal plane detector

We identify here the polarization enhancement, due to coherent bremsstrahlung. The tagger spectrum covers from 7 % to 95 % of the photon energies with approximately 2 MeV resolution. Channel 0 corresponds to  $E_\gamma = 819$  MeV, channel 284 to  $E_\gamma = 205$  MeV. Due to saturation risk, the channels corresponding to low energetic photons/high energetic electrons, were switched off. As a matter of fact, the  $1/E$  bremsstrahlung distribution shape produces an enormous quantity of low energetic photons.

For  $E_\gamma = 674 - 728$  MeV, a special detector system, the so called *Tagger Microscope* [Rei99] was placed in order to increase the energy resolution. However, this device is not used in this work, since the analyzed data are situated in a photon energy range below 600 MeV.

### Tagging Efficiency Measurements

The knowledge of the photon flux is needed for the absolute normalization of cross sections.

This flux is, however, not equal to the number of the recorded recoil electrons in the tagger. Due to collimation, Møller scattering and other processes, the number of photons reaching the target is lower than the number of electrons recorded in the tagger.

Thus, the number of emitted photons for a specific beamtime period is obtained by the combination of the emitted electrons during this time (scalers) and the efficiency of the tagging system:

$$N_\gamma = N_{e^-} \cdot \epsilon_{tagg}$$

Tagging efficiency measurements have been performed once a day of beamtime, using the following setup:

The recoil electrons are detected in the tagger focal plane detectors. The tagged photons that pass through the collimator are detected in a lead glass detector.

The ratio of the tagging photon spectrum and the electron spectrum delivers a tagging efficiency for each tagger channel:

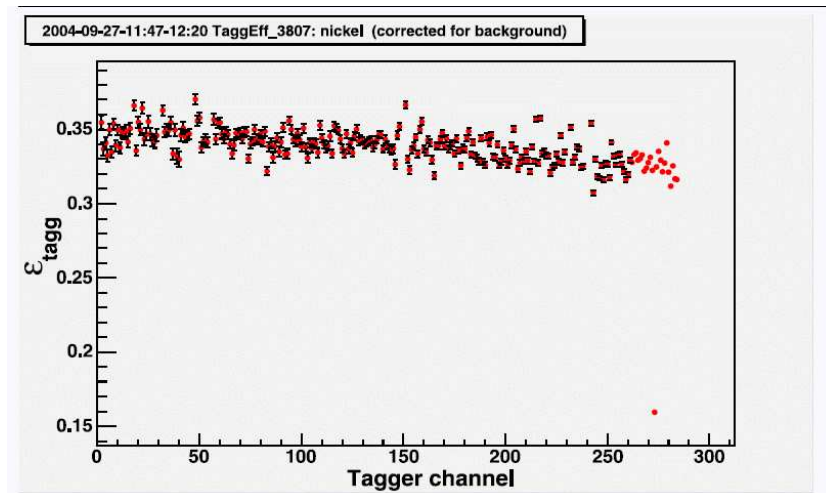


Figure 3.8: Example of tagging efficiency measurement

### 3.3 The Hydrogen Target

Our liquid hydrogen target cell was built by using the DAPHNE cryotarget system [Tho04a]. It consists of a  $125 \mu\text{m}$  thick Kapton cylinder with a length of 48 mm and a diameter of 24 mm.

This cylinder is coated with eight layers of a "super isolator" ( $8 \mu\text{m}$  Mylar, two  $\mu\text{m}$  Aluminium).



Figure 3.9: The Liquid Hydrogen Target

Due to an ice accumulation on the cell window, an additional  $10 \mu\text{m}$  thick Kapton cylinder has been mounted around the isolation layer.

The cell is placed in a one mm thick and 82 mm large fibre vacuum tube.

The latter offers a Kapton window to protect the target cell and play the role of a scattering chamber, avoiding the hydrogen to reach the air in case of a cell leakage.

The target pressure is kept by 1080 mbar, just above the atmospheric pressure to minimise the risk of air penetrating into the target.

## 3.4 The Crystal Ball Apparatus

### 3.4.1 Overview

The crystal ball apparatus is composed of the spherical crystal ball NaI detector and two additional components placed in the center of the ball (see fig 3.10). These are a Particle Identification Detector and a Multi Wire Proportional Chamber. This combination ensures adapted energy and time resolution thanks to the NaI detector system, a trustable particle identification, as well as a precise determination of the particles's position.

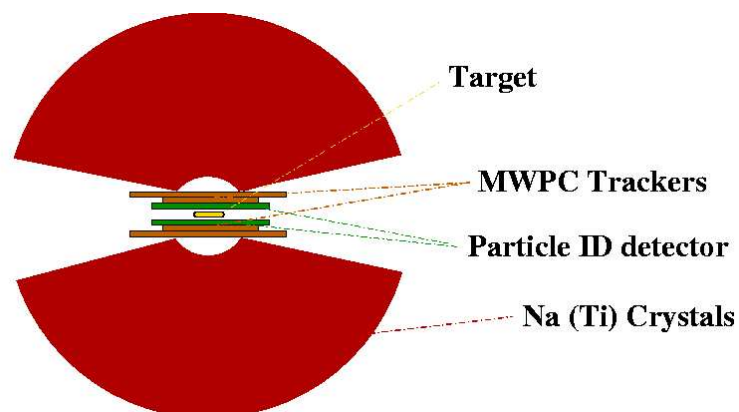


Figure 3.10: The Crystal Ball Apparatus

### 3.4.2 The Crystal Ball Detector

The crystal ball detector was built at SLAC and used in  $J/\Psi$  measurements at SPEAR and c quark physics at DESY.

It is a segmented Sodium Iodide detector of 672 crystals and covering 94 % of  $4\pi$  steradians.

This detector is especially adequate for time, energy and polar angle determination of multi-photon events.

The ball geometry is an icosahedron divided in 20 "Major Triangles" that are themselves split in four "Minor Triangles" containing each nine crystals. 24 crystals are missing in this structure to offer space for the tunnel path, which has an opening angle of  $\approx 20$  degrees. The crystal ball has an inner radius of 25.3 cm and outer radius of 66 cm.

The detector is surrounded by two Aluminium frames essential for the stability of the photomultipliers and the inside apparatus.



Figure 3.11: LEFT: Complete crystal ball before cabling. RIGHT: Part of the crystal ball detector. View of bare crystals and ones equipped with photomultipliers

To reach the target and other devices in the center of the ball, the latter is composed of two separable spherical shells (see figure 3.11 left). The so called *equator* between the hemispheres is 0.8 cm thick and consists of 1.6 mm stainless steel plates, separated by five mm air. This gap induces the small loss of 1.6 % of  $4\pi$  steradians. The two shells are kept under low pressure, to avoid humidity reaching the crystals, as these are very hygroscopic.

The NaI crystals have a pyramide shape and point to the center of the ball. They have a length of 40.6 cm and a thickness of 15.7 radiation length. All

the 672 crystals are coated with a 0.15 mm thin reflecting paper, so to be optically isolated.

The SRC L50 B01 photomultipliers have a diameter of 5.1 cm and have been selected for their linearity over a wide dynamic range.

### 3.4.3 The Particle Identification Detector

The Particle Identification Detector or (PID) was built in 2002-2004 by a team of the Glasgow University and it has been part of the PhD work of the colleague Evangeline Downie [Dow06].

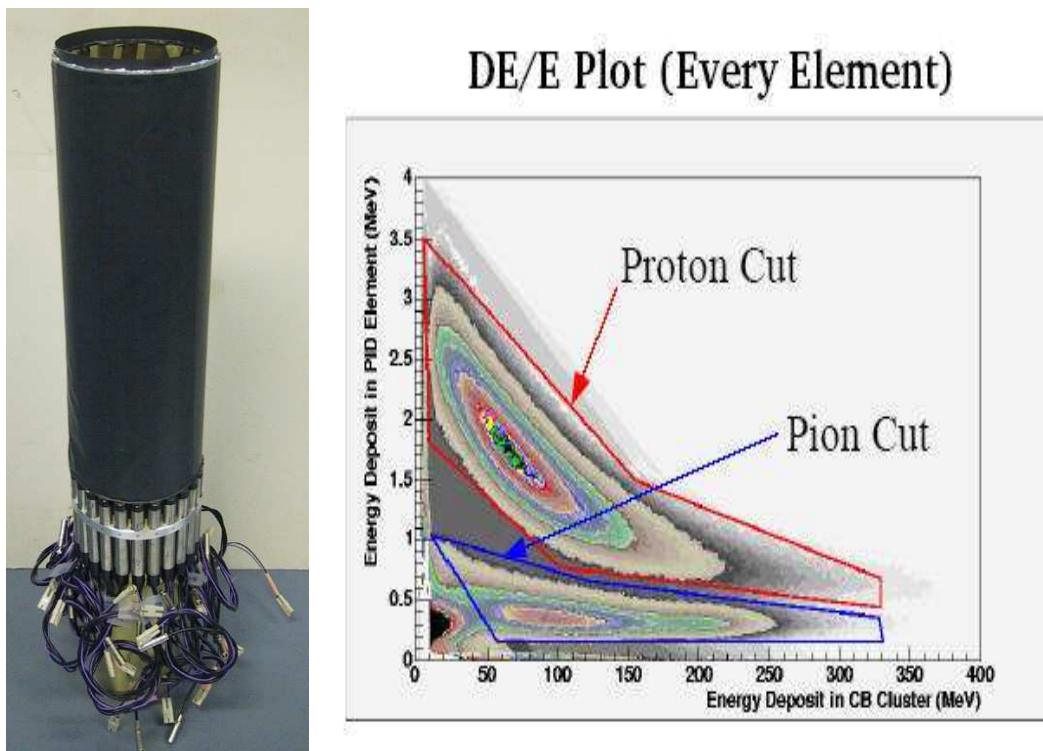


Figure 3.12: LEFT: View of the PID. RIGHT:  $E/\Delta E$  plot of the PID

We need the PID detector because the very short distance between the target and the ball and the too poor time resolution do not allow any time of flight measurement.

The main goal of the PID is the identification of the protons, pions and electrons, using their specific  $E/\Delta E$  ratio defined below.

The unusual location of the PID **in front of** the wire chamber on the way from the target to the detector is due to a space lack between the wire chamber and the NaI detectors.

Tests that have been realized with Geant3 models for the detector delivered a two mm thick plastic scintillator being a good compromise between a multiple scattering and a functional energy loss signal. The PID is, according to this, a 10 cm diameter barrel composed of 24 pieces of 31 cm x 13 mm x 2 mm plastic scintillators.

The identification between the different particles is reached by a comparison between the energy  $E$  deposited in the NaI, which is supposed to be the total energy, and the small energy ( $\approx 400$  keV for minimum ionising particle)  $\Delta E$  deposited in the PID scintillators. The latter energy is different for particles having the same total energy, but a different ionisation density.

Looking at the  $E/\Delta E$  ratio (fig 3.12, RIGHT), we clearly identify definite regions corresponding to the different particles. These regions are defined as polygons, so that e.g., to be accepted as a proton, a particle has to have a  $E/\Delta E$  ratio in the red area of figure 3.12.

### 3.4.4 The Wire Chamber

The **Multi Wire Proportional Chamber** is based on the principle of a condenser. Our MWPC is basically the one used with the DAPHNE detector [Aud91] and is especially well adapted for the tracking of protons and charged pions that often fire one or two NaI crystals only. An additional tracking of the photon position is not needed, as the coordinates resolution provided by the NaI of the crystal ball is high enough.

In our MWPC, the anode and cathode are coaxial cylinders and the use of the inner and outer side of them provides two tracking chambers (see fig 3.13, LEFT). The third chamber of the DAPHNE MWPC could not be used due space constraint. The two tubes are made of one mm thick Rohacell, coated with a 25  $\mu\text{m}$  Kapton film.

The anodes wires are parallel to the tube axis and of 20  $\mu\text{m}$  thick Tungsten.



They are placed every two cm around the circumference. The cathode strips are placed at  $45^\circ$  to the anode wires and made of  $0.1 \mu\text{m}$  thick and four mm wide Aluminium. The gap between the anode and the two cathodes is four mm. The chambers are filled with a mixture of 74 % Argon, 25 % ethane and 0.5 % freon.

Ionising particles deposit electron-ion pairs along their path in the chambers (first ionisation). The electrons are then quickly caught by the anode wires and induce there new charge pairs, while the ions slowly travel to the cathode strips. The chambers operate in a *proportional range* ( $U_1 \approx 2445 \text{ V}$ ,  $U_2 \approx 2475 \text{ V}$ ), i.e, the charges produced by the first and second ionisation are proportional to each other. The charges induced on the cathodes strips are read via an Alcatel 1757 amplifier, the ones induced on the anode wires are digitalised via a LeCroy PCOS 2735C amplifier-discriminator.

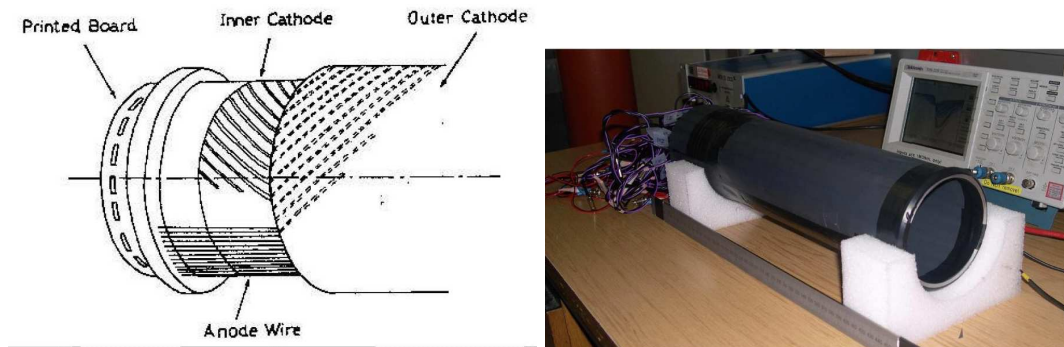


Figure 3.13: LEFT: Schematic view of the MWPC. RIGHT: Tests on the MWPC

The hit position can be located by determining the center of gravity of the charges induced in the several strips. The coordinates delivered by the MWPC are given by an azimuthal angle  $\alpha$  and a longitudinal coordinate  $z$  (cylinder axis direction). In order to determine the  $z$  coordinate when a wire has fired, the inner and the outer cathode strips cross each other twice along the length of the chamber. The location of the same position in two chambers indicates a particle track.

The area covered by the MWPC is  $360^\circ$  in  $\phi$  and from  $21^\circ$  to  $91^\circ$  in  $\theta$ . This gives a total of 94 % of  $4\pi$  steradians.

The electrical screening is obtained by a  $0.1 \mu\text{m}$  thick Aluminium coating on the external surface of the chamber.

## 3.5 The TAPS Apparatus

The TAPS apparatus, used as forward wall in addition to the crystal ball apparatus (see fig 3.14), is composed of two parts: The *TAPS* detector itself, i.e the wall of crystals and a layer of five mm thick plastic scintillators, the *TAPS Vetos*. The goal of this detector combination is the detection of photons, pions and protons along the Lorentz boost induced by the photon beam.

TAPS is placed 175 cm away from the target center, covering a  $\theta$  angle from  $4^\circ$  to  $20^\circ$ , largely the area of the crystal ball tunnel.

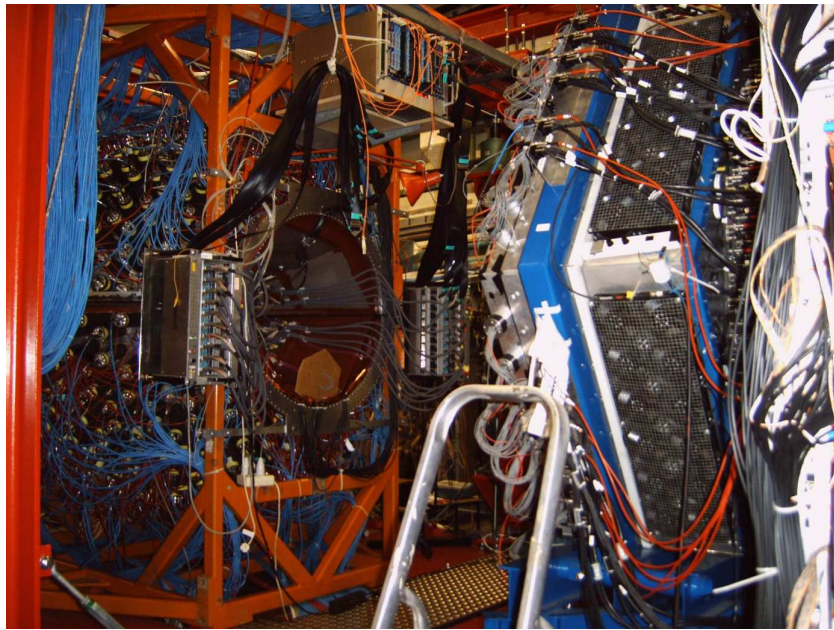


Figure 3.14: View of the crystal and the forward detector TAPS on the right

### 3.5.1 The TAPS Detector

The originally called **Two Arms Photon Spectrometer** was built by a European collaboration, to investigate high energy photons as well as neutral mesons ( $\pi^0$ ,  $\eta$ ,  $\omega$ ) in relativistic and ultra-relativistic heavy ion or photonuclear reactions.

In order to reconstruct the invariant mass of a meson from its decay products (here mostly photons), the hit position and the total energy of the electro-

magnetic shower<sup>2</sup> have to be precisely determined. Due to a high multiplicity of hadronic reaction products, a very efficient discrimination between charged and neutral particles is needed.

The above described required properties are fulfilled by the use BaF<sub>2</sub> crystals as scintillation material. The TAPS detector is made of 510 BaF<sub>2</sub> modules built in an hexagonal wall and segmented in eight blocs (4 segments for the trigger) (see fig 3.15).

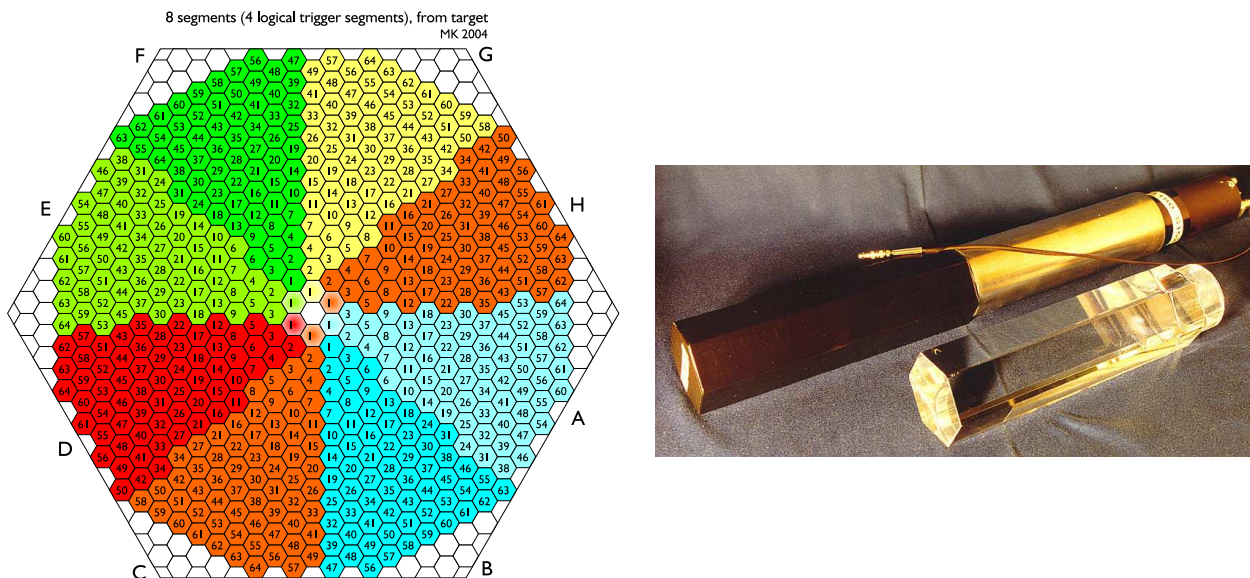


Figure 3.15: LEFT: Hexagonal wall of BaF<sub>2</sub>. RIGHT: TAPS detector module

Each detector module is composed of a 250 mm long hexagonal ( $\varnothing=59\text{mm}$ ) BaF<sub>2</sub> crystals, whose last 25 mm are spherically shaped, in order to have a better match to the photomultiplier tube (see fig 3.15, RIGHT). Each crystal owns a quartz fiber to send laser light inside, to allow the gain monitoring and the calibration for the readout electronics.

The crystals are wrapped with PTFE and an additional aluminium foil as UV reflector. They are optically coupled to the quartz window of an Hamamatsu R2059-01 photomultiplier. The assembly of the module is achieved by using a 0.2 mm thick heat shrinkable and light tight PVC tubing.

<sup>2</sup>A description of the response measurement performed by the autor on the TAPS crystals follows in chapter 4.4.3

The energy and time resolution of TAPS are the following:

$$\sigma E/E = 0.59\%/\sqrt{E/GeV} \text{ and } \Delta t < 200 \text{ ps}$$

An additional and particularly useful property of the BaF<sub>2</sub> scintillator is its sensitivity to the nature of the detected particle. It is based on the relative contribution between fast (short gate<sup>3</sup>) and slow (long gate<sup>4</sup>) light components that depends on the ionization properties of the particles. By building the ratio of the fast (short gate) and the total (long gate) light inputs, one distinguishes clearly different rising slopes corresponding to the different particles (see fig 3.16).

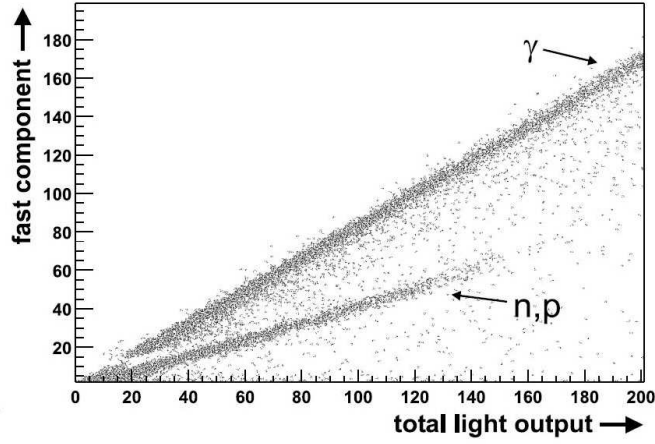


Figure 3.16: Ratio of short (fast light) and long gate (total light)

### 3.5.2 The TAPS Vetos

In order to improve the particle identification in TAPS, a thin Veto wall of 5mm plastic scintillators is installed in front of the BaF<sub>2</sub>. The signals are read out by an optical fiber and do not deliver any energy or time information, but a simple "YES/NO", i.e. "fired/not fired" signal. However, this allows the separation of the protons that fire the vetos and the neutrons that do not, as in this case the PSA tracking is not reliable enough.

---

<sup>3</sup> $\lambda_{short}^{max} = 220mm \rightarrow \tau_{short} = 0.6ns$

<sup>4</sup> $\lambda_{long}^{max} = 310mm \rightarrow \tau_{long} = 620ns$

## 3.6 The Trigger and Electronics System

### 3.6.1 The Crystal Ball and Trigger Electronics

In view of our A2-CB-TAPS experiment, the CB electronics has been newly designed [Kram07].

Considering the main measurement of this experiment, which is the determination of the magnetic moment of the  $\Delta^+$  resonance via the reaction channel  $\gamma p \rightarrow \gamma' p \pi^0$ , it appears as essential to be able to distinguish reactions that only differ by one photon. Thus the CB electronics has to reach two goals: a fast event treatment and an efficient trigger selection. The previous CB electronics was only able to treat several Hertz and was over 30 years old.

The main properties of the new CB electronics are the following:

- Treatment of 1000 events per second including energy and time information for all crystals concerned by the present event.
- CB responsible for the experiment main trigger. It collects the number of clusters (area of fired crystals corresponding to an event) and deduces the final trigger decision.
- The ADCs have been designed by the München University. They have the property of a continuous sampling with a rate of 40 MHz and are, due to this fact, called *SADC* (Sampling-ADC).
- The CATCH TDCs and Scalers are the ones elaborated by the University of Freiburg (Germany) for the COMPASS experiment. They are, like the ADCs continuously sampling modules.
- The Trigger electronics is based on the one from the WASA (Uppsala) and AMANDA (South Pole) experiment. As it has been developed for the WASA discriminators, some new modules, the splitters, are in our case necessary to segment the signals in an analogical and digital branch for the multiplicity trigger, the ADCs and the TDCs. The splitters also deliver partial sums from the input signals for the energy trigger sum.

General view of the crystal ball electronics:

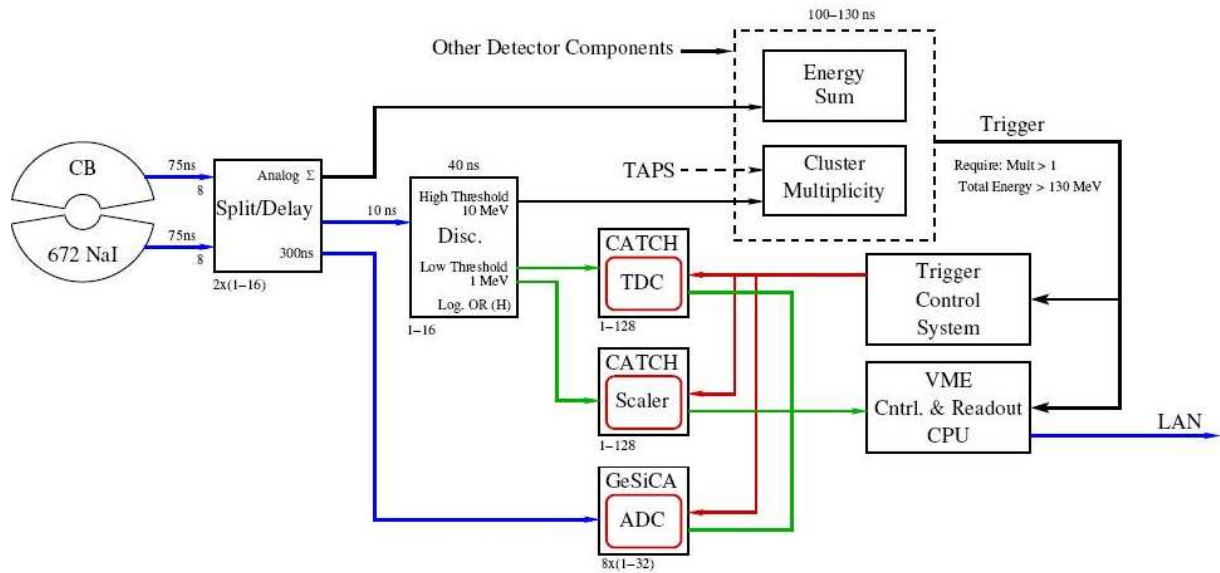


Figure 3.17: Main view of the crystal ball electronics

- The analogical signals from the photomultipliers are grouped in bundles of eight and sent to the splitter.
- The role of the **splitter** is to segment the differential input signal from the PM in two output signals. In order to be treatable for the next steps, the signals must be negative. Thereafter, the energy sums must be prepared for the *energy sum trigger*. There are 45 splitter modules, as one of these proceeds the signals of two cable bundles, i.e 16 detectors. One splitter output is sent to the discriminator, the other output to the ADCs via a delay line chips of 300ns.
- The **energy sum trigger** delivers a signal when the analogical sum of all the NaI passes over the set threshold. The up to 16 channel energy sums are delivered by the splitter and are summed in three levels via a LeCroy 428F analogical FIFO module (see fig 3.19, C). The amplitude of the total sum is about 2.5mV/MeV. The demanded threshold is adjusted with two discriminators (fig 3.19, E), one

applying a low threshold and delaying the signal, another applying a high threshold. The final energy sum trigger threshold is then reached by the AND combination of both. This discriminator combination provides a hardware reduction of the time walk effect (see [unv04]). The high threshold for the  $\mu_{\Delta}^+$  experiment is normally set by 40 MeV.

- The **discriminator** provides the signals for the trigger, the TDCs and the scalers. As the NaI crystals have a similar signal shape as the CsI(Na) crystals used in Uppsala, the same discriminators are used as the ones of the WASA experiment.

Each discriminator channel contains two *leading edge discriminators*, which are in principle based on two different thresholds, a "low" one and a "high" one.

For the  $\mu_{\Delta}^+$  experiment, the TDCs are set on the low threshold ( $\approx 2$  MeV), but still far away enough over the electronic noise. The logical OR of the signals, which comes from the higher threshold (40 MeV), is used by the Cluster Trigger and the Scalers.

- The **SADCs** have the property to continuously sample with a rate of 40 MHz and buffer the data. They are able to readout all the samples over a  $2\mu\text{s}$  period, this still allowing the reconstruction of the NaI pulse shapes.

To avoid a huge amount of data reaching the DAQ, there is an "on board integration" of the signals directly by the SADC. The boards produce integrals (sums) over three windows (see fig. 3.18): one sum of the samples *before* the scintillation pulse, one sum of the *main* part of the signal pulse and a last sum of the *tail* of the pulse. This reduces the amount of data by a factor of  $10^2$  and also allows a dynamic pedestal subtraction.

The SADC can be run in three different modi:

- The *Latch-All* modus outputs  $N$  ( $N \leq 128$ , normally  $N=90$ ) samplings and three sums in adjustable windows of the samples. This modus is used to test the ADCs and adjust the trigger.
- The *sparse* modus used by CB during our experiment only sums over parts of adjustable areas, in our case: one window from 0 to 29 (pedestal), one from 30 to 59 (signal), one from 60 to 89 (tail). Running this modus, the data delivered by a channel are thrown out, if the difference between the signal sum and the pedestal sum is lower than a definite threshold.

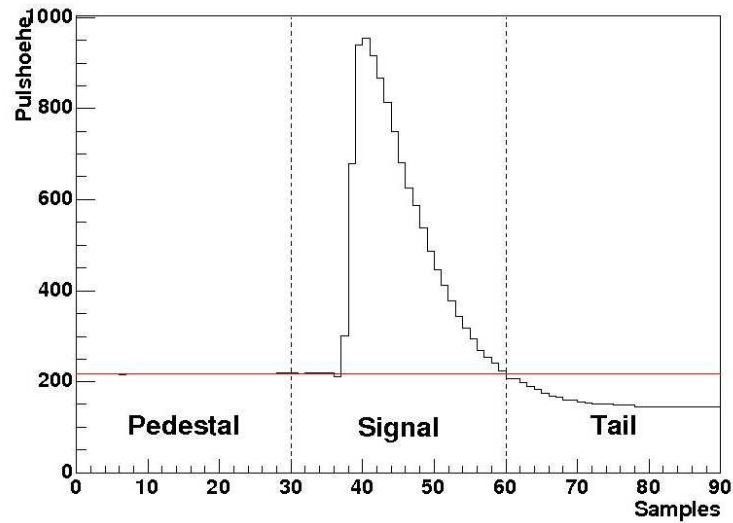


Figure 3.18: Typical SADCs pulse. For each of the three sums (pedestal, signal, tail) 30 samples are analysed. The horizontal line gives the zero position.

- The last modus is the one producing the least quantity of data. In this case, only the "pedestal subtracted" values are transferred as energy information. This modus is used for the readout of the wire chamber.

The communication with the ADCs is done via the so called *GeSica*<sup>5</sup> or also called *i-MUX* modules. They can treat up to eight data flows of the SADCs and have the following tasks:

- The sequential multiplex of the eight HOTLink<sup>6</sup> data streams
- The transformation of the data into a S-Link format
- The summarization of the TCS<sup>7</sup> events and the corresponding detector data
- The configuration of the ADC via an I<sup>2</sup> interface

The GeSicas treat the information coming from the TCS and send it further to the ADCS via an optical connection. Afterwards, for each event, the

<sup>5</sup>GEM Silicon CATCH

<sup>6</sup>High Speed Optical Transceiver Link

<sup>7</sup>Trigger Control System



GeSiCas multiplex the ADCs data and these are then sent via a S-Link card to the readout CPU.

- The **CATCH**<sup>8</sup> TDCs are TDC cards connected to CATCH modules. The CATCH module is a universal readout interface for the detector electronics. It is a 9U-VME-module providing four plugins for card inputs. In CB, the plugged cards are TDC and Scalers cards.

The tasks of the CATCH modules are the following:

- Buffer and multiplex the data of the input cards (here the TDCs and Scalers)
- Provide an universal interface for the configuration of the input cards
- Distribute the trigger signals to the input cards

There are in the CB electronics six CATCH modules, providing the handling of 768 channels. 720 channels are for the NaI, the rest is used for trigger time and the PID time information.

The TDC input cards are composed of four TDC-chips giving a deadtime free readout. The TDC works like a synchronised 16-bit counter. For each *valid* hit the counter status and the channel number are written into the buffer. Each chip has a buffer of four trigger pulses and 128 hit pulses per channel.

A hit is considered *valid*, when it is situated in a pre-programmed window before the trigger signal. When the trigger signal arrives, the trigger-offset is subtracted and then compared to the hit time. The hit is then valid if the latter *effective time* is inside a pre-defined window. In CB are the trigger-offset and the window width set to  $1.18\mu\text{s}$ . Thanks to these readout properties, the time measurement is not interrupted during the digitalising and the readout. Notice that it is important that the trigger is sent to TDCs **after** the hit time, as this is what allows a non use of delay paths.

- A **Scaler** card can also treat  $8 \times 4 = 32$  input signals. The maximal count rate is reached by 311 MHz with a width of 31 bits. Like the ADCs and TDCs, the Scaler readout does not have any deadtime, counts are continuously registered.

---

<sup>8</sup>Compass Accumulation, Transfer and Control Hardware

Each counter is composed of fast "pre-counter" (4-bit Johnson counter), whose readout is coupled with the signal frequency of the TDCs (38.88 MHz), so the status of the Johnson counter is checked every 25.72 ns. The value of this precounter is then added to the status of the slower 31 bit wide overall counter.

As only three of the four bits of the pre-scaler can be used, the Johnson counter completes its loop after eight events. This explains the mentioned maximal count rate of  $8 \times 38.88 \text{ MHz} = 311.04 \text{ MHz}$ .

- the **multiplicity trigger** is evaluated in two different levels and sent to trigger control system (TCS). The multiplicity trigger incorporates the number of wanted final particles in the readout decision. Very important for the  $\mu_{\Delta^+}$  experiment is the reliable distinction between the two final photons reaction (single  $\pi^0$ ) and the three final photons reaction ( $\pi^0 + \text{radiative } \gamma$ ) of the  $\mu_{\Delta^+}$  specific reaction. This is reached by the definition of so called *cluster areas*. A cluster area is a defined area of crystals around each crystal, which should reproduce the electromagnetic shower of a hit. (see chapter 4.4.7).

To require a definite multiplicity ( $\approx$  number of clusters  $\approx$  number of events) in the  $4\pi$  area, we have to know and combine the number of fired clusters in CB and TAPS.

For CB it is reached by first transforming the OR of the 16 signals from the discriminator  $B$  into a NIM signal. They are then collected together with the TAPS clusters (maximal 4) and treated by four LeCroy 4413 discriminators.

Under these conditions a multiplicity of  $M \geq 3$  asks for a threshold of 100-150 mV by the next coming discriminators (E).

For each measurement, to get a  $\pi^0$  for sure,  $M \geq 2$  at least is required.

- The tasks of the **TCS** are:
  - Distribute the trigger signals with the trigger offset  $< 8 \mu\text{s}$
  - Distribute the event sums for each trigger. These will be used later for the event reconstruction.
  - Provide a clock for the synchronisation of all components. This clock

has a frequency of 38.88 MHz and a precision of 50 ps RMS<sup>9</sup>.

The main part of the TCS is the controlling. It treats the data coming from the 1<sup>st</sup> level trigger logic and generates the informations to be sent to the readout modules via optical connections. These signals reach the TDC via the CATCH modules and the ADCs via the GeSiCas.

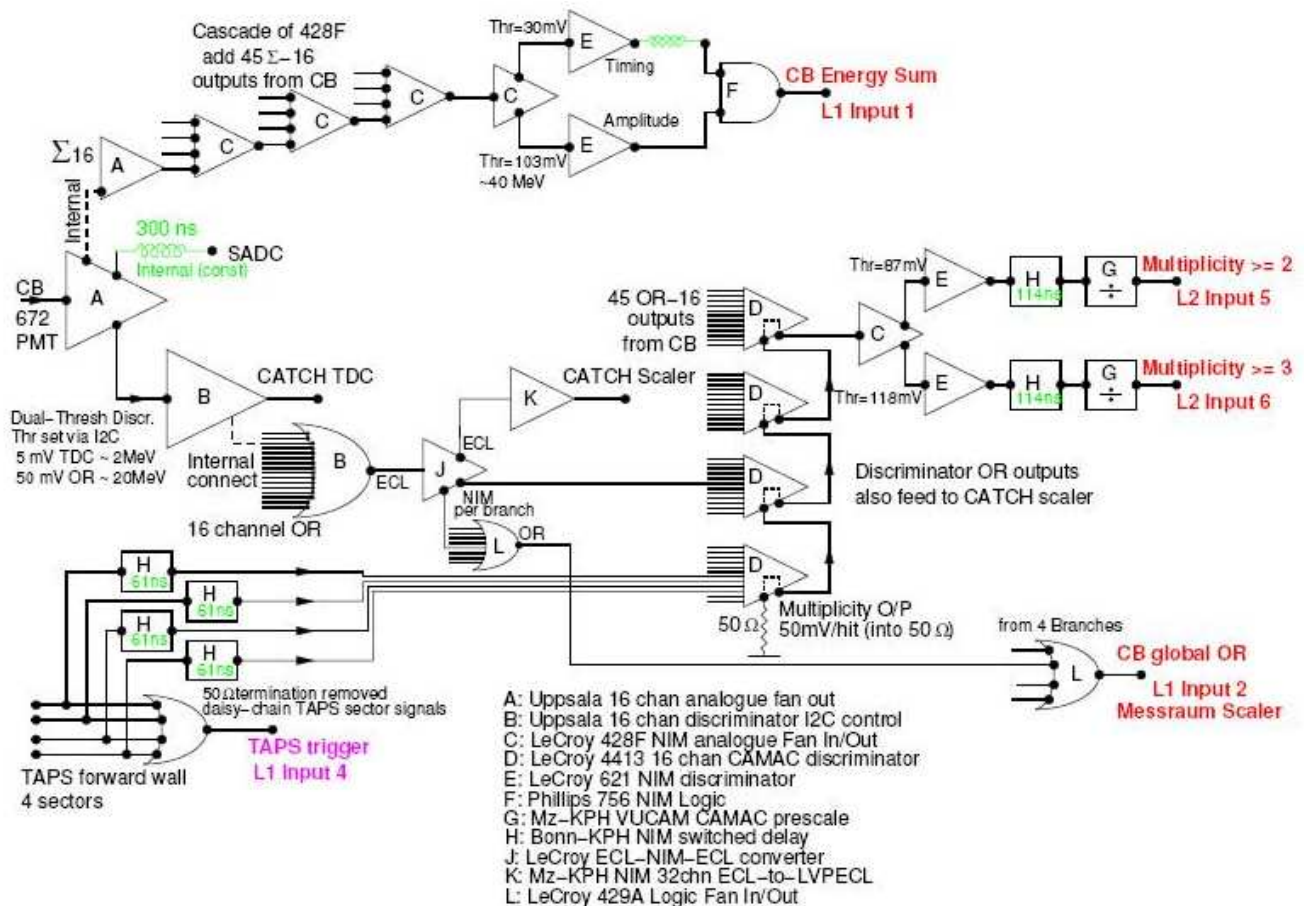


Figure 3.19: Experiment trigger (L2) and CB trigger energy sum trigger (L1)

### 3.6.2 The PID Electronics

The PID provides the time and charge information of each of its 24 scintillators. These analogue signals are first amplified by LeCroy 612 modules and

<sup>9</sup>Root Mean Square

split into an ADC and TDC branch. The signals for the ADCs are primarily delayed with 300 ns, before reaching the *FIADC 64* that have been designed for the COMPASS experiment.

On the TDC branch, on one side the *leading edge* discriminators digitize the signals above a threshold for the CATCH TDCs, on the other side an OR is built with 16 channels and sent to the experiment trigger where it may be used for calibrations measurements.

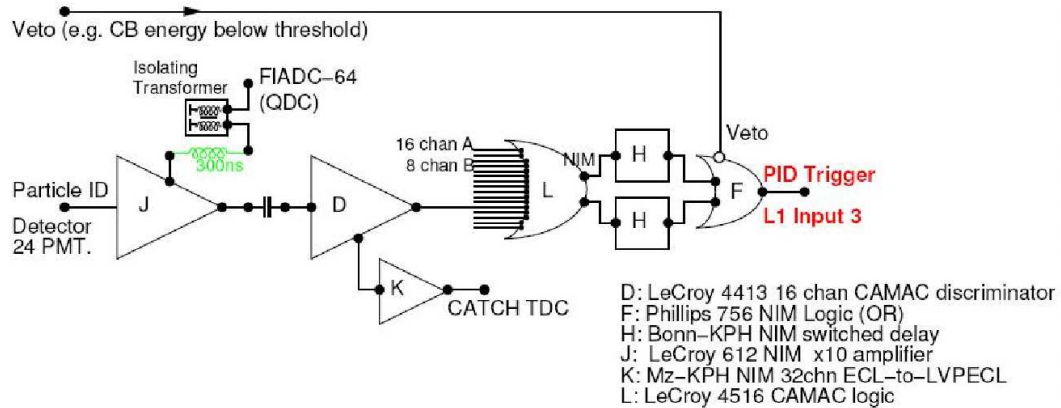


Figure 3.20: Schematic view of the PID electronics

### 3.6.3 The MWPC Electronics

The 480 wires of the MWPC are readout via four CATCH TDCs. The pulses of the 320 strips are digitized by 10 SADCs + GeSiCas modules.

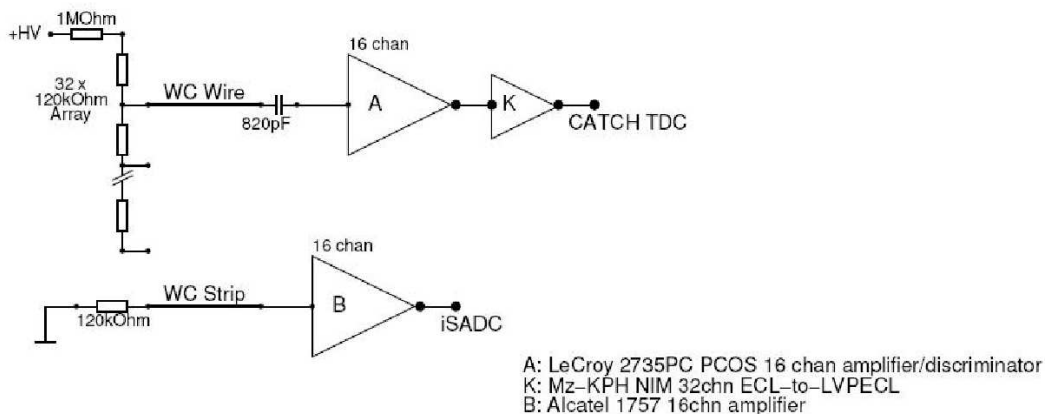


Figure 3.21: Schematic view of the MWPC electronics

### 3.6.4 The TAPS Electronics

#### Overview

The TAPS electronics has been renewed for our experiment within the PhD work of Peter Drexler [Dre04]. The main idea of the new electronics is to deal with the complete data conversion of four channels in a **single VME module**. This VME module is made of two main parts: the *Motherboard* for the digitization and the VME access and the *Piggyback* for the data collection.

#### The CAEN Motherboard

The motherboard is a slightly modified CAEN 32x analogue readout module MOD. V8741A, with the following properties:

- 28 readout channels
- fast ( $10\mu\text{s}/\text{channel}$ ) 12-bits ADC with Sliding-Scale-Technology
- programmable zero suppression
- continuous trigger counter

### 3.6.5 The TAPS Piggyback

Figure 3.22 shows the diagram for one channel of the Piggyback. The inputs and outputs on the right side are connections to the motherboard, the ones on the left side are for the external connections.

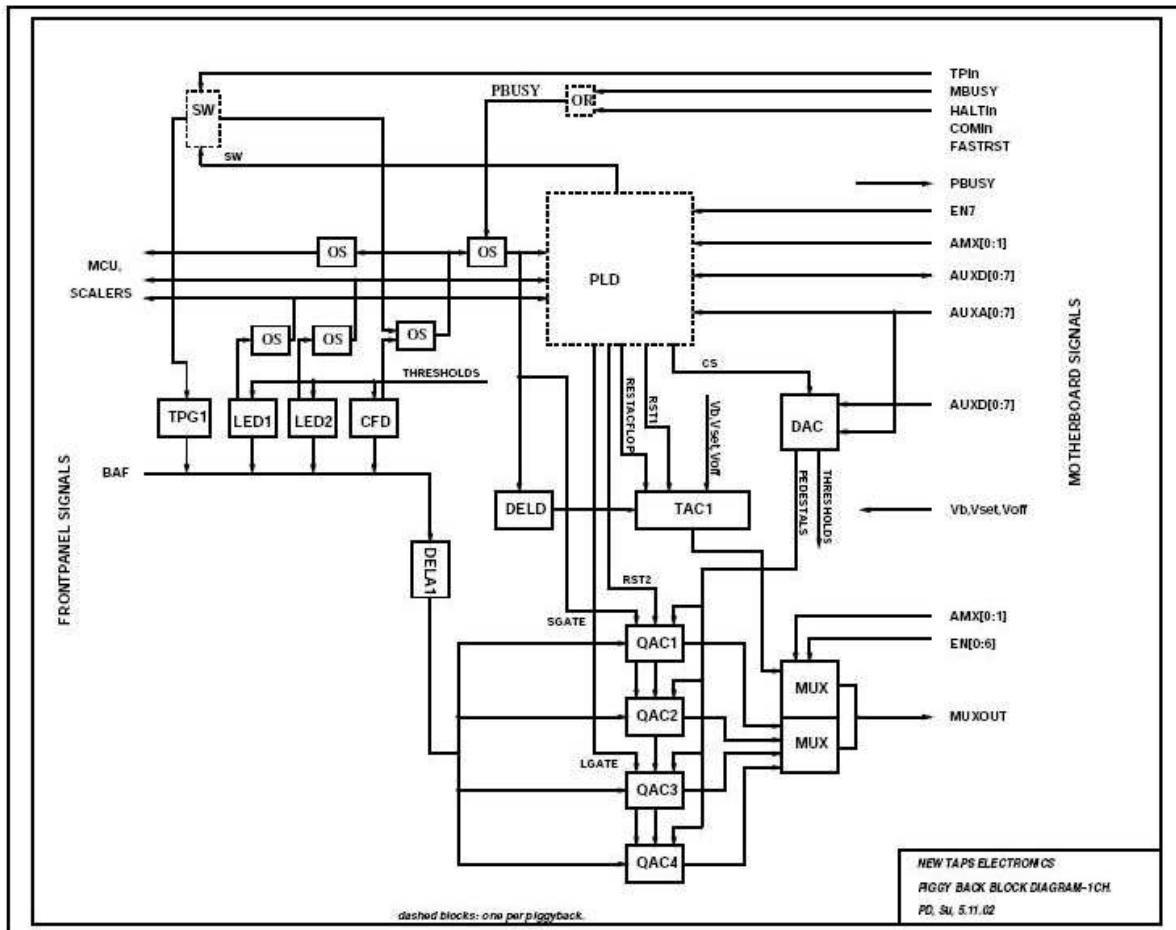


Figure 3.22: Schematic view of one channel of the Piggyback

Here the different components of the Piggyback:

- The **Active Delay/Passive Split** have the task to distribute the BaF<sub>2</sub> analogical input signals to the four Charge-to-Analog-Converter (QAC) channels.

- The **Test Pulser Generator** (TPG) present for each channel is used to test the electronics and to measure the pedestal.
- There are three **Discriminators** per channel: The *Constant-Fraction-Discriminator* (CFD), the *Leading-Edge-Discriminator* LED1 (low) and LED2 (high) for fast trigger tasks.

The CFD is set to a minimal value to identify the fired crystals. In free running integration procedure the gates are opened by the CFD signal without waiting for trigger decisions. With it, the analogue delay remains short (50 ns). The CFD, moreover, provides the individual time signal for the Time-to-Analogue-Converter (TAC) to obtain the time and energy information of all the detectors concerned by an event.

The LED thresholds may be used for the selection of high energetic photons, where the central detector collects 70% of the total energy.

The discriminators signals are needed for the *First-Level-Trigger* decision and are for this purpose buffered in an additional bit-register and adjusted via a 13 bit Digital-to-Analog-Converter (4x DAC).

Considering the long integration time for the BaF<sub>2</sub> slow components, the deadtime of all the discriminators (CFD, LED1, LED2) is set to 2.5  $\mu$ s. In case of a positive First-Level-Trigger decision, an INHIBIT signal is placed on the CFD, to avoid an additional signal to arrive during the treatment of a first signal.

- The **Gate Generator** (GG) produces long and short gates, the INHIBIT for the discriminator, and the RESET/CLEAR signals for the QAC and TAC.
- The **Energy Branch** treats the energy information via four QACs. These integrate the signals over the corresponding integration window (SGATE= 70 ns, LGATE= 2  $\mu$ s). There is an additional dynamic range, due to the fact that each gate integration is done twice with different sensitivities. We obtain therewith four final energy measurements: the Short-Gate (SG), the Short-Gate-Sensitive (SGS), the Long-Gate (LG), the Long-Gate-Sensitive (LGS). The QACs work in free-running modus with a fast RESET (RST) in case of absence of a First-Level-Trigger. Their analogical outputs are transferred via ADCs to the motherboard and are sequentially multiplexed.
- The **Time Branch** is mainly composed of the TACs, which treat the time

information delivered by the CFD conversion of the  $\text{BaF}_2$  signals into a logical signal. This signal gives the start of the TAC and the stop is given by an external box via NIM or ECL. The TACs analogical output signals are then, like the analogical QAC signals, multiplexed and digitized on the board.

### The TAPS First-Level-Trigger MCU

As shown above, the First-Level-Trigger is deduced from the three discriminators signals (CFD, LED1, LED2) coming from the Piggyback. In order to work with multihits events or coincidence/anti-coincidence conditions, we use *Multi-Coincidence-Module* (MCU). This module contains all discriminators informations of one TAPS bloc. To distinguish neutral particles from charged ones, the  $\text{BaF}_2$  signals can be compared with the VETO signals.

## 3.6.6 The Data Acquisition

### The CBDAQ

The DAQ of the crystal ball is based on the standard DAQ elements of A2:

- VMEbus computer as control system
- LynxOS as operating system
- ACQU [Ann97] as acquisition program

The CBDAQ collects the CB ADCs, TDCs and Scalers arrays and is controlled by two VMEbus, one master and one slave, communicating via VICbus (32 bit cable extension of VMEbus). The digital data first pass by the VMEs to receive the slow control functions, like the programmable threshold setting, run start and stop. They are then transferred by the master VME to the A2-counting room computer via an ethernet connection.

### The TAPSDAQ

The TAPSDAQ system is made of ten VME crates. Eight of them are for the new 4-channel readout electronics boards, the two remaining VMEs are for the trigger generation modules (MCU), the HV control modules and the VETOs, TDCs and Scalers' readout. All VMEs are equipped with a CPU board and a



specifically developed synchronisation module. The synchronisation module is responsible for the transmission of the INHIBIT signal, the trigger signal and the event number of the eventbuilder.

The system has a master/slave configuration. One CPU acts as master and together with the corresponding synchronisation module, distributes the event number to the individual slaves.

The CPU works with Linux as operating system and owns two network connections used for the slow control and the data readout. Each CPU achieves the above described eventbuilder and then sends the buffered data via TCP/IP to the data server. The data server also runs under Linux and may be run on a standard personal computer.

### The Combined CB/TAPS DAQ

The TAPS and CB information is connected to each other by the combination of their respective INHIBITS. The TAPS and CB DAQ run at the same time, they both send their data to the data server, *a2mistral*, which combines the two event streams and write them on the disk.

The online analysis run on the data server via a counting room PC is basically the online version of *AcquRoot* [Ann05]. It provides an extensive check of the data stream of the running measurement by showing the detectors basic histograms (energy, time, scalers), the status of polarization, if present, and the of prime importance *synchronisation status*. The synchronisation status is obtained by a comparison of the event number delivered by CB and by TAPS. To be synchronised the detectors are not allowed to propose event numbers differing more than one unit from each other.

### 3.6.7 Overview of the taken Data

The data used for this analysis were taken during four separate beamtimes. The first measurements were taken in July/August 2004, a second long beamtime occurred on September 2004. Two last shorter measurements were taken in January 2005. An overview of the beamtimes and their properties is shown on the following chart:

	July/August 2004	September 2004	January 2005 A	January 2005 B
<b>Beam Energy</b>	883.25 MeV	883.25 MeV	883.25 MeV	570.19 MeV
<b>Beam Current</b>	8.4 nA	11.5 nA	11.5 nA	25 nA
<b>Radiator</b>	Diamond	Diamond	Diamond	Iron
<b>Polarisation</b>	linear, circular	linear, circular	linear, circular	circular
<b>Lin. Pol. Edge</b>	440 MeV	400 MeV	400 MeV	-
<b>Tagger Channels</b>	1-284	1-284	1-284	1-284
<b>Tagger Range</b>	205-820 MeV	205-820 MeV	205-820 MeV	134-530 MeV
<b>Rrun Time</b>	370 h	190 h	120 h	120 h
<b>Trigger Level 1</b>	Sum in CB > 59 MeV			
<b>Trigger Level 2</b>	$M \leq 3$ (1/1), $M \leq 2$ (1/49)			

# Chapter 4

## Data Treatment for Analysis

The data treatment has the task to prepare the raw digital pulse heights and non synchronised times into physical data reproducing physical variables as masses, energies, etc.

The main steps to reach this goal are:

- Make the detector data reachable by an analysis interface program (here ROOT) and analysable by individual programmed codes. This step is performed by our analysis software *AcquRoot* [Ann05].
- Transform the data informations provided by the different detectors which are in channel format into physical units by performing calibrations.

### 4.1 Analysis Software AcquRoot

AcquRoot is the C++ version of the data analyser *ACQU* used within the A2 collaboration. From the start of the crystal ball experiments at MAMI, the traditional form of *ACQU* written in C/C++ has been used with a small FORTRAN interface to HBOOK. The last update of *ACQU* is the version 3V4. Starting from the 3V5 version, the new analysis program *AcquRoot* has been used.

*AcquRoot* is built on the framework of the CERN analysing program *ROOT*, C++ based suite of software tools and libraries. *ROOT* has the same properties as its predecessor, FORTRAN based, *PAW*. As *ROOT* is based on object-oriented sources, it has a broader range of functionality, better performance and its macro language recognizes most of the C/C++ commands and makes its use therefore very convenient.

### AcquRoot Software Structure

AcquRoot makes an extensive use of the facilities offered by *ROOT*. Most of the *AcquRoot* class names are derived from the *ROOT TNamed*<sup>1</sup> and can be manipulated directly via the *ROOT* macro interpreter CINT.

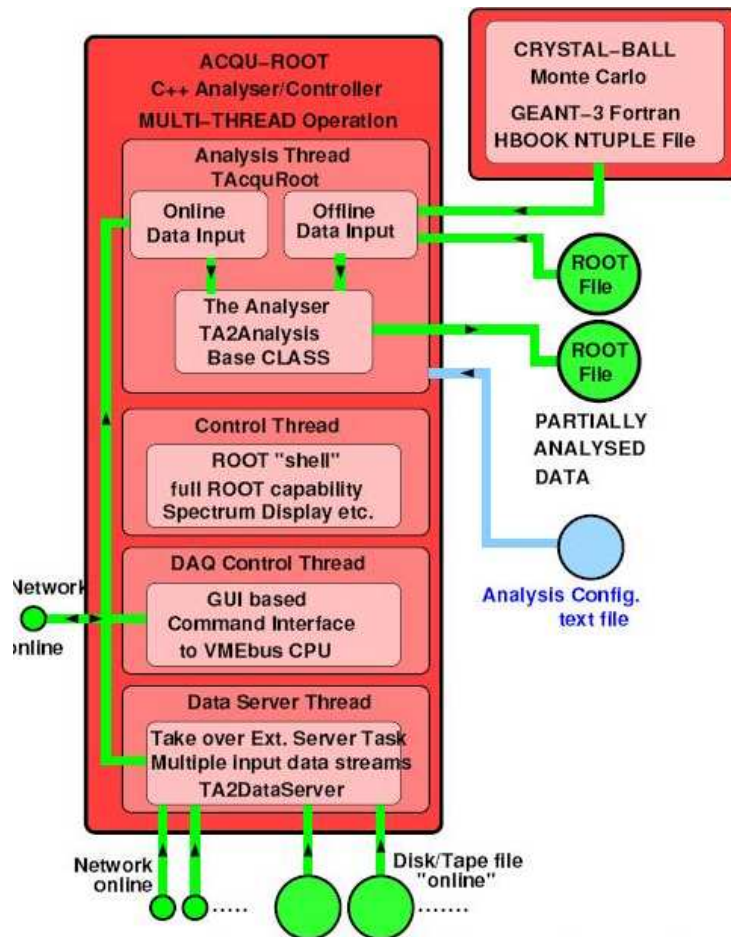


Figure 4.1: Schematic view of the AcquRoot Data Storage and Analysis System

As figure 4.1 shows, *AcquROOT* is a multithread operation analyser and controller. The main program *TA2Control* can be invoked from any *ROOT* session, but can also be compiled as an executable (used this way in the present analysis).

<sup>1</sup>Object with a character-string name

The analysis thread *TAcquRoot* is mainly run in two different modes:

- **Online** mode: It is the default mode. Here *TAcquRoot* links to the data server thread (see later). Data buffers that are in traditional *ACQU* format are read and transformed into an appropriated format.
- **Offline** mode: used for performing the full analysis of the experiment and simulated data. In this case the data server thread is not required and the events are read from a Tree File.

The specific property of the present data server thread *TA2DataServer* is the simultaneous processing of multiple input data streams. The data from TAPS and CB are sent via separate optical fiber lines to the online analysis, where the data server performs the following tasks:

- Reads all data streams synchronously and feeds data into buffer.
- Identifies and extracts simultaneous sub-events from all the streams.
- Checks the sub-event number and generates an error if they do not match.
- If the sub-events match, puts them together in a single event in an output buffer.

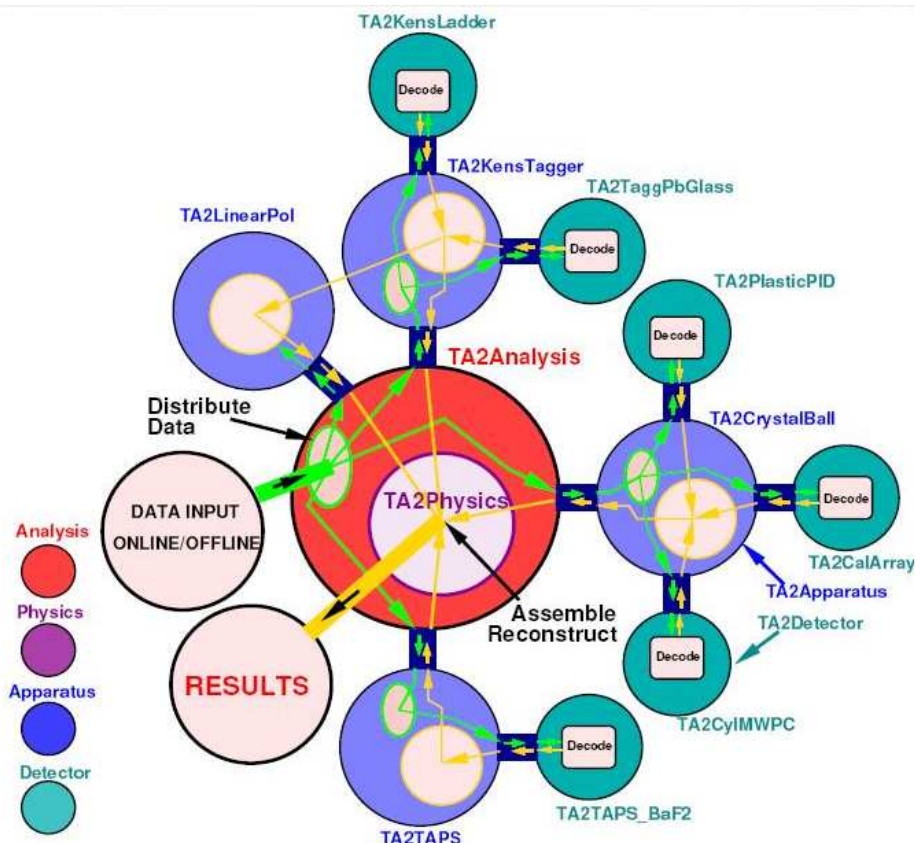


Figure 4.2: Schematic View of the AcquRoot Analyser System

The data analysis is performed by three classes. All of them are able to:

- Read in configuration data from a file or a command line.
- Communicate with the data analysis classes.
- Histogram the result for the local calculations.

The *TA2Apparatus* class corresponds to "big systems" of the experiment: the tagger system *TA2Ladder*, the crystal ball system *TA2CrystalBall* and the TAPS *TA2TAPS* system. The *TA2Detector* class which is "a child" of the *TA2Apparatus* class contents the different detectors building the experiment system like the TAPS BaF<sub>2</sub> with the TAPS Vetos, together beeing the *TA2Apparatus TA2TAPS*.

*TA2Analysis* provides the core of the data analysis system. It decodes the basic ADC, Scalers information before sending them further to the *TA2Apparatus* class which performs the basic decoding. *TA2Apparatus* reconstructs the decoded info and *TA2Physics* finally collects the information to reconstruct the event completely.

## 4.2 Tagger Data

### 4.2.1 Tagger Energy Calibration

The energy of the tagged photons is obtained by applying the formula:

$$E_{\gamma} = E_{e_{in}} - E_{e_{out}} \quad (4.1)$$

$E_{e_{in}}$  is delivered by MAMI,  $E_{e_{out}}$  is obtained by the position of the fired tagger detector. In order to establish the correspondence between the tagger channel and the associated energy, we perform in the beginning of each beamtime a ray tracing in an equivalent uniform field, monitored with a specific program called *TagCal*. This program, which may be started online [A204], is based on the NMR measurement of the tagger magnetic field and determines the energy of the recoil electron landing in the middle of each tagger detector.

### 4.2.2 Tagger Time Calibration

The tagger time calibration is performed easily: the conversion factor of each TDC channel is known (around 0.18 ns/channel) from the basic time calibration that has been performed during the installation of the tagger. The way

then to obtain a prompt peak of all TDC channels at the same position is the following:

1. Run low-intensity measurements of tagging efficiency. Thus the random coincidences are minimized.
2. Transform the tagger channel scale of the tagger TDCs into a *ns* scale using the appropriate conversion channel.
3. Fit the prompt peak of each TDC channel with a gaussian and determine the mean of this latter.
4. Apply an appropriate time offset on each TDC channel, in order to shift the peak position to the chosen arbitrary prompt peak position.

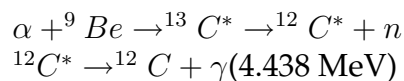
The obtained clean tagger time peak will be used to perform the random events subtraction (see chapter 5.2.1).

## 4.3 Crystal Ball Data

### 4.3.1 Crystal Ball Energy Calibration

The range setting and the energy calibration in the crystal ball could not be performed with the use of cosmic rays, due to the the varying orientation of the crystals in space. After several tests [unv04], the range setting has been finally accomplished with a combined  $^{241}\text{Am}/^9\text{Be}$  source. This combination offers a neutron source with continuous spectra up to 10 MeV and a photopeak at 4.438 MeV:

- $^{241}\text{Am}$  is an  $\alpha$  - emitter: 85.2 % at 5.486 MeV, 12.8 % at 5.433 MeV
- $^9\text{Be}$  is an  $\alpha$  - absorber:



The photopeak has been fitted with a gaussian + exponential function and the PMT's voltage adjusted, in order to get the peak within 20% of the range's mean.

The NaI energy calibration has been performed via the analysis of the single pion channel:

$$\gamma p \rightarrow \pi^0 p \rightarrow 2\gamma$$

Knowing the photon beam energy, the exact target mass and the  $\theta$  angle of the pion, the CM energy of the two final photons can be theoretically determined. The comparison of the obtained energy channel for a final photon and its calculated energy gives a first *MeV/Ch* value and the repetition of about five such iterations delivers the final NaI energy calibration.

### 4.3.2 Crystal Ball Time Calibration

The CB time alignment is done together with the *walk-correction*. The latter is the compensation of the recorded time difference between signals with different pulse heights.

For this purpose, as for the energy calibration, we use the single  $\pi^0$  channel. The time of the  $\pi^0$  decay photons is plotted against their deposited energy (see fig. 4.3). We then determine the maxima of multiple vertical slices and finally plot the 2D shape with the following function:  $f(y) = p_0 + p_1(1 - \sqrt{p_2/2})$  where the offset is adapted with  $p_2$ .

Applying the "inverse" function to arrive to a horizontal distribution, we typically obtain the result shown on the right side of figure 4.3. A detailed description of the *walk correction* follows in the chapter 4.4.9.

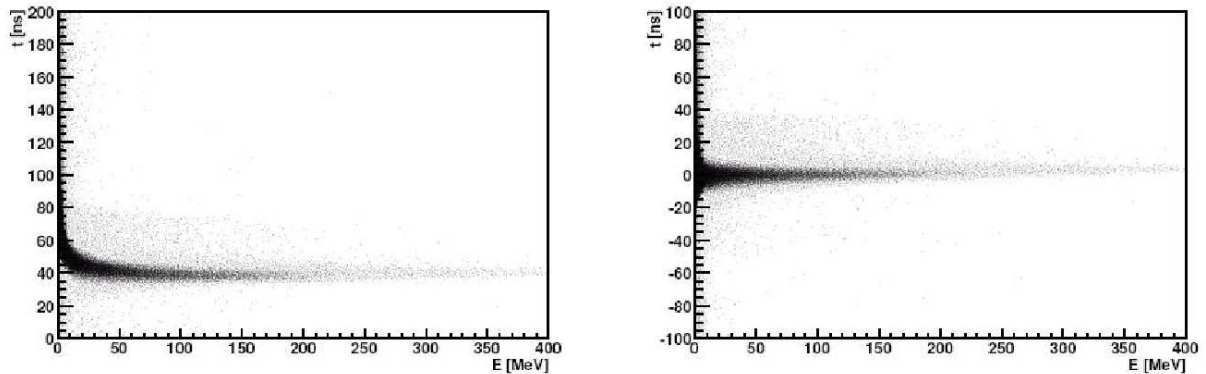


Figure 4.3: 2D walk and alignment CB time. LEFT: Before correction, RIGHT: After correction



### 4.3.3 The PID Calibration

In addition to the time and energy calibration, the PID needs a position calibration to be able to synchronize hits from their scintillators with the NaI hits and to construct the  $\Delta E/E$  ratio. This position calibration is carried out on the angle  $\phi$  in two steps:

1. Plot in a 2D histogram the PID channel versus the  $\phi$  angle of the NaI for synchronized events built of one hit in the PID and one in CB (see fig 4.4). Starting from this, we directly locate a first approximation of the  $\phi$  angle corresponding to each PID channel.
2. We then look at the projection of the above described 2D plot for each PID channel and fit the highest peak with a gaussian.

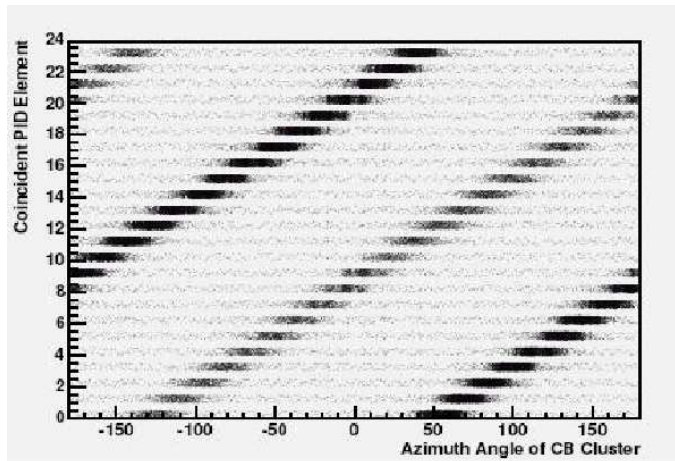


Figure 4.4: Calibration of the angle  $\phi$  in the PID

The PID energy calibration is achieved by simulating events with one low energy peak (typical for charged pion) and one high energy peak (typical for proton), fitting the two peaks and determining the energy range in between. We then consider similar plots of the PID with real data and adapt them to the results found in the simulations.

The PID time calibration is easy to perform, as its time is delivered by CATCH TDCs whose time/channel ratio is well known. The alignment is easily done as the time peaks are very sharp (time resolution of  $\approx 5ns$ ).

### 4.3.4 The Wire Chamber Calibration

The intrinsic angular resolution of the MWPC is determined by the analysis of cosmics measurements. Each cosmic hit delivers 4 intersection points and two tracks, as shown on figure 4.5. As muons travel on a straight path, the applied condition to obtain the  $\theta$  and  $\phi$  resolution is the collinearity of the two tracks. Resulting resolution:  $1.8^\circ$  for  $\theta$  and  $1.33^\circ$  for  $\phi$ .

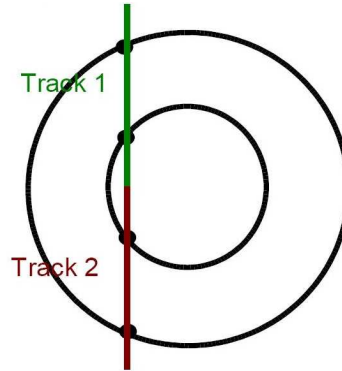


Figure 4.5: MWPC Calibration tracks and points with cosmics

The efficiency of minimal ionising particles has been also determined by using cosmics and delivered the value of 81.2 %. The proton efficiency of 89.7 % (July 04 data) has been determined via the well known single  $\pi^0$  channel. The charged pion's one of 79.3 % was reached by the use of the  $\gamma p \rightarrow n\pi^+$  channel. The difference between the proton and charged pion efficiency is due to the higher ionisation density of the proton in the chamber gas.

## 4.4 The TAPS Data

### 4.4.1 The TAPS Energy Calibration

The TAPS energy calibration is performed by using cosmics measurements taken at the beginning and at the end of each beamtime.

As the combination crystal-photomultiplier-electronic delivers a linear correspondance between energy and pulse height, we only need two energy reference points to find out the two calibration factors: `gain` and `offset`. The gain is given in MeV/Channel and the offset corresponds to the pedestal position in channel units.

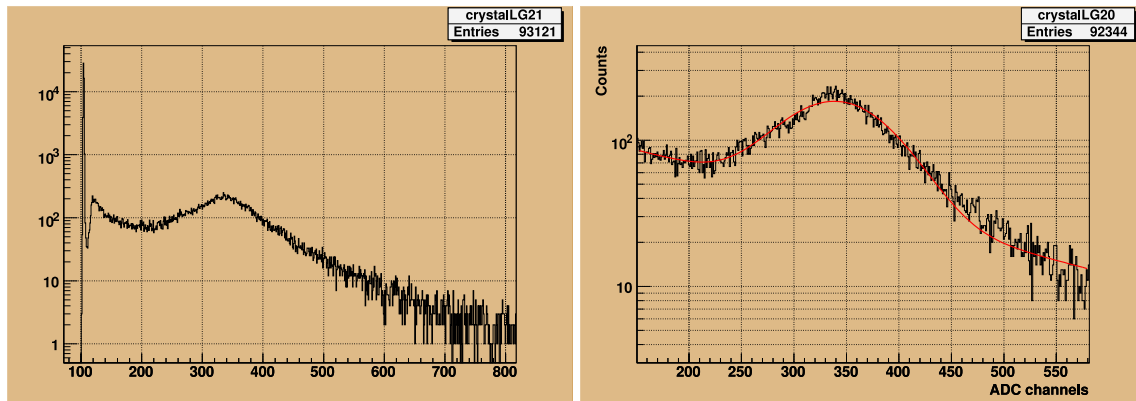


Figure 4.6: LEFT: Example of a cosmic spectrum, RIGHT: Fit of a cosmic spectrum for the determination of the peak position

To obtain a precise pedestal position, we use an electronic pulser-trigger and therewith determine the position of the "0 MeV", delivering the first calibration point.

The second point is then given by the position of the cosmic peak corresponding to the well known energy deposition of minimal ionising muons. This value has been specifically determined for the TAPS BaF<sub>2</sub> crystals as 37.7 MeV.

Practically, the pedestal position is determined by registering the first highest channel of the spectrum before decreasing again. The cosmic peak position is determined by a `gauss + exp` fit, as shown on figure 4.6, RIGHT.

#### 4.4.2 The TAPS Time Calibration

The TAPS time calibration is achieved by plotting for each BaF<sub>2</sub> the difference of its time with the one of a single photon tagger channel. Then all these spectra are fitted with a gaussian and the position and the mean of the peak are determined. Finally all the time plots are shifted to the same arbitrary position (see fig 4.7).

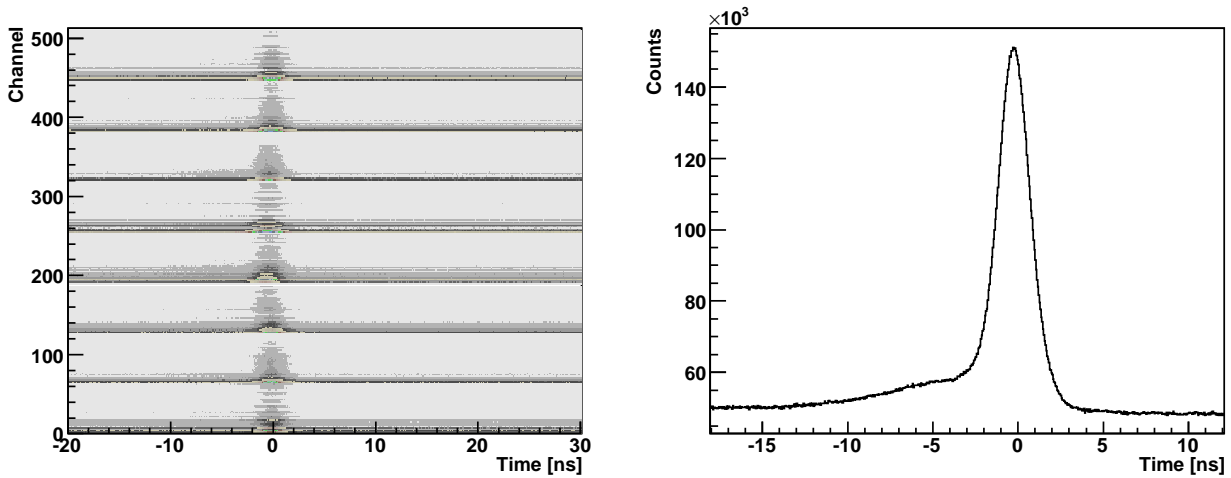


Figure 4.7: LEFT: Alignment of the time of the TAPS crystals. RIGHT: Single crystal time (difference BaF<sub>2</sub>-Tagger) and gaussian fit

### 4.4.3 The Response Measurement and Cosmics Calibration

The goal of a response measurement is the check of the photon shower in our crystals by throwing photons in one crystal and look at the energy deposited in the crystals around.

Before looking at the photon data, we first have to set the range of the detectors and calibrate them. The range setting is described in a later part.

The setup for the response measurement is a "Mini-TAPS" including 36 crystals. The photon beam collided the center of this Mini-TAPS with three different energies.

We study for this response measurement three different photon spectra: The first one is the spectrum of the central detector only (detector 36), which is the target of the photon beam. The second one is a spectrum where for each event the energy deposited in the central crystal and in the six crystals around are added. The third one is the energy summation of 19 crystals, i.e. the central crystal plus the two crystal rings around.

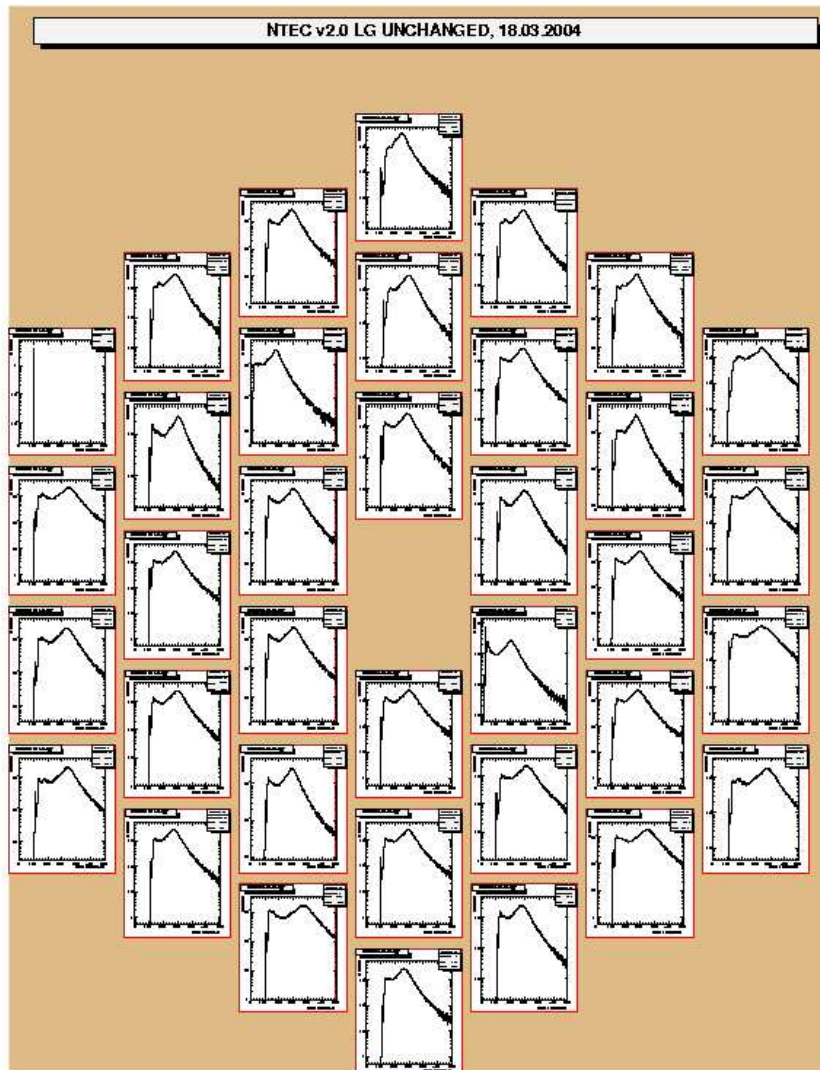


Figure 4.8: Mini TAPS. Notice that the center is in reality not empty as it appears on the picture, but a detector carrying the label "36" is in this central position.

Figure 4.9 shows the two first spectra. The black spectrum shows the energy of the central detector only and the red one the energy sum of seven detectors, i.e. the central crystal and the ones of the first ring around.

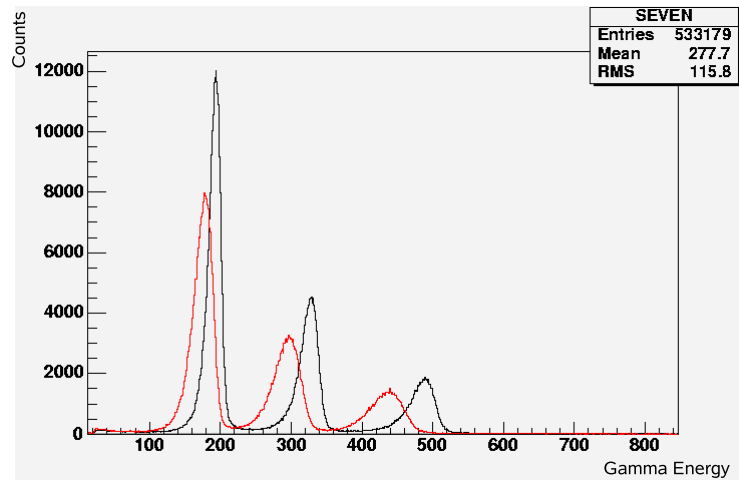


Figure 4.9: TAPS response with two rings

Notice a shift to the right in the red spectrum, self-evident due to the sum of energies collected for each event. We also observe that the peaks are narrower in the 7-detector spectrum. This is exactly the expected effect, since we are in this case closer to the well defined, real photon energy.

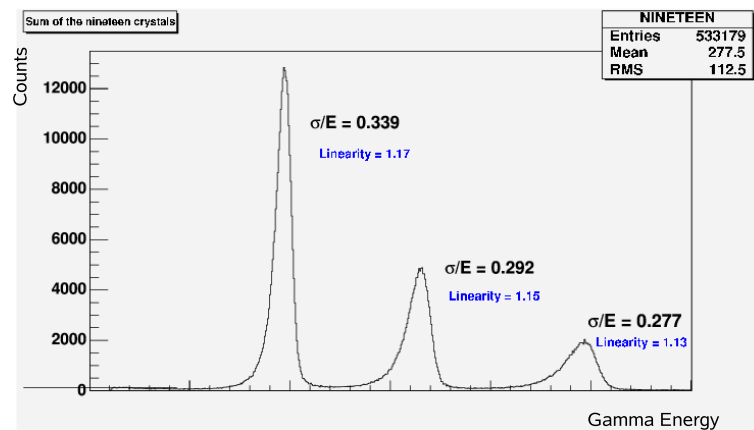


Figure 4.10: TAPS response of three rings (19 crystals)

Figure 4.10 shows the last spectrum, i.e the three energy peaks of 19 crystals together. We expect here even narrower peaks and this actually is the case.

Since the detectors are calibrated and so give MeV on the x-axis, it is possible to calculate the resolution  $\sigma/E$  and so make a comparison with theoretical values. Our results for  $\sigma/E$  are around 10 % worse than the ones measured by Gabler et al.[Gab93], this remains acceptable.

#### 4.4.4 The Range Setting

The aim of a range setting is to obtain, with the provided 3800 channels of a QDC, a range of 600 MeV after calibration. This is accomplished by the use of cosmic measurements. We register the pedestal and cosmic peak position and adjust the PMT's high voltage in order to obtain the corresponding channel number between these two positions. It is an iterative procedure that had to be done around three times to arrive at the satisfactory spectrum alignment shown below.

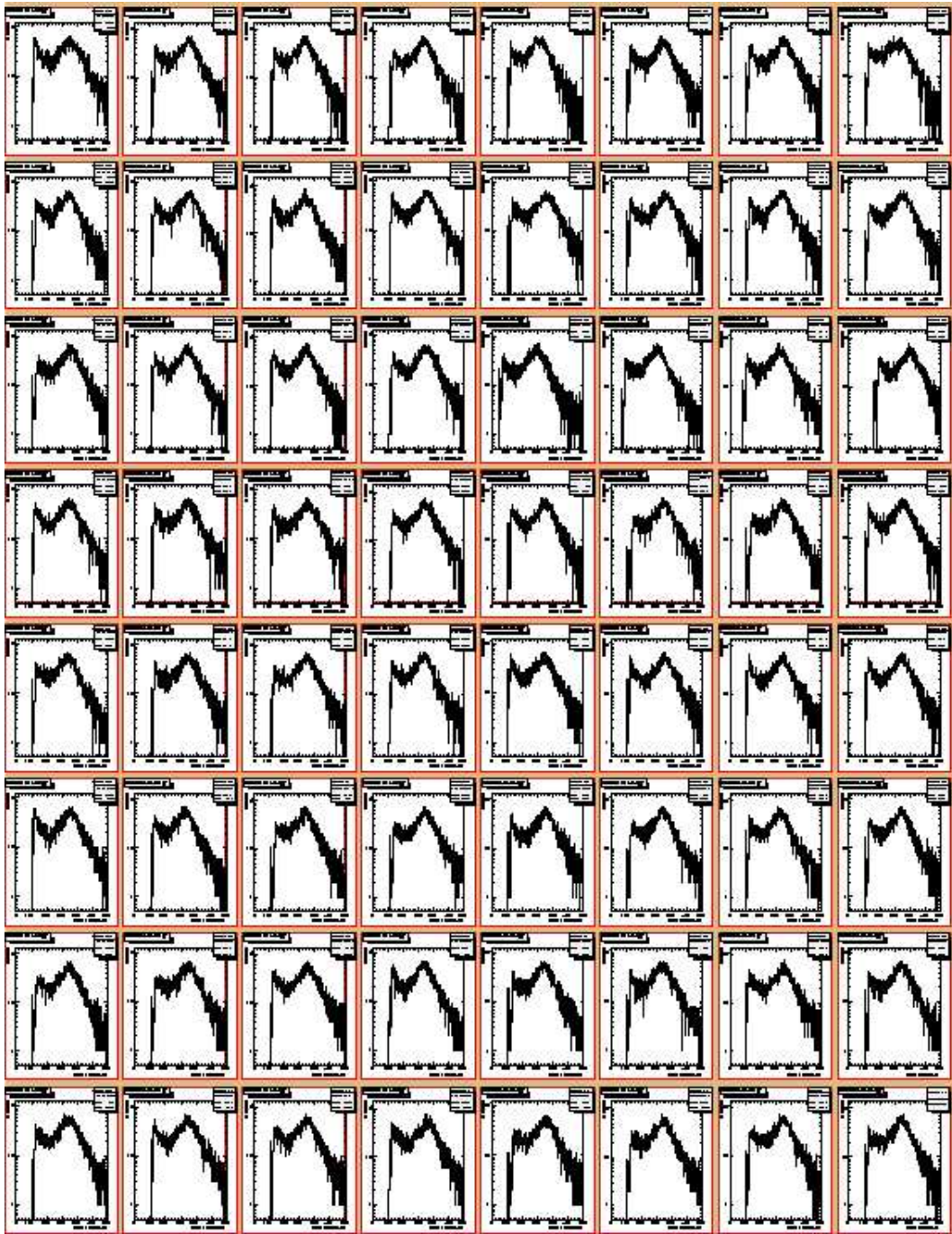


Figure 4.11: One "bloc" of TAPS: 64 BaF<sub>2</sub> crystals



### 4.4.5 The Determination of the LED Threshold

The determination of the LED threshold is done by using a comparison between spectra considering the LED condition and spectra ignoring it.

The energy threshold of the LED discriminators is part of the trigger conditions and must be, according to this, precisely known and set before starting the measurements. Therefore, a calibration delivering a proper relation between the mV scale of the electronics and the corresponding energy threshold in MeV coming out of the QDC has to be performed.

This calibration is realized by using, for each QDC channel, the comparison between an energy spectrum where the LED-threshold is taken into account and one where it is ignored (see fig. 4.12, LEFT). The precise determination of the LED threshold position is reached by building the ratio of these two spectra and requiring a nearly to one (0.99) value (see fig. 4.12, RIGHT).

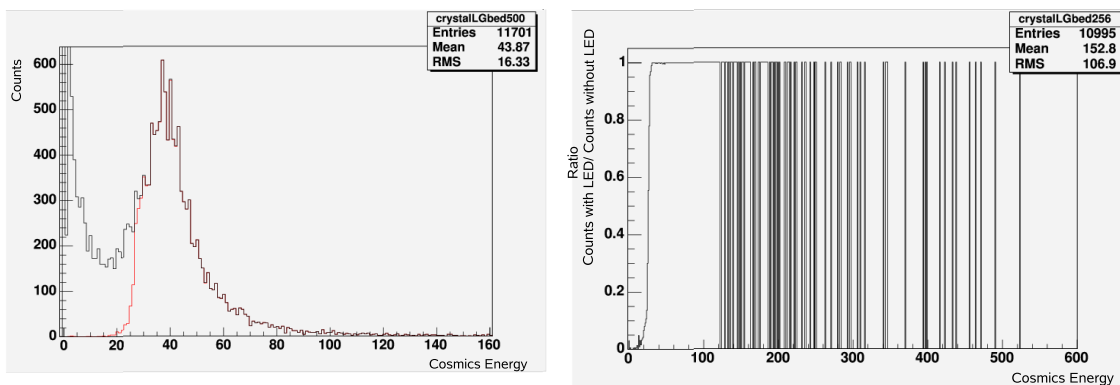


Figure 4.12: LEFT: Spectra considering/not considering the LED threshold. RIGHT: Ratio of the two left spectra

This procedure is repeated with four different voltages of the LED discriminator (50mV, 100mV, 150 mV, 200mV). The so obtained four points permit a linear fit and so a trustable conversion function from the wished threshold in MeV and the hardware setting in mV.

### 4.4.6 The TAPS Particle Identification

The particle identification in TAPS is established by combining three informations: The *Pulse Shape Analysis (PSA)*, the *VETO* signals and the *Time of Flight* of

the particles.

The different steps to use the PSA information are the following:

1. Produce calibrated BaF<sub>2</sub> energy plots.
2. Plot the  $E_{LongGate}$  signal versus the  $E_{ShortGate}$  signal (see fig. 3.14) and define polar coordinates on the plot:

$$R = \sqrt{E_{LG}^2 + E_{SG}^2} \text{ and } \phi = \arctan\left(\frac{E_{SG}}{E_{LG}}\right) \frac{180}{\pi}$$

3. Plot  $\phi$  [°] versus R [MeV] and define projections on the Y-axis from 10 to 600 MeV.
4. For each projection, identify the areas corresponding to the specific particles. This is obtained by fitting the main photon peak with a gaussian and defining a limit,  $3\sigma$  apart of the peak position. Particles with a  $\phi$  under this limit are considered as heavy and, depending on the VETOS information, are identified as proton or neutron. Particles with a  $\phi$  over the limit are considered as light particles and identified as photons or electrons, depending on the corresponding VETO information.

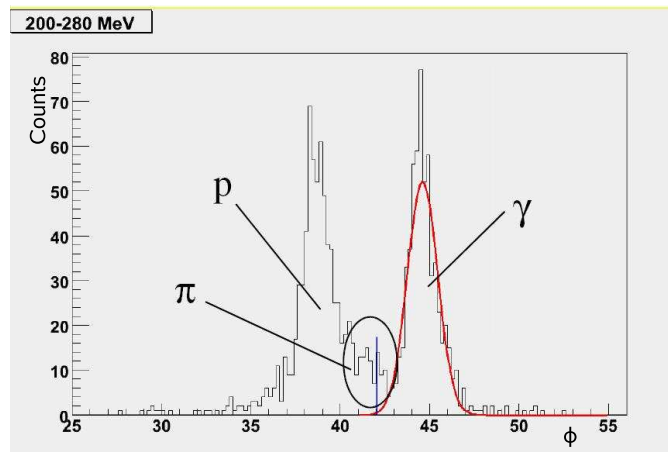


Figure 4.13: PSA step: One of the multiple projections of the  $\phi$  distribution with the identified particle areas.  $\phi = \arctan\left(\frac{E_{SG}}{E_{LG}}\right) \frac{180}{\pi}$

The time of flight information (TOF) is obtained by considering the time difference between the BaF<sub>2</sub> and the tagger and plotting this latter against the BaF<sub>2</sub> hit energy. A specific *proton area* is then identified and used for the ultimate decision of a proton identification.

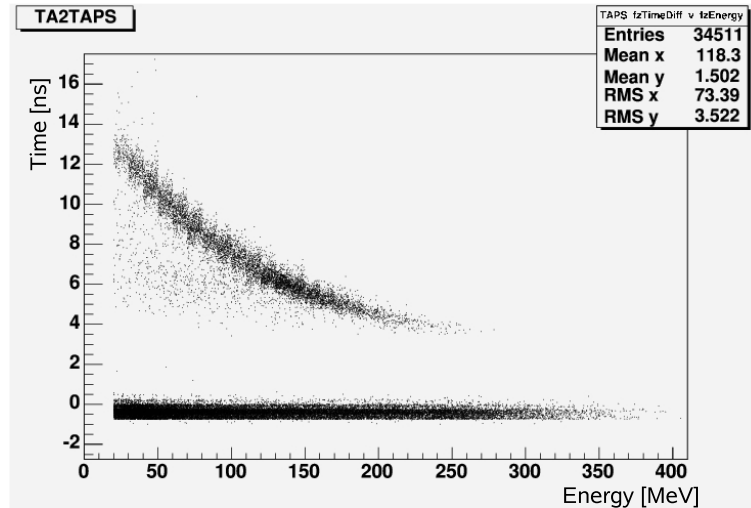


Figure 4.14: Typical Time Of Flight distribution

#### 4.4.7 The Cluster Algorithm

As already mentioned in the electronics part of this work, the relevant information delivering the number of particles in one event is not the number of hits, but the number of *clusters*.

Due to the fact that the particles generate electromagnetic showers in the detectors and therefore generally distribute their energy in not only one, but several crystals, we need to collect the energy deposits in all the crystals fired from the considered particle, in order to reconstruct its energy.

The cluster algorithm is of high importance, as it decides, either to group together or split clusters from each other and thus deliver a  $i - 1, i$ , or  $i + 1$  particles event. This decision is particularly crucial in this work, as the studied reaction differs only by one particle from the two background reactions.

The cluster algorithm is performed by the following several steps:

1. In the list of fired crystals, we select the crystal with the maximal deposited energy. This one is accepted as the center of the cluster

C1.

2. Scanning the neighbours of the central crystal (6 neighbours in TAPS, 12 in the CB), we "move" them to the *C1 list*, if their energy deposit is not zero.
3. Looking at the *neighbours of the neighbours* we move them to *C1 list*, if their energy deposit is not zero.
4. When no additional *neighbours* are found (with  $E > 0$ ), the cluster *C1* is considered as complete. We come back to point 1. and determine in the remaining members of *list of fired crystals* a new maximal energy crystal that will be the center of cluster *C2*.

The TAPS and CB cluster algorithm differ only at point 3. This iterative "next neighbour" scan is accomplished per default in TAPS and stops only if a crystal with a zero energy deposit is found. The NaI setup files offer the opportunity to "tune" the algorithm. The user can define a limit of the neighbour's iteration, either by defining a limit radius of the cluster, or by setting a maximal number of iterations. It is also possible to completely switch off the iteration process 3. and only accept the very next 12 neighbours of the central crystal. After a meticulous study this latter option has been chosen. The effect of the infinite iteration in TAPS can be clearly observed:

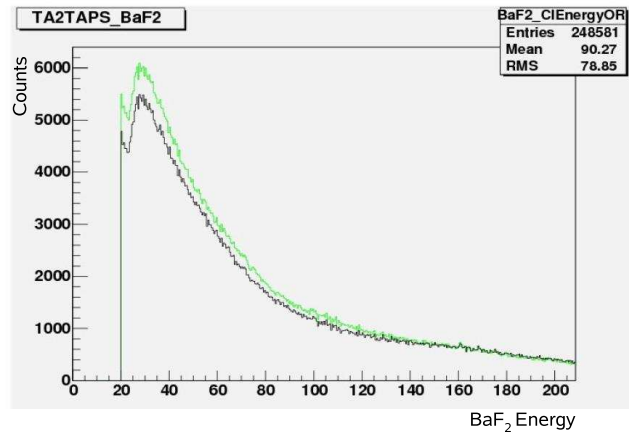


Figure 4.15: The difference in the cluster energy by infinite iteration of the next neighbour (green) and limited to very next neighbours cluster size

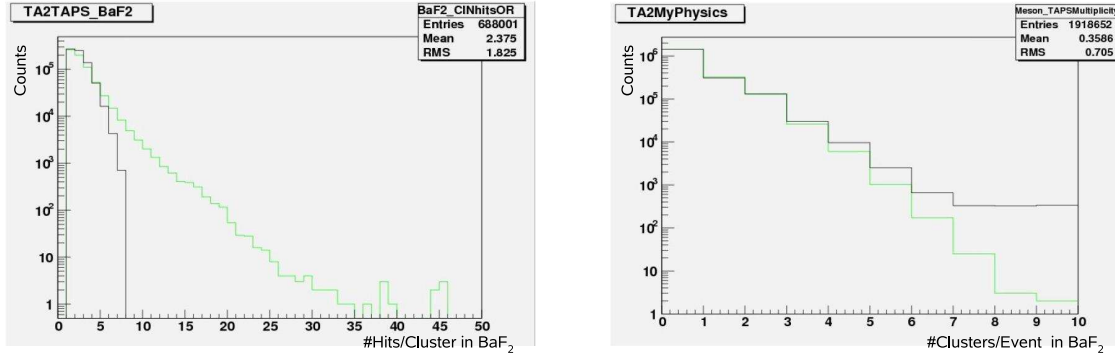


Figure 4.16: Effect of the infinite iteration in TAPS. LEFT: Number of fired crystals in a  $\text{BaF}_2$  cluster. RIGHT: Number of clusters in an event. The colors correspond to the ones of picture 4.15

The time of the cluster is the time of its central crystal. The energy of the cluster corresponds to the sum of the energy deposits in the cluster's members. The cluster position is obtained by first giving a "weight" to the crystals, depending on their energy contribution and then building the mean of the so weighted crystal positions.

#### 4.4.8 The Proton Energy Correction

As protons do not interact the same as photons with the crystals, their corresponding energy delivered by the reconstruction of the electromagnetic shower in the detector is not exactly reproduced. As a matter of fact, protons lose more kinetic energy by travelling through material than photons. Also the shower they produce in the detectors is most of the time concentrated in one crystal, thus much less broader than the photon's one.

The correction applied on the proton energy is obtained by using the reaction channel  $\gamma p \rightarrow \pi^0 p$ . The kinematics of a 2-body decay being very well known, we can reconstruct the theoretical 4-vector of the proton using the informations of the photon beam, the target and the  $\pi^0$ :

$$P_{p,cal} = \begin{pmatrix} E_\gamma + m_p - E_{\pi^0} \\ -p_{\pi^0}^x \\ -p_{\pi^0}^y \\ E_\gamma - p_{\pi^0}^z \end{pmatrix} \quad (4.2)$$

As the energy spectrum of the proton also varies with its azimuthal angle  $\theta_p$ , correction factors have to be determined for each  $\theta_p$  range. Thus, for each 2-degrees  $\theta_p$ , a 2D-plot is produced, representing on the x-axis the measured energy of the proton, on the y-axis the difference between the measured and calculated energy of the proton:

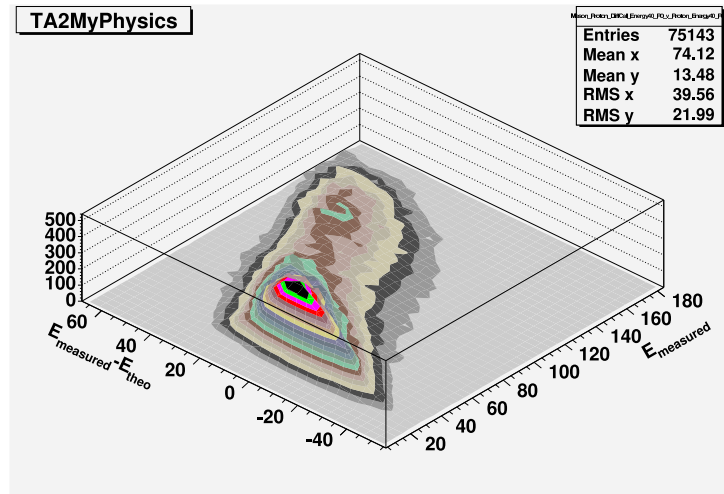


Figure 4.17: Example of 2D plot used for the proton energy correction. If the energy was perfect, we would have a straight horizontal line at 0. This plot includes protons with an azimuthal angle  $\theta_p$  between 40 and 42 degrees.

Starting from the 2D plot shown above, projections on the y-axis are produced and fitted with a gaussian to obtain their peak position. These positions are then plotted on the 2D frame and fitted with a  $P3$  function:

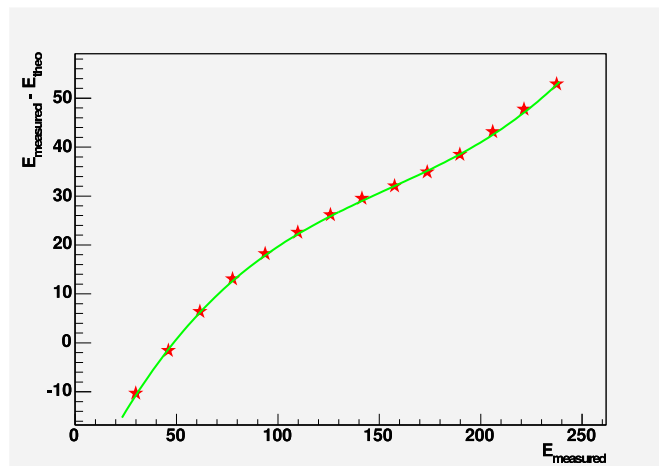


Figure 4.18: Example of  $P3$  fit applied for the proton energy correction. Compare with the shape on figure 4.17

The parameters of the function corresponding to each  $\theta_p$  angle are finally stored in a file and provide for each proton energy the offset that must be subtracted from the delivered energy value.

#### 4.4.9 The Walk Correction

The time signal elongation due to the height of the raw pulse signal is called the *Walk Effect* (see fig. 4.19). This effect could be neglected in TAPS thanks to the CFD threshold. It has however been corrected for the crystal ball within the student's work of Marlon Horras in Basel [Hor06].

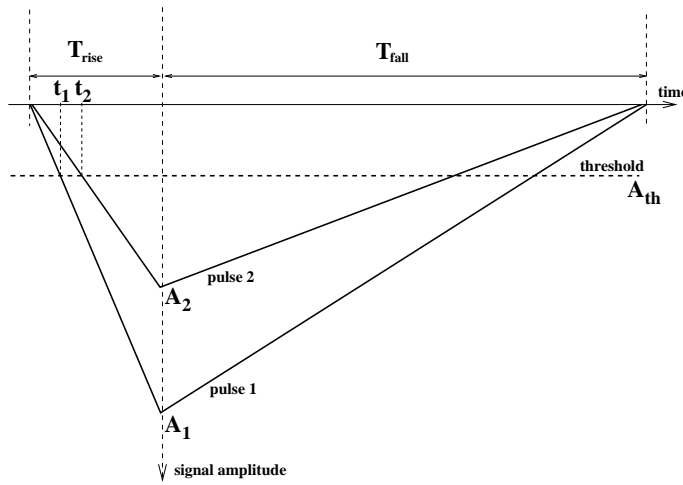


Figure 4.19: Time variation until reaching the threshold, depending of the signal amplitude

The times  $t_1$  and  $t_2$  are delays on the real start time  $t_{ideal}$  and are called  $t_{walk}$ . The bigger the energy, the smaller  $t_{walk}$ .  $t_{ideal}$  can be determined as it follows:

$$t_{ideal} = t_{measurement} - t_{walk} \quad (4.3)$$

$t_{walk}$  can be expressed as a function of the signal energy:

$$t_{walk} = p_1 + p_2 \cdot E^{p_3} \quad (4.4)$$

The formula was found empirically, the parameters  $p_1$ ,  $p_2$ , and  $p_3$  can be determined with a fit using CB data.

For this purpose, a simple analysis of the single  $\pi^0$  has been used with the following properties:

- Accepting events made of exactly 3 clusters, all found in crystal ball
- Knowing well the kinematics of the  $\gamma p \rightarrow \pi^0 p$  reaction in the CM, the proton and the  $\pi^0$  should be emitted in inverse direction. Thus, only events are accepted where the difference of the azimuthal angles of the proton and the pion are between 170 and 190 degrees
- A cut on the invariant mass of the reconstructed pion is done between 110 and 160 MeV

The fit is then done for each of the 720 crystal ball detectors, on a 2D plot:  $t_\gamma^{CB}$  versus  $E_\gamma$ . See figure 4.20:

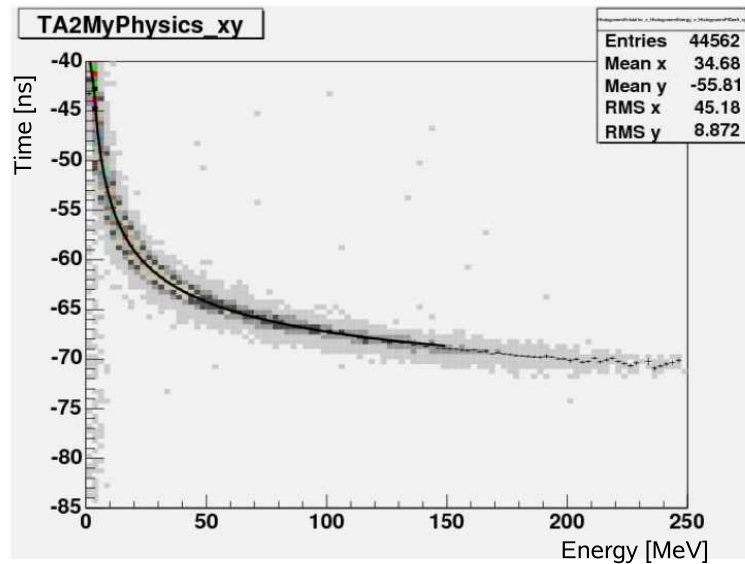


Figure 4.20: Time in CB versus energy deposited in crystal, example of one crystal before Walk correction. The applied fit is shown.

The result, i.e a total independance of the time to the pulse-eight, i.e the energy deposited in crystal can be observed on figure 4.21.



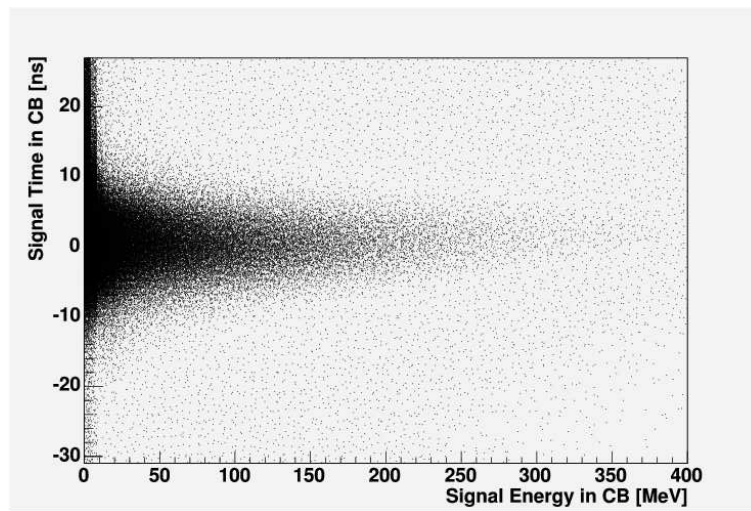


Figure 4.21: Time in CB versus energy deposited in crystal

#### 4.4.10 The Tagger Structure Correction

A structure on the tagger spectrum has been systematically observed, could however not be explained. Instead of being flat, the tagger scaler distribution shows clear separated groups of always four channels. See figure 4.21. This effect is treated in the analysis using the ratio of the tagger TDC channels in a tagger background area, i.e., where there is no bremsstrahlung influence, and the electrons spectrum. This ratio should be flat and constant.

The correction was applied by norming for each group of channels the highest one to a ratio of one. The obtained new ratio spectrum is finally multiplied channel by channel with the tagging efficiency.

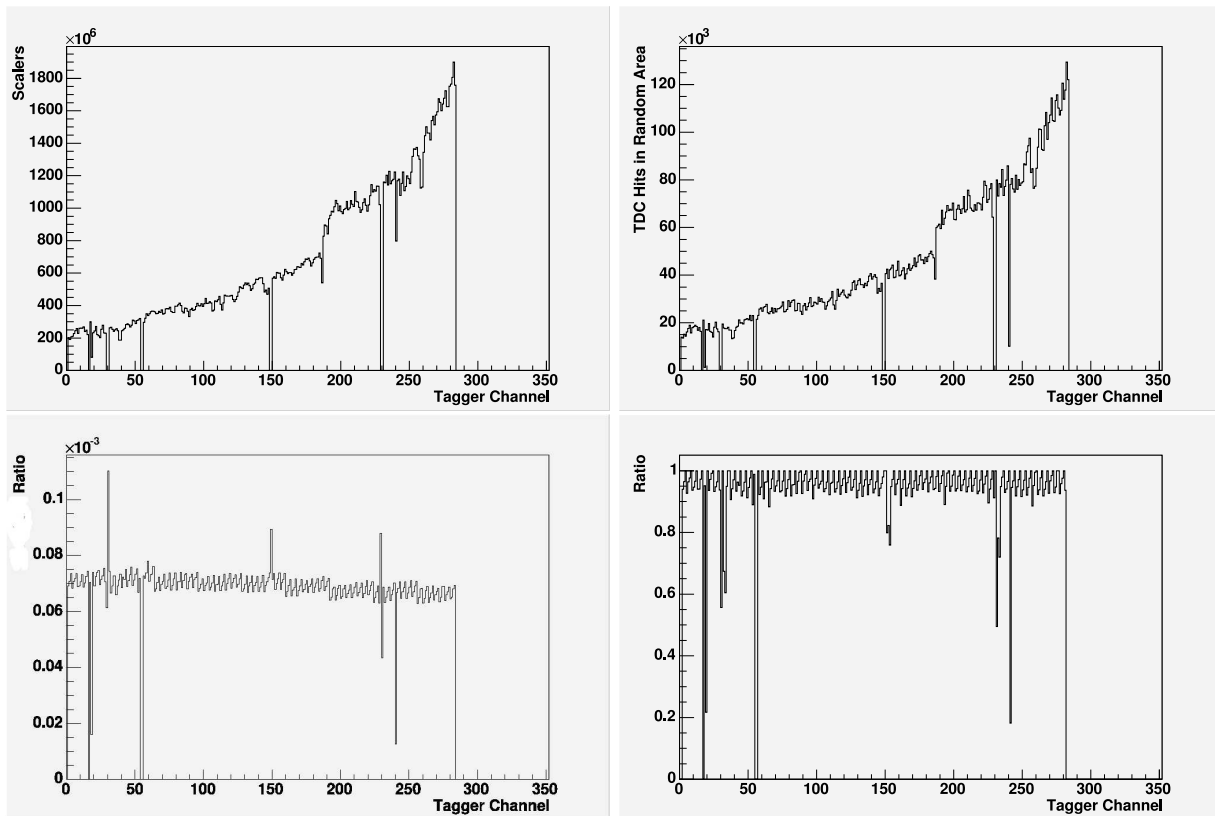


Figure 4.22: UP LEFT: The Electron Tagger Spectrum. UP RIGHT: The Tagger TDC hits in background area BOTTOM LEFT: Ratio of the upper two distributions. BOTTOM RIGHT: Final weighted Ratio.

# Chapter 5

## Analysis

The aim of the present analysis is to provide reliable and precise enough physics variables for a comparison with theoretical models and so allow the extraction of the  $\Delta$  magnetic dipole moment  $\mu_{\Delta^+}$ . These variables are **Cross Sections** and **Asymmetries**.

Before being able to produce such results from the experimental data, the first task in the analysis is the isolation of the studied reaction channel  $\gamma p \rightarrow \pi^0 p \gamma'$  from the background.

Another important part of this analysis contents the simulations of the studied channel, but also of the background channels, showing us the effect on a set of pure channel data.

Complete studied reaction:  $\gamma p \rightarrow \Delta^+ \rightarrow \Delta^+ \gamma' \rightarrow p \pi^0 \gamma' \rightarrow p \gamma \gamma \gamma'$

Symbol $i$	Particle
$\gamma$	beam photon
$\gamma_1, \gamma_2$	decay photons of the $\pi^0$
$\gamma'$	radiative photon
$p$	proton

Symbol	Variable
$\vec{V}_i = (\vec{X}_i, t_i)$	4-vector of the particle $i$
$\vec{X}_i$	position vector of the particle $i$ , of the 4-vector $\vec{V}_i$
$t_i, t(\vec{V})$	time of the particle $i$ , of the 4-vector $\vec{V}$
$E_i, E(\vec{V})$	energy of the particle $i$ , of the 4-vector $\vec{V}$
$\theta_i, \theta(\vec{V})$	polar angle of the particle $i$ , of the 4-vector $\vec{V}$
$\phi_i, \phi(\vec{V})$	azimuth angle of the particle $i$ , of the 4-vector $\vec{V}$
$m_i, m(\vec{V})$	mass of the particle $i$ , of the 4-vector $\vec{V}$
$InvM_i$	invariant mass of the particle $i$
$M_{ij}$	missing mass reconstructed from the particles $i, j$

Table 5.1: Nomenclature of the Reaction Products

## 5.1 Simulations

An essential part of the analysis concerns the reproduction of near to perfect reconstructed events, the *simulated events*. These events are first produced by a so called "generator", a Monte-Carlo program combined with theoretical kinematics knowledge. Then the generated events have to interact with a simulated setup via the so called "reconstruction program", in our case a GEANT<sup>1</sup> software reproducing as near as possible all the setup parts with the corresponding materials and dimensions.

Finally, the simulated events are analysed with the same code as the data, in order to also reproduce the analysis properties.

The so obtained simulated events are used for several goals. First they provide a very good reference for the channel identification, delivering examples as well of the analysed channel as of the background channels. Secondly and more generally, simulations are crucially needed for the extraction of cross sections. As we shall see in chapter 5.5, the *detector efficiency* has to be introduced in the cross section to correct the event loss due to a "never perfect" setup and analysis code. This detector efficiency is obtained by looking at the ratio of the simulated events *before* (just after being generated) and *after* having passed the detectors and the analysis code.

More about the efficiency will be discussed in chapter 5.5.

### 5.1.1 Event Generator

The event generator code is a Monte-Carlo program applying the kinematics properties corresponding to the chosen reaction. The goal of the generator is to reproduce as close as possible to the reality, events coming out of a reaction channel. In this work, we need simulated events for three different reaction channels:

- The MDM reaction channel:  $\gamma p \rightarrow \pi^0 p \gamma'$
- The single  $\pi^0$  background reaction channel:  $\gamma p \rightarrow \pi^0 p$
- The double  $\pi^0$  background reaction channel:  $\gamma p \rightarrow \pi^0 \pi^0 p$

---

<sup>1</sup>GEometry And Tracking

The development of the event generator used here was done by S.Schumann and M.Kotulla. A more detailed description can be found in [Schu07].

An important point by programming the Monte-Carlo is the *start distribution*. The latter concerns the space and energy distribution of the particles. In our case we have to consider two effects influencing this distribution:

1. The typical distribution of coherent bremsstrahlung photons (for spectra that integrate on large regions of incident range)
2. The typical distribution of scattered particles

Concerning 1) the energy distribution is a typical  $\frac{1}{E}$  bremsstrahlung, added with an artificial "step" in the coherence region (see figure 5.1):

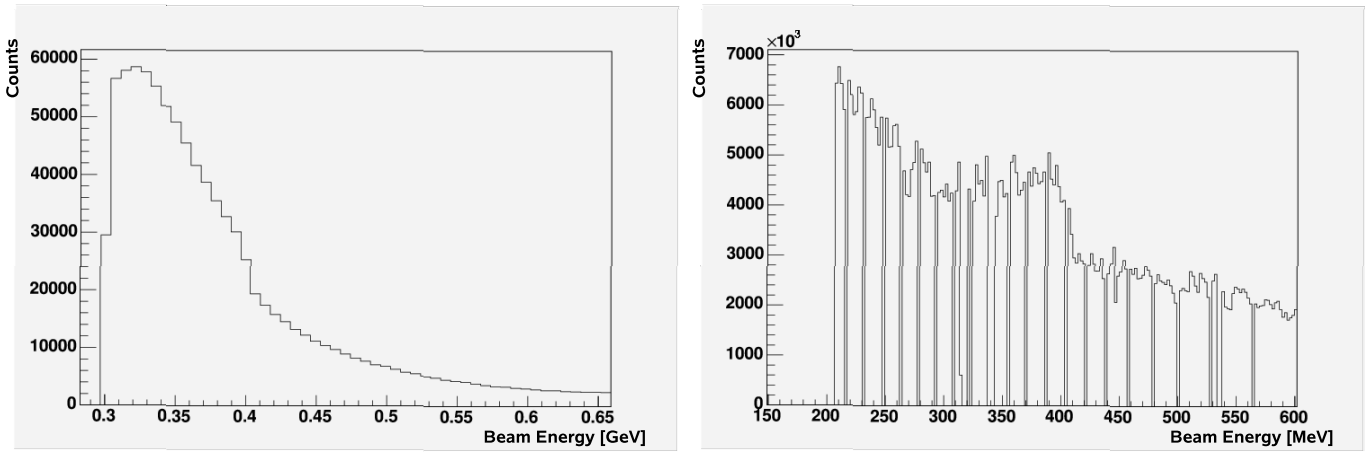


Figure 5.1: Comparison of the energy distribution between the generated (LEFT) and the real (RIGHT) bremsstrahlung photons.

The space distribution of the bremsstrahlung photons is isotropic in  $\phi$  and has a  $\theta$  distribution corresponding to the following function already seen in chapter 3.2.2:

$$\frac{d\sigma}{d\theta} \propto \frac{\theta}{(\theta^2 + \theta_c^2)} \quad (5.1)$$

with  $\theta_c = m_e/E_0$

The start distribution 2) of the scattered particles is chosen according to each reaction channel:

- $\gamma p \rightarrow \pi^0 p \gamma'$  : Here we have a three-body decay, i.e.  $3 \times 4 = 12$  degrees of freedom. Known parameters like masses and conservation laws can reduce this number to five and thus a five fold cross section is necessary for the complete description of the reaction kinematics.

This kind of cross section can be found in [Dre01]:

$$\frac{d^5\sigma}{dE'_\gamma d\Omega'_\gamma d\Omega^*_{\pi^0}} \quad (5.2)$$

where the \* corresponds to a variable in the  $p\pi^0$  rest frame, the others being in CM frame.

Numerical values of this cross section were delivered by M.Kotulla for 2 different possible values of  $\Delta$ 's magnetic moment:  $\mu_{\Delta^+} = 2$  and  $\mu_{\Delta^+} = 3$ .

The start energy and  $\theta$  distribution of the three reaction particles look like the following (photon incident energy = 400 MeV):

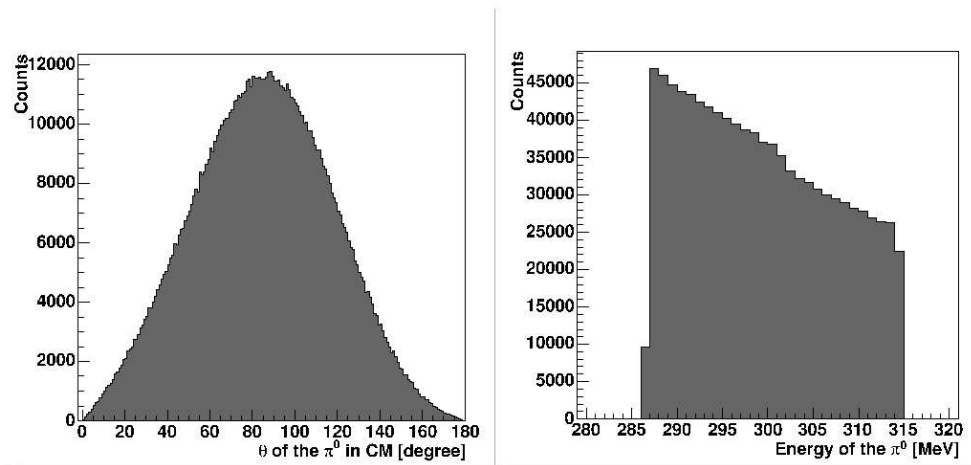


Figure 5.2: Start energy and  $\theta$  distribution (CM-frame) of the  $\pi^0$  in the reaction  $\gamma p \rightarrow \pi^0 p \gamma'$ .

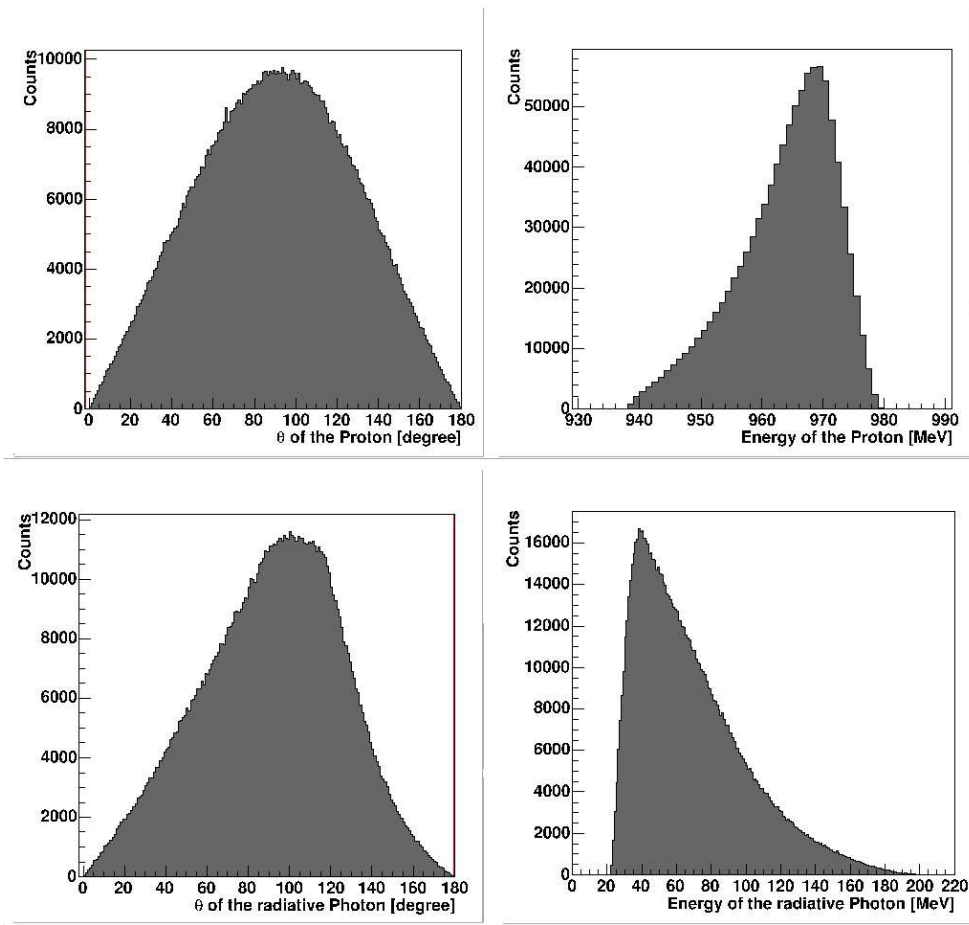


Figure 5.3: UP: Start energy and  $\theta$  distribution of the proton in the reaction  $\gamma p \rightarrow \pi^0 p \gamma'$  DOWN: Start energy and  $\theta$  distribution (CM-frame) of the  $\gamma'$  in the reaction  $\gamma p \rightarrow \pi^0 p \gamma'$

- $\gamma p \rightarrow \pi^0 p$ : The polar angle and energy distribution is based on the theoretical predictions of MAID [MAI03] and SAID [SAI06] for the unpolarized differential cross section in dependance of the photon energy  $E_\gamma$ :

$$\frac{d\sigma}{d\Omega_{\pi^0}} = \frac{1}{2\pi \sin \theta_{\pi^0}} \frac{d\sigma}{d\theta_{\pi^0}} \quad (5.3)$$

Again considering the azimuthal angle distribution  $\phi_{\pi^0}$  as isotropic, the kinematics of the  $\gamma p \rightarrow \pi^0 p$  reaction is with  $E_\gamma$  and  $\theta_{\pi^0}$  completely determined. The  $E_\gamma$  distribution is the upper described one for bremsstrahlung photons.

- $\gamma p \rightarrow \pi^0 \pi^0 p$  : Here we chose, like in M.Kotulla's work [Kot01], a phase space distribution. However, the photon beam energy dependance is specifically adapted by the use of the  $\gamma p \rightarrow \pi^0 \pi^0 p$  total cross section from [Kot01]. The latter cross section is combined with the standard bremsstrahlung energy dependance described before.

### 5.1.2 Detector Reconstruction

Our GEANT detector modeling is based on the previous existing crystal ball modeling developed by the Los Angeles group [Cla97]. As this modeling reproduced the crystal ball only, improvements have been performed to reach the nearest possible reproduction of our experimental setup.

S.Lugert and V.Kasevarov have been working on this project to implement the following experimental parts:

- The reproduction of TAPS in details with its aluminium frame, its "dummy"<sup>2</sup> crystals and the vetos material.
- The reconstruction of the TAPS Vetos and the corresponding scintillation properties.
- The addition of the PID delivering the expected energy traces.
- The addition of the wire chamber, however without its scintillation properties, thus not delivering any traces.
- A meticulous work on the crystal ball tunnel with implementation of metal inside tunnel frame and "disturbing" (i.e. source of rescattering) material around: screws, electric cables.

---

<sup>2</sup>some of the TAPS elements on the side are not real detector, but plastic modules used for the stability of the TAPS wall



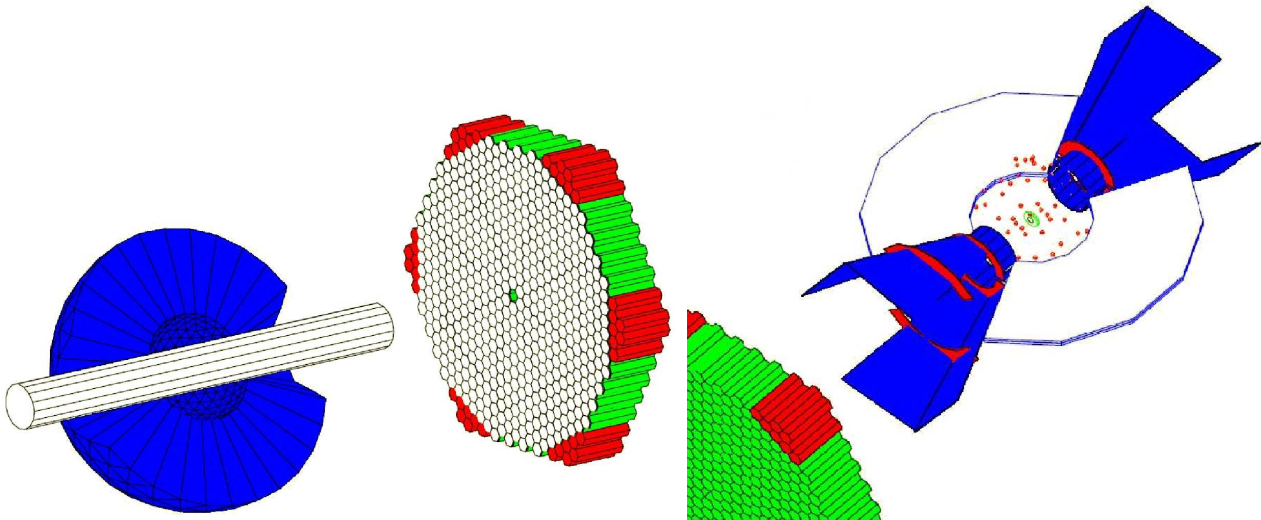


Figure 5.4: View of the reconstructed setup in GEANT. LEFT: The two main detectors CB and TAPS. RIGHT: The tunnel area inside the crystal ball.

### 5.1.3 Analysis of simulated Events

The most important goal of the simulations being the nearest reproduction of the data, the most important goal of the simulation *analysis* consists of running the most similar code as the one run on the data.

The detector reconstruction program delivers the simulated events in the form of a ROOT file which can be easily analysed with the standard AcquRoot code of the data. Thus, using the same analysis frame, we insure that simulated events are analysed in the same conditions as the data.

However a couple of unavoidable differences occur between the analysis code used for the experimental data and the one used for the analysis of the simulations:

- Due to the fact that simulated bremsstrahlung photons behave like an ideal bremsstrahlung process, only one photon corresponds to each incoming electron. There is no random event production, so no tagger random subtraction is done in the simulations.
- The times produced in the simulations are perfect Dirac peaks at 0, so the analysis part concerning the times of the different particles differs between the data and the simulations.
- As simulated events are registered without any hardware trigger condi-

tion, the latter has been replaced in the simulations by a software trigger developed by M.Unverzagt.

- The TAPS pulse shape property not being reproducible in simulations, the particle identification in TAPS is done for the simulations with a specific appropriate time of flight reference distribution and the vetos informations. In order to have a more similar analysis environment, the pulse shape consideration by the particle identification in TAPS for the data was finally switched off.
- The Time Of Flight cut has been adapted for simulation files.
- A proton energy correction based on simulated data has been produced.
- Some detector calibration files have been adapted to simulated events.

## 5.2 Channel Identification

This part of the analysis is extremely important and tricky, due to the fact that the studied reaction channel has a tiny cross section of 40 **nanobarns** and moreover has the two principal background channels:  $\gamma p \rightarrow \pi^0 p$  and  $\gamma p \rightarrow \pi^0 \pi^0 p$  with cross sections in the **microbarn** range. As shown further, additionally to the reaction background, we have to fight against the standard background like electromagnetic noise or random events.

### 5.2.1 The Data Reduction

A first data reduction was performed in order to reduce the amount of data that has to be treated along the whole MDM analysis.

The reduction method is a basic analysis code considering each event and making the decision to keep it further or throw it away. The accepted events are then stored in a ROOT Tree file which will be used for the standard MDM analysis.

The conditions for a good event in the data reduction code are the following:

- The event must contain exactly 4 clusters
- The sum of the masses of the cluster 4-vectors must be between 920 and 950 MeV (one proton and 3 photons)
- One of the reconstructed masses built with 2 clusters of the event must be between 100 and 160 MeV

The files after this data reduction procedure are 29x smaller than the raw data ones, this has a considerable effect on the analysis running time.

### 5.2.2 Basis Analysis Requirements and Cuts

The basic condition of the present channel analysis is a 4-cluster event, as the  $\pi^0$  is identified via its  $2\gamma$  decay products. Moreover, one of the cluster must have been identified as a proton and no cluster is allowed to be identified as a  $\pi^+$ .

Further, the best of the 3 different possible  $\gamma$  pairs is chosen as  $\pi^0$  via a  $\chi^2$  test on the  $\pi^0$  invariant mass. Thereafter, the basic cuts are applied on the incoming beam energy and the invariant mass of the  $\pi^0$ . The analysed energy range is

from 325 MeV to 475 MeV. The cut on the  $\pi^0$  mass is done from 110 MeV to 150 MeV (see fig. 5.5).

### Cut 1: $\pi^0$ Invariant Mass

$$\text{Inv}M_{\pi^0} = m(\vec{V}_{\gamma_1} + \vec{V}_{\gamma_2}) = m(\vec{V}_{\gamma_1\gamma_2}) \quad (5.4)$$

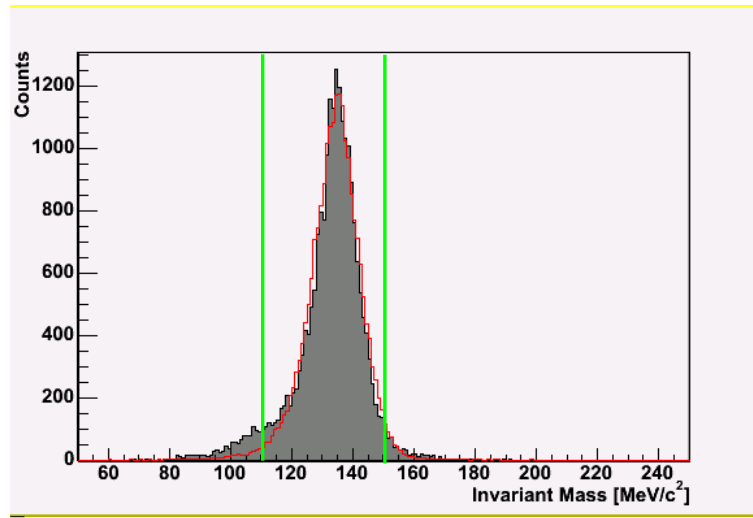


Figure 5.5: Invariant mass of the  $\pi^0$ : the grey distribution represents the data, the red shape shows a pure  $\gamma p \rightarrow \pi^0 p \gamma'$  simulation scaled to the data integral value, the green lines are the applied cuts.

### 5.2.3 The Substraction of the Tagger's Randoms

The Tagger randoms subtraction is an efficient method to remove the so-called *random events*. The latter are events resulting from the high multiplicity of the tagger and do not have any connection to the experiment reactions.

We usually find during the coincidence time window the electron corresponding to the photon which induced the reaction, but also some further electrons corresponding to photons that did not interact in the target. The way to isolate the electron and the tagged photon corresponding to our reaction is the *tagger random subtraction* and is done the following way:

We consider for each event the time difference between the  $\pi^0$  and the supposed beam photons delivered from the tagger multiplicity. We obtain the distribution shown in figure 5.6.

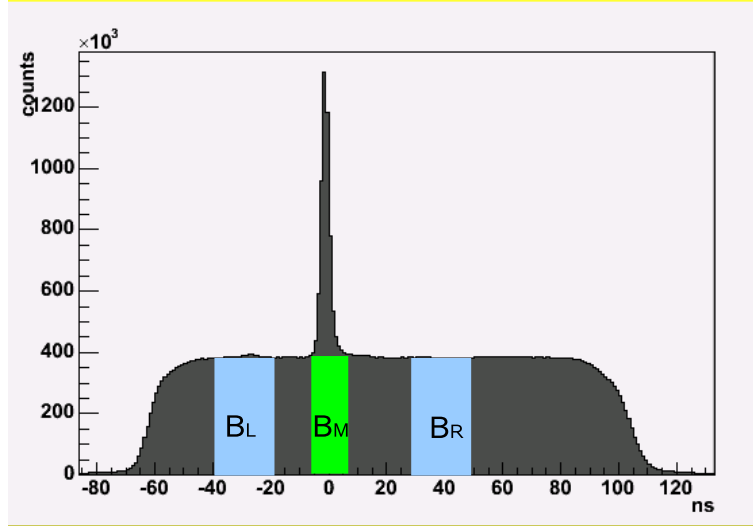


Figure 5.6: Technique for the substraction of the random events under the prompt peak:  $B_M = \frac{1}{4}(B_L + M_R)$

We clearly see the *prompt peak* or the peak of the *prompt events*, where the time of  $\pi^0$  rebuilt from 2 detected photons and the time of the scattered electron have a difference around 0 ( $\Rightarrow$  synchronisation). This is due to a spectra alignment of the difference time of the prompt  $e^-$  and  $\pi^0$  by 0. The tagger- $\pi^0$  time differences forming the large "carpet" come from the random events.

Cutting at the bases of the peak only removes a big part of the latter but it still remains the "carpet's" part lying under the prompt peak (Background Middle  $B_M$  on fig 5.6). This remaining background has the same shape as the background beside the peaks and thus its content can be estimated by the use of integral windows on the left and the right of the coincidence peak.

Practically we produce for each observable a histogram containing the events having  $t_{\pi^0\text{-tagger}}$  in the prompt peak's area  $A_{peak}$  (with width  $\sigma_{prompt}$ ) and a histogram containing events with a  $t_{\pi^0\text{-tagger}}$  in the left ( $B_L$ ) or right ( $B_R$ ) background area of  $2 \sigma_{prompt}$  - width (see fig. 5.6).

Finally we obtain the prompt area  $A_{prompt}$  as follows:

$$A_{prompt} = A_{peak} - B_M = A_{peak} - \frac{1}{4}(B_L + B_R) \quad (5.5)$$

We work with a broader background area (4x) in order to improve the statistics of the background subtraction.

### 5.2.4 Single $\pi^0$ Background Channel

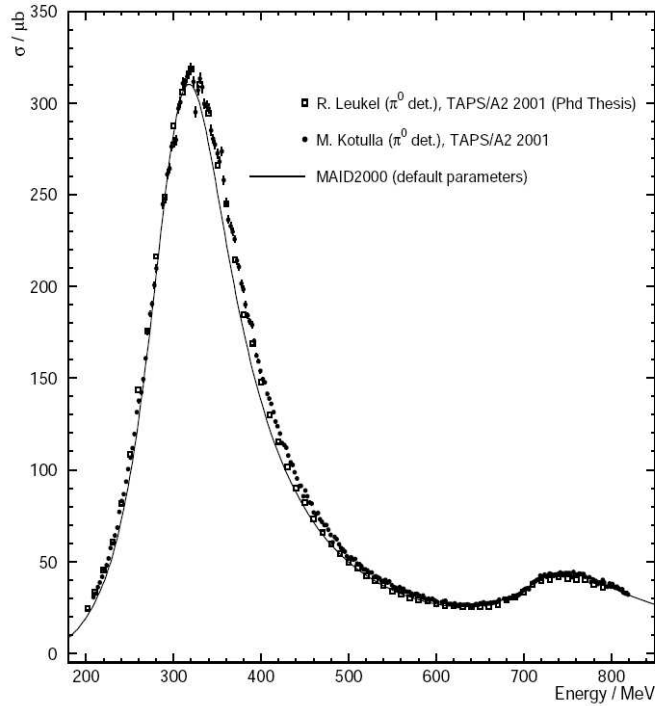


Figure 5.7: Total cross section of the  $\gamma p \rightarrow \pi^0 p$  channel. Taken from [Kot02]

The  $\gamma p \rightarrow \pi^0 p \rightarrow p\gamma\gamma$  channel can enter our analysis when one of the two of the following case happens:

- a) **Split-Offs:** here a "faked" additional photon produced by the electromagnetic shower in the crystals is detected together with the 3 final particles  $\gamma\gamma p$  of the single  $\pi^0$  channel. The *split-off effect* is due to the fact that high energetic photons interact with the scintillation material building  $e^+e^-$  pairs.

A photon or a lepton may escape the detector material and hit the detector again in a different section building finally a new electromagnetic shower.

- b) **Cluster Splitting:** it may also happen that not all EM showers of a real reaction event are completely collected in one cluster, but a part of the shower may be considered as part of a second cluster nearby the concerned cluster. This leads typically to the assumption of two photon hits instead of one.

In spite of the very efficient setup, the single  $\pi^0$  contribution remains highly disturbing, because of its high cross section (see fig. 5.7) in our beam energy region of interest (300-500 MeV).

Events coming from the single  $\pi^0$  reaction can be suppressed with the following cuts:

**Cut 2: The opening Angle between the Photon Pairs**

Split-off's photons have the property to be often detected in a crystal which is very close to the one of the photon that produced the EM shower. This is moreover always the case by cluster splitting. Due to this fact, the opening angle between the final photons provides a good view of the  $\gamma p \rightarrow \pi^0 p$  background channel contribution:

$$\begin{aligned} \text{Angle} &= \arccos(\vec{X}_{\gamma_1} \cdot \vec{X}_{\gamma_2}) \\ \text{or Angle} &= \arccos(\vec{X}_{\gamma_1} \cdot \vec{X}_{\gamma'}) \\ \text{or Angle} &= \arccos(\vec{X}_{\gamma_2} \cdot \vec{X}_{\gamma'}) \end{aligned} \tag{5.6}$$

(5.7)

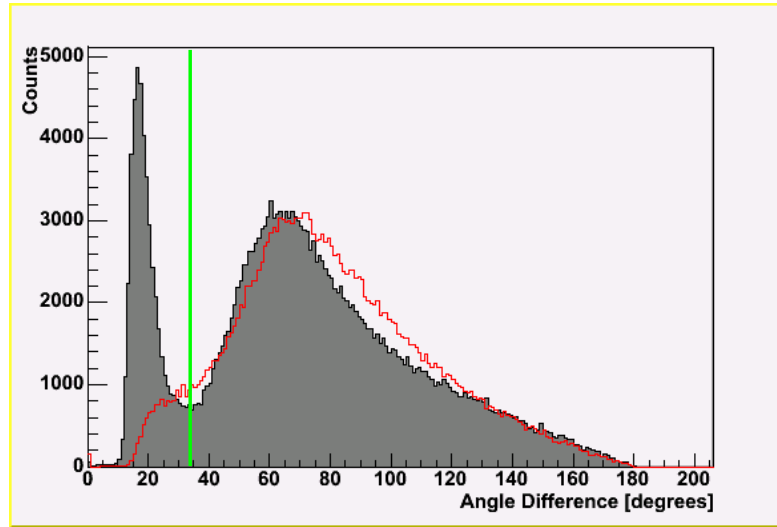


Figure 5.8: Opening Angle between the different photon pairs. We clearly identify the small angle area corresponding to the split-offs. The grey distribution represents the data, the red shape shows a pure  $\gamma p \rightarrow \pi^0 p \gamma'$  simulation scaled to the data integral value, the green line is the applied cut.

### Cut 3: The Time Difference between the Photon Pairs

As split-off photons are induced by the EM shower of one of the reaction photons, two possible cases can happen:

- They directly interact very close to the photon they are coming from. They appear in this case in the low opening angle region.
- They fly far away enough to not appear in the low opening angle region. They are in this case delayed in time and a first riddance can be reached by a cut on the time differences between the photons.

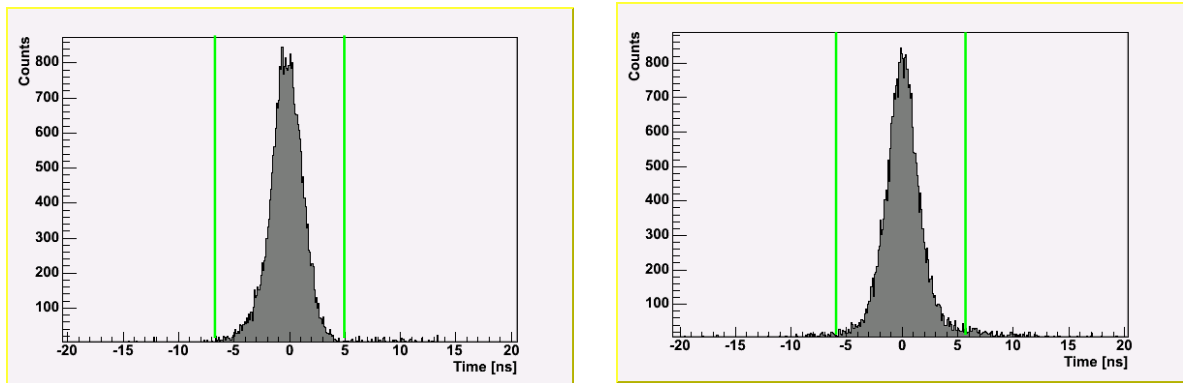


Figure 5.9: LEFT: Time difference between the reconstructed  $\pi^0$  and the  $\gamma'$ . RIGHT: Time difference between the 2 decay  $\pi^0$  photons.



Cut 4: The Missing Mass from The Proton

$$M_p = M(V_{beam}^{\vec{}} + V_{target}^{\vec{}} - \vec{V}_p) \quad (5.8)$$

The single  $\pi^0$  background can also be identified by building the missing mass from the proton. In the case of a  $\gamma p \rightarrow \pi^0 p \gamma'$  reaction this missing mass results from a combined four vector of **two** "missing" particles, the  $\pi^0$  and  $\gamma'$ . It thus shows a broad distribution. In the case of a  $\gamma p \rightarrow \pi^0 p$  reaction, the missing mass corresponds to the mass of only **one**  $\pi^0$ , building a peak around 135 MeV. This peak can be perceived on figure 5.10. Accepting only events with  $M_p > 145$  MeV suppresses this single  $\pi^0$  participation. (The second cut at 310 MeV is related to the suppression of the double  $\pi^0$  channel, see below).

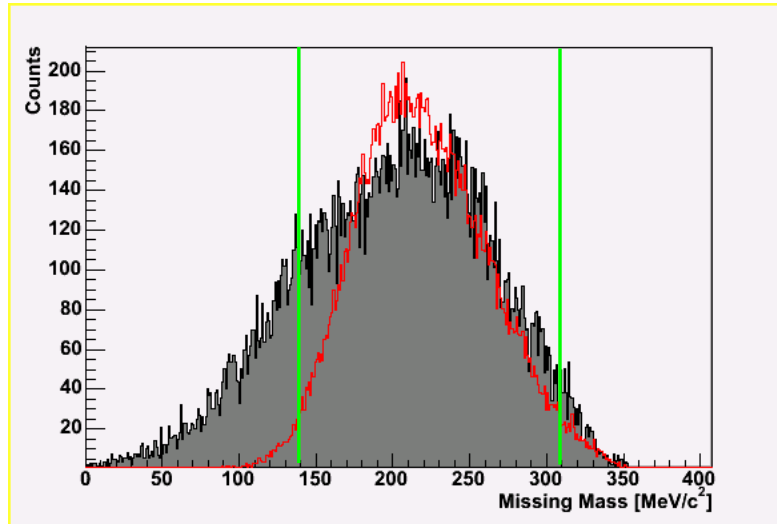


Figure 5.10: Missing mass reconstructed from the proton. The grey distribution represents the data, the red shape shows a pure  $\gamma p \rightarrow \pi^0 p \gamma'$  simulation scaled to the data integral value between the cuts, the green lines show the applied cuts.

Cut 5: The Energy of the Radiative Photon

The split-offs effect deliver a large amount of low energetic photons. This contribution can be clearly identified by comparing the  $E_{\gamma'}^{CM}$  data spectrum with the pure  $\gamma p \rightarrow \pi^0 p \gamma'$  simulation:

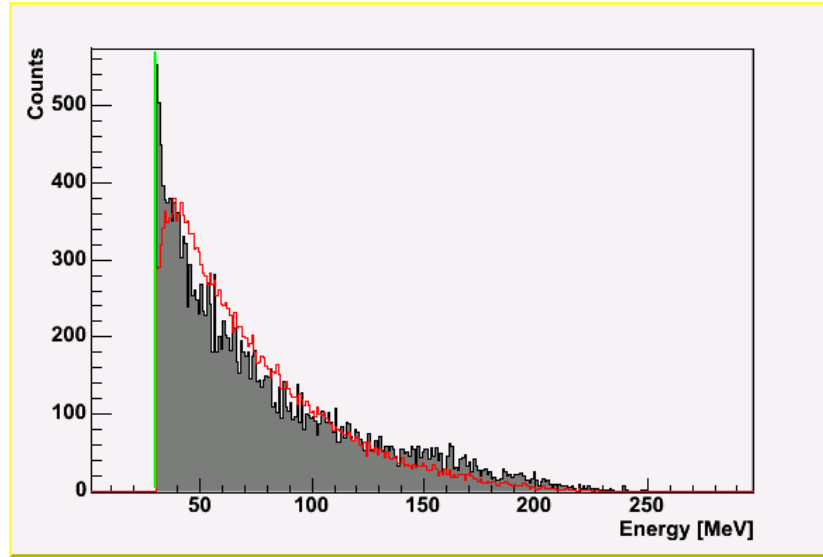


Figure 5.11:  $E_{\gamma}^{CM}$ : The single  $\pi^0$  channel. The applied cut is shown with the green line at  $E_{\gamma}^{CM} = 30$  MeV.

### 5.2.5 Double $\pi^0$ Background Channel

Here also, there is a "real" and a "cluster" situation which lead to the emergence of  $\gamma p \rightarrow \pi^0 \pi^0 p$  events in our analysis. The clean detection of this channel delivers a final five particles status, 4  $\gamma$ s coming from the  $2\pi^0$  and one proton.

- a) **Photon Loss:** the typical case of mis-identifying this reaction with ours is the loss of one of the 4 photons somewhere on the way. Notice that this effect is, with the actual setup of almost  $4\pi$  steradians minimized, but again, due to the high cross section of this channel (see fig. 4.3), we have to treat this contamination. These described events are easily removed with the *missing mass'* or *energy balance's* cuts, as the energy of the lost photon gets also lost.
- b) **Cluster Fusion:** here we have the inverse problem of the single  $\pi^0$  channel's one. It may also happen that clusters corresponding to two photons are identified as a single cluster by the algorithm. There is no efficient cut against this kind of contamination, this being the main reason why a

double  $\pi^0$  channel subtraction is performed for the final results, in order to get rid of a remaining contamination by this channel.

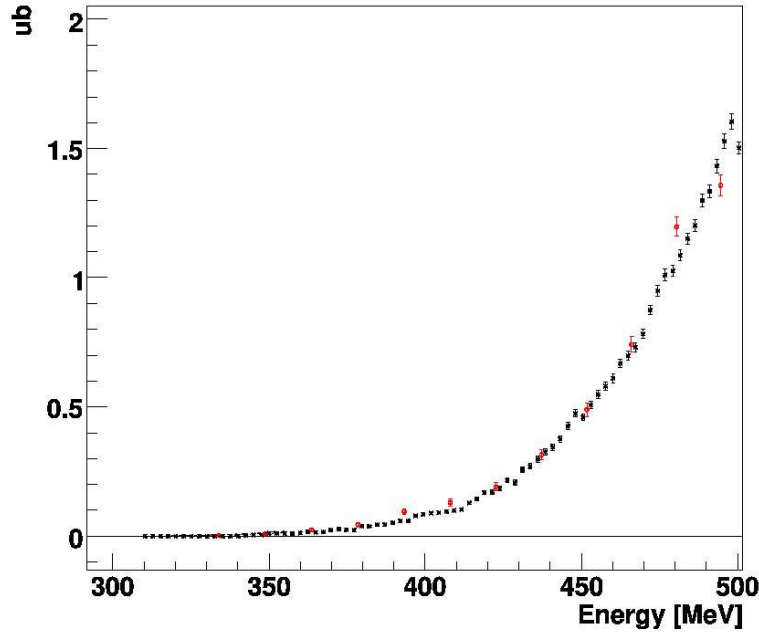


Figure 5.12: Total cross section of the  $\gamma p \rightarrow \pi^0 \pi^0 p$  channel in our beam energy region of interest: 300-500 MeV. From [Zeh08]

The removal of the double  $\pi^0$  contribution can be done with the help of the following cuts: the proton missing mass cut, as shown in the last part. Further, the most important cut concerning this background channel is applied on the missing mass built from the proton and the pion:

#### Cut 6: The Missing Mass from The Proton and The $\pi^0$

$$M_{\pi^0 p} = M(V_{beam}^{\vec{}} + V_{target}^{\vec{}} - V_{\pi^0}^{\vec{}} - V_p^{\vec{}}) \quad (5.9)$$

We should see here the mass corresponding to the radiative photon, i.e. a peak at 0. We study this variable for three different energy ranges to be able to see the effect of the double  $\pi^0$  contribution which becomes important for

$E_\gamma \approx 450$  MeV (see fig.5.12).

Looking at figures 5.13, 5.14, we notice the background growing with the beam energy. This  $\gamma p \rightarrow \pi^0 \pi^0 p$  background should deliver a peak at the double  $\pi^0$  squared mass (fig. 5.13, RIGHT), this effect is slightly distinguishable on the data with a growing background on the right side of the peak (fig.5.13, LEFT). However, as it appears clearly by the double  $\pi^0$  simulated data, this  $\gamma p \rightarrow \pi^0 \pi^0 p$  often delivers a  $M_{\pi^0 p}$  peak at 0, i.e it often happens that one of the four final photons are identified in the same cluster as another one. This explains the fact that the  $\gamma p \rightarrow \pi^0 \pi^0 p$  background does not appear clearly on the data, as a part remains hidden in the around 0 peak.

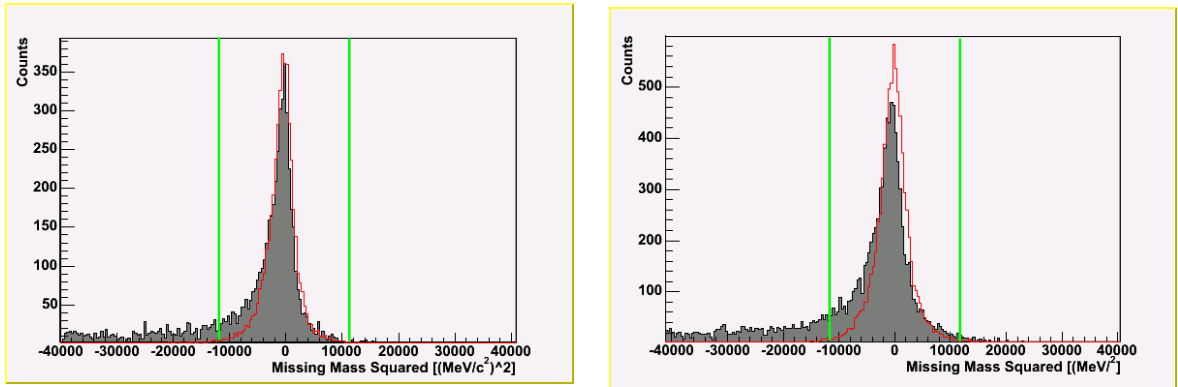


Figure 5.13:  $M_{\pi^0 p}$  for an incoming beam energy of 325-375 MeV (left) and 375-425 MeV (right). The red shape shows pure  $\gamma p \rightarrow \pi^0 p \gamma'$  simulation scaled to the data integral value, the green lines show the applied cuts.

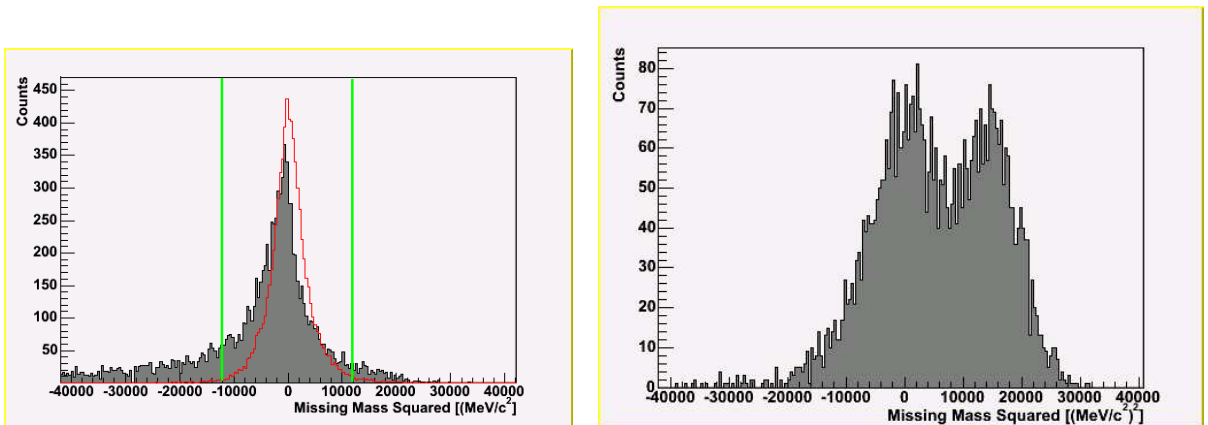


Figure 5.14: Comparison Missing Mass C Data/double  $\pi^0$  simulations  $M_{\pi^0 p}$  for incoming beam energy of 425-475 MeV. LEFT: data, the red shape shows a pure  $\gamma p \rightarrow \pi^0 p \gamma'$  simulation scaled to the data integral value, the green lines show the applied cuts. RIGHT: Simulated  $\gamma p \rightarrow \pi^0 \pi^0 p$  data.

Another cut removing the double  $\pi^0$  channel is the one on the missing mass built from the pion and the radiative photon:

Cut 7: The Missing Mass from the  $\pi^0$  and the  $\gamma'$

$$M_{\pi^0\gamma'} = M(V_{beam}^{\vec{}} + V_{target}^{\vec{}} - V_{\pi^0}^{\vec{}} - V_{\gamma'}^{\vec{}}) \quad (5.10)$$

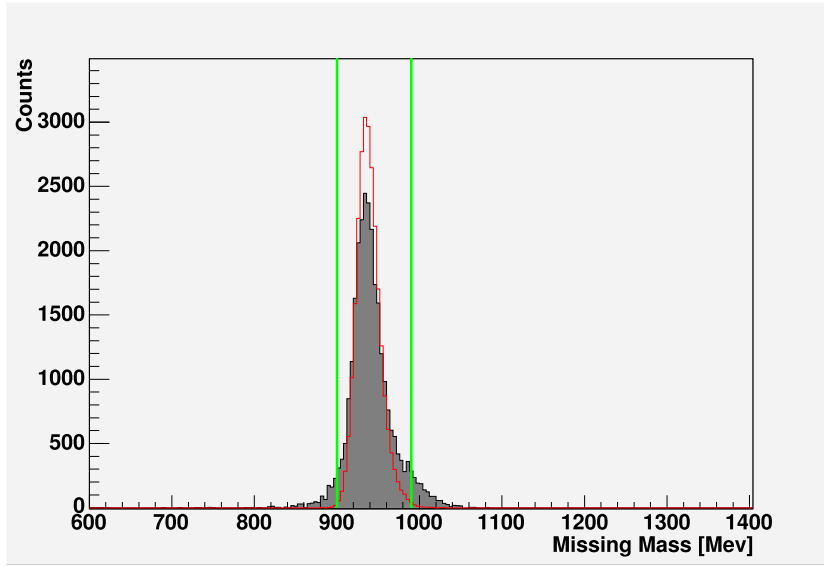


Figure 5.15:  $MM_{\pi^0\gamma'}$ : Our  $\gamma p \rightarrow \pi^0 p \gamma'$  channel delivers a peak at the proton's mass. The  $\gamma p \rightarrow \pi^0 \pi^0 p$  channel contains an additional  $\pi^0$  mass and thus brings a background contribution above 1000 MeV. The red shape shows a pure  $\gamma p \rightarrow \pi^0 p \gamma'$  simulation scaled to the data integral value, the green lines show the applied cuts.

The last cut contributing to the removal of the double, but as well as the single  $\pi^0$  channel, concerns the so called *energy balance* EB:

Cut 8: The Energy Balance

$$EB = E(V_{beam}^{\vec{}} + V_{target}^{\vec{}} - V_{\pi^0}^{\vec{}} - V_{\gamma'}^{\vec{}} - \vec{V}_p) \quad (5.11)$$

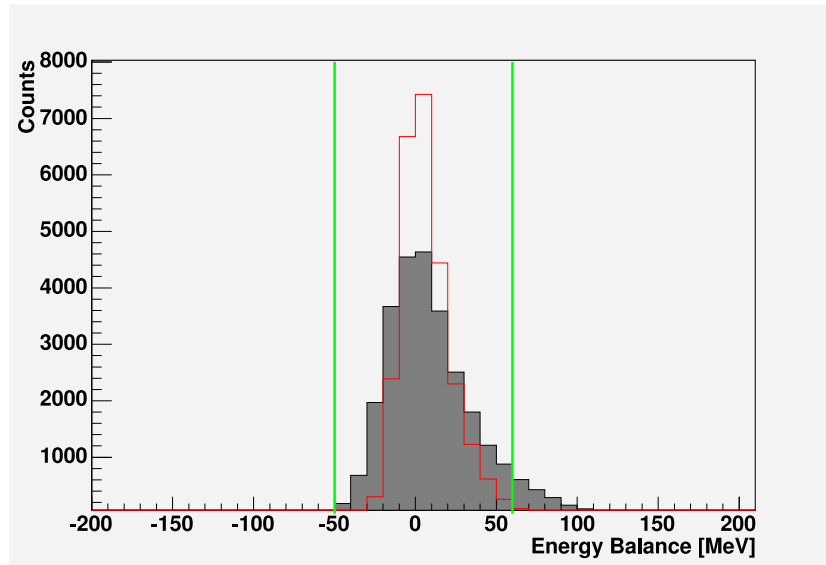


Figure 5.16: Energy Balance: The double as well as the single  $\pi^0$  channel deliver a peak above 0 MeV. The red shape shows pure  $\gamma p \rightarrow \pi^0 p \gamma'$  simulation scaled to the data integral value above the cut, the green lines show the applied cuts.

## 5.2.6 The Electromagnetic Background

A large amount of electromagnetic background appears along the beam line. It is mainly due to the *beam dump*<sup>3</sup>, but also to the interaction of the photon beam with the target material and other detector's material on the way to TAPS. The latter background is extremely visible on the polar angle distribution of the radiative photon (see fig. 5.17, LEFT). In order to get rid of this very disturbing electromagnetic noise, a cut is applied on  $\theta_{\gamma'}^{CM}$ :

<sup>3</sup>Remaining part of the photon beam which did not interact in the target

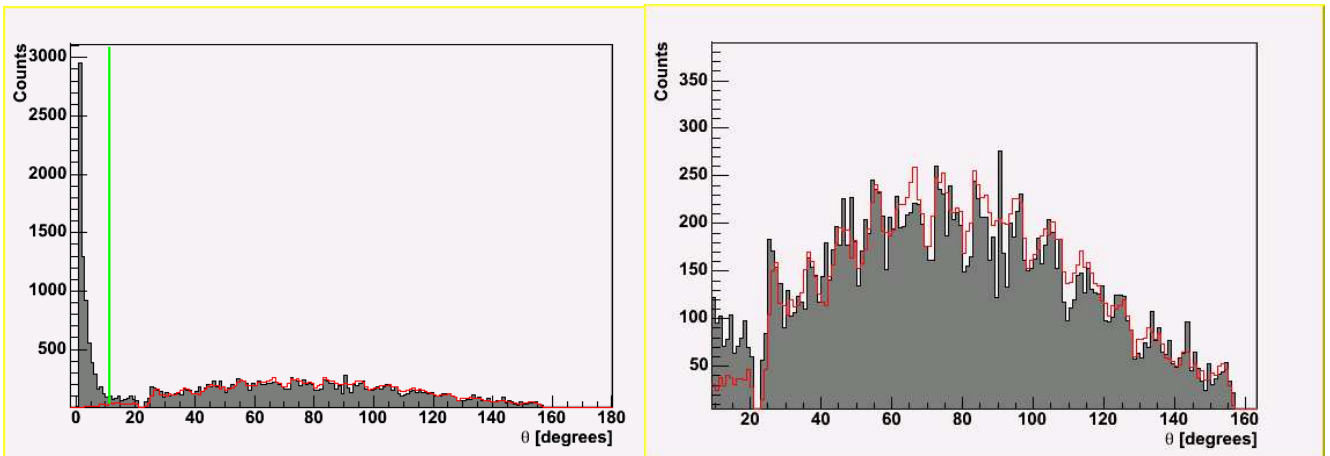


Figure 5.17:  $\theta_{\gamma'}^{CM}$  LEFT: Before the cut, the EM background among 30 degrees is dominant. RIGHT: Same and distribution after the cut: the data shape becomes similar to the simulated data. (The red shape shows a pure  $\gamma p \rightarrow \pi^0 p \gamma'$  simulation scaled to the data integral value above the cut, the green lines show the applied cut.)

### 5.2.7 The Setup Background

Finally, an additional background derives from the fact that much setup material (PMTs, PID electronic modules, etc.) is placed very close to the target. This is visible in the proton angular distribution:

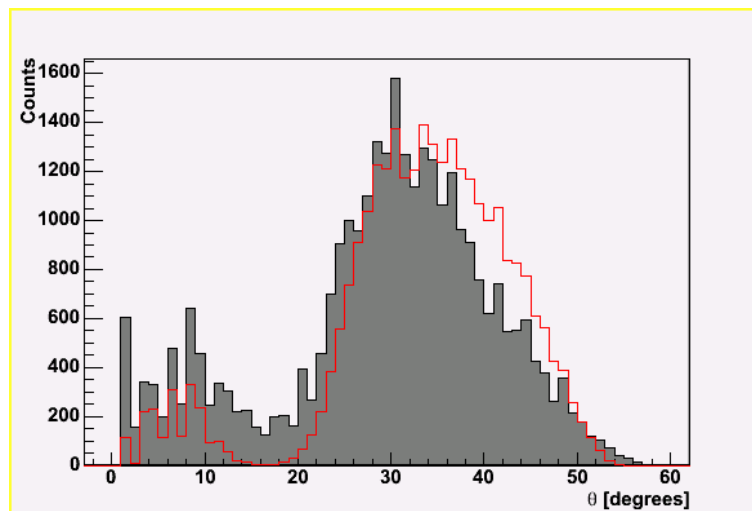


Figure 5.18:  $\theta_p$ : We clearly see the background events due to material scattering between 10 and 20 degrees. The red shape shows a pure  $\gamma p \rightarrow \pi^0 p \gamma'$  simulation scaled to the data integral value, the green lines show the applied cuts.

### 5.2.8 Overview of the Cut Effects

In the following pictures we can observe the effects of the cuts on the different channels. The shown variable is the missing mass calculated from the  $\pi^0$  and the  $\gamma'$ :

$$M_{\pi^0\gamma'} = M(V_{beam}^{\vec{}} + V_{target}^{\vec{}} - V_{\pi^0}^{\vec{}} - V_{\gamma'}^{\vec{}}) \quad (5.12)$$

The first column shows the evolution of the experimental data, the second shows the simulated  $\gamma p \rightarrow \pi^0 p \gamma'$  events, the ones we want to keep. The third and the fourth column show the evolution of simulated events from the  $\gamma p \rightarrow \pi^0 p$  and  $\gamma p \rightarrow \pi^0 \pi^0 p$  channels, the ones we want to remove.

Each row shows the plots after the application of one new cut:

- 1) Condition applied on the photon beam energy: 325-475 MeV and cut on the azimuthal angle of the radiative photons (see EM background)
- 2) Additional cut on the missing mass calculated from the proton (Cut 4)
- 3) Additional cut on the energy of the radiative photon (Cut 5)
- 4) Additional cut on azimuthal angle of the proton (see setup background)
- 5) Additional cut on the invariant mass of the  $\pi^0$  (Cut 1)
- 6) Additional cut on the energy balance (Cut 8)
- 7) Additional cut on the opening angle between the photons (Cut 2)
- 8) Additional cut on the missing mass calculated from the  $\pi^0$  and the proton (Cut 6)
- 9) Additional cut on the times between the  $\pi^0$  photons (Cut 3)
- 10) Additional cut on the times between one of the  $\pi^0$  photons and the  $\gamma'$  (Cut 3)

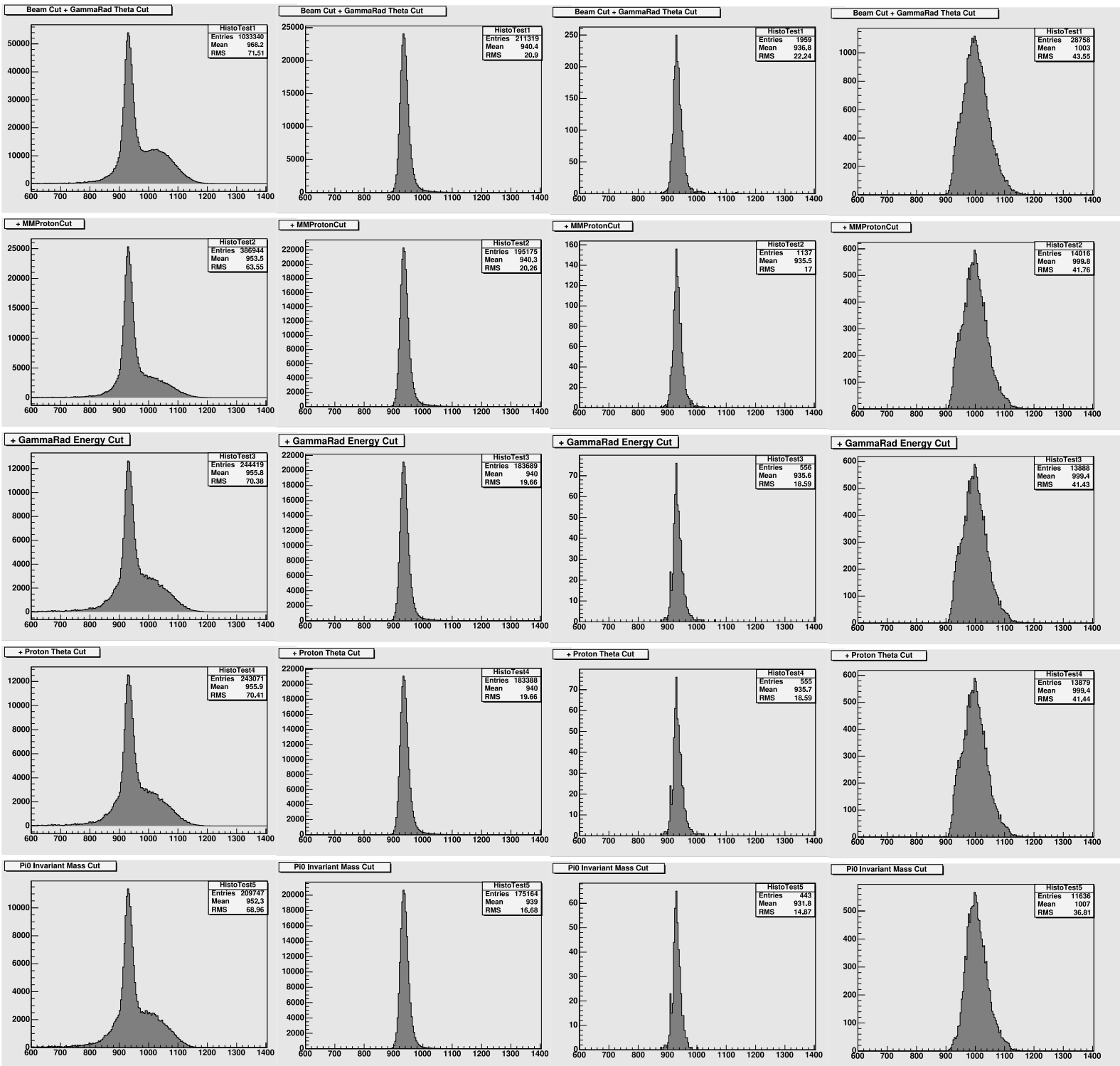


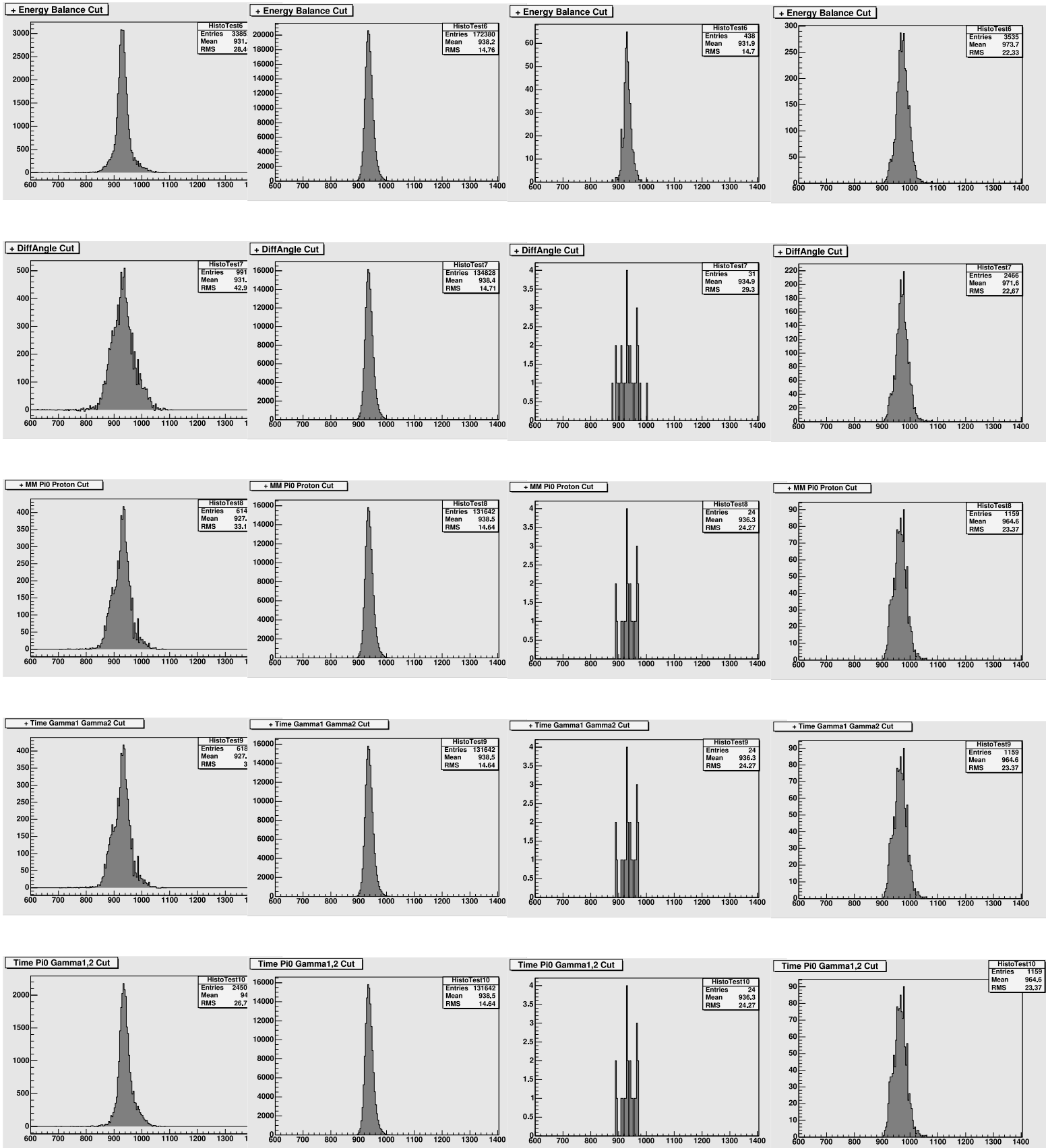
Real data

Simul  $p\pi^0\gamma$

Simul  $p\pi^0$

Simul  $p\pi^0\pi^0$



Real dataSimul  $p\pi^0\gamma$ Simul  $p\pi^0$ Simul  $p\pi^0\pi^0$ 

Final view of the missing mass calculated from the  $\pi^0$  and the  $\gamma'$ :

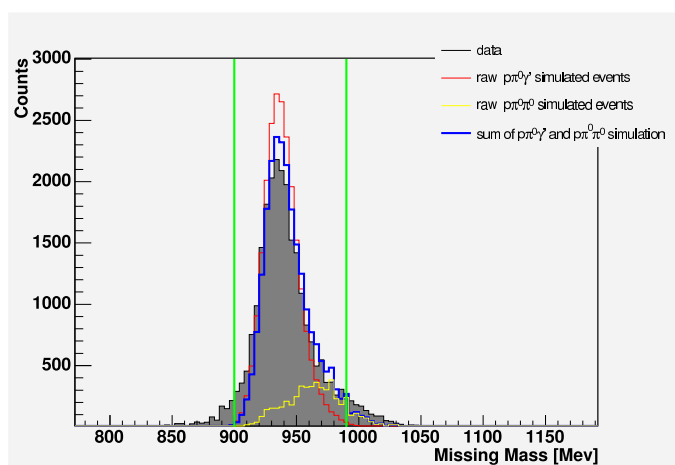


Figure 5.19: Final missing mass calculated from the  $\pi^0$  and the  $\gamma'$ . The  $\gamma p \rightarrow \pi^0 p \gamma'$  simulation has been scaled to the data integral between the cuts. The remaining  $\gamma p \rightarrow \pi^0 \pi^0 p$  background has been scaled considering the total cross section of this channel and the number of generated events in our beam energy range: 325-475 MeV. The latter remaining background is finally extracted with the method described in chapter 5.5.2

### 5.3 Analysis of the single $\pi^0$ Channel

A complementary analysis of the  $\gamma p \rightarrow \pi^0 p$  channel is important as cross check for the MDM analysis and is needed for the application of the theoretical models for the determination of the magnetic moment.

The single  $\pi^0$  channel is a very well known and defined channel due to its high cross section.

This analysis is based on the following steps:

- The events must contain *at least* 2 clusters.
- The events must contain *exactly* 2 photons.
- The 2 photons composing the  $\pi^0$  must have an azimuthal angle over 20 degrees. We thus avoid the large electromagnetic background in forward direction.

- A mass is reconstructed with all the possible cluster pairs. With a  $\chi^2$  test the pair having the nearest mass to the  $\pi^0$  ones is kept to be the  $\pi^0$ .
- The tagger random subtraction is done similarly as for the MDM analysis.
- A cut on the  $\pi^0$  invariant mass is applied between 115 and 155 MeV (see figure 5.20, LEFT).
- A cut on the  $\pi^0$  missing mass 860 and 990 MeV (see figure 5.20, RIGHT).

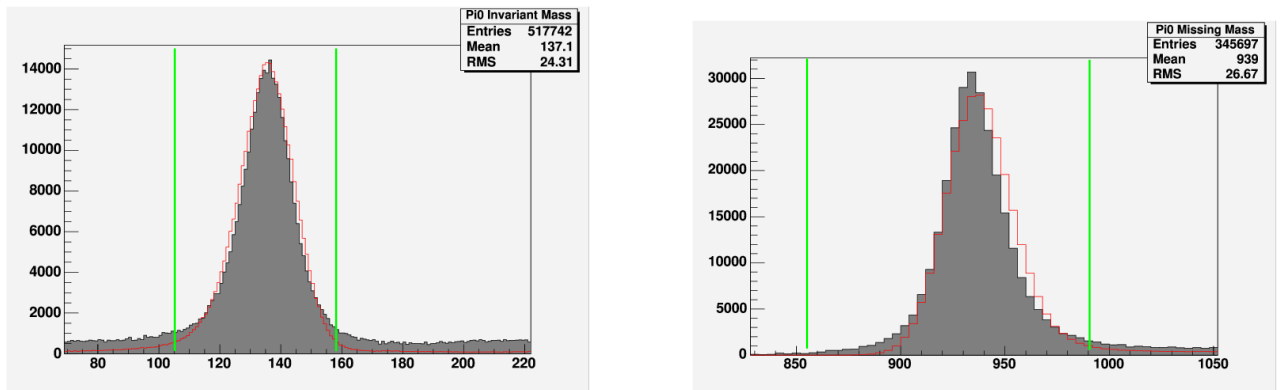


Figure 5.20: Cuts applied in the single  $\pi^0$  analysis. LEFT: Invariant mass of the  $\pi^0$ . RIGHT: Missing mass of the  $\pi^0$ :  $MM_{\pi^0} = M(\vec{V}_{beam} + \vec{V}_{target} - \vec{V}_{\pi^0})$

Another important thing that has to be considered is the trigger. The hardware trigger applied to the data during the MDM measurements was mainly  $M \geq 3$  with one  $M=2$  event accepted out of 49. This means that by using MDM data with the single  $\pi^0$  analysis, we must only treat these  $M=2$  events and finally multiply the cross sections by a factor 49.

The trigger hardware information is stored in the ADC in the form of an 8-bit number and delivers for each event the status of the corresponding trigger. In the present single  $\pi^0$  analysis, only events having the trigger status  $M2$  only are accepted.

Of course, also the "hardware trigger" applied in the simulations (see chapter 5.1.3) must be changed from  $M=3$  to  $M=2$ .

We see here the  $\theta$  angle of the  $\pi^0$  in CM, a comparison between simulations and data. This distribution is the base of the extracted angular differential cross section:

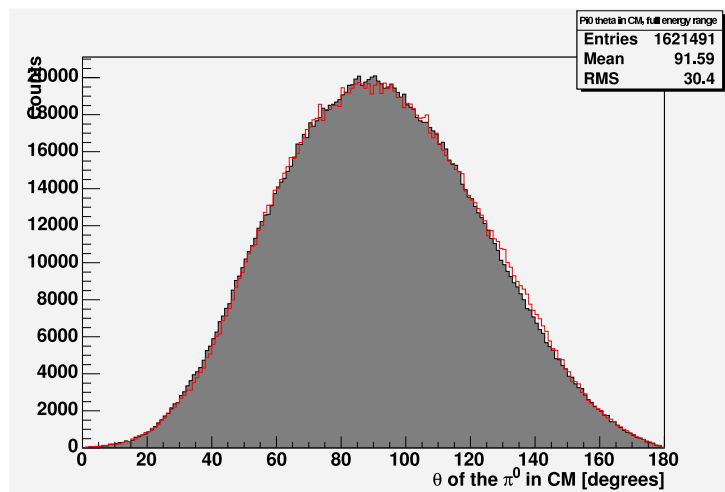


Figure 5.21:  $\theta$  angle of the  $\pi^0$  in CM by the single  $p i^0$  analysis. The red shape shows a pure  $\gamma p \rightarrow \pi^0 p$  simulation scaled to the data integral value.

## 5.4 Extraction of Polarisation Variables:

### *The Circular Asymmetry*

Considering the sensitivity of the circular asymmetry to the magnetic moment in the theoretical determinations and the opportunity of having circularly polarized photons, we also determine this asymmetry. A special beamtime setup in January 2004 was also adapted with lower electron beam energy of 570 MeV.

The kinematics of a decay in three <sup>4</sup> particles like we have in the  $\gamma p \rightarrow \pi^0 p \gamma'$  channel allow the definition of two planes in the reaction and thus provide the possibility to build an asymmetry on the opening angle between these 2 planes [see fig. 5.23].

The circular asymmetry can be simply determined using the following formula:

$$A^{circ} = \frac{1}{P_\gamma} \cdot \frac{N_\gamma^{left} - N_\gamma^{right}}{N_\gamma^{left} + N_\gamma^{right}} \quad (5.13)$$

Where the helicity transfer  $T_h$  is determined for each event via:

$$T_h = \frac{E_\gamma(E_{e^-} + \frac{1}{3}(E_{e^-} - E_\gamma))}{E_{e^-}^2 + (E_{e^-} - E_\gamma)^2 - \frac{2}{3}E_{e^-}(E_{e^-} - E_\gamma)} \quad (5.14)$$

With  $P_e$  the degree of polarisation of the electron beam, we obtain:

$$P_\gamma^{circ} = P_e \cdot T_h \quad (5.15)$$

The difference in the photon flux between photons with *right* and photons with *left* circular polarisation has been studied by Dirk Krambrich. He determined a tiny value of  $\frac{N_\gamma^{left}}{N_\gamma^{right}} \approx 1.00055$ , which has been neglected here.

This way to describe the asymmetry, i.e on an angle  $\phi$ , as well as the notation, derives from the one of L. Roca [Roc05] applied reaction channels with two pions. We can adapt his description to our channel by simply replacing one of the pions by the radiative photon.

The derivation of the circular asymmetry value is reached with the following steps and using the following parameters:

Roca's angle definition becomes in our case:

---

<sup>4</sup>before the  $\pi^0$  decay

#### 5.4. EXTRACTION OF POLARISATION VARIABLES: THE CIRCULAR ASYMMETRY 125

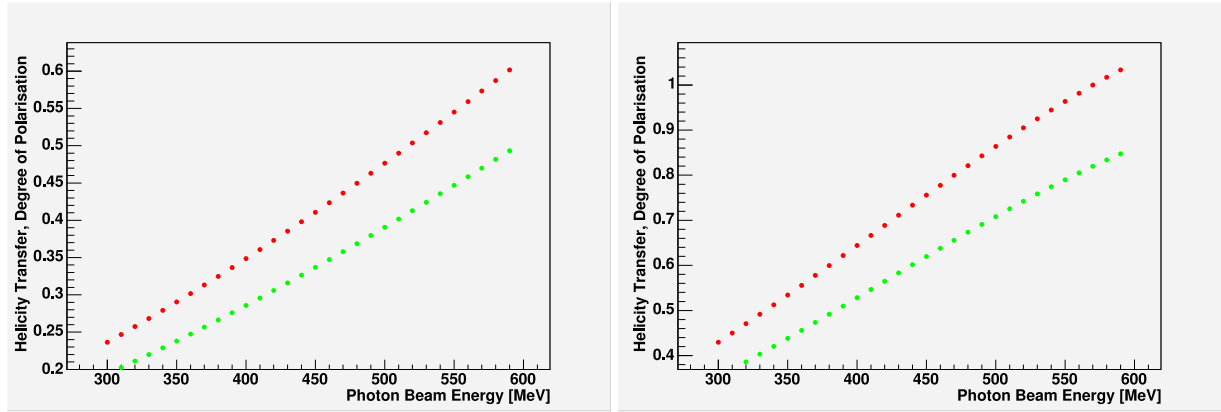


Figure 5.22: Helicity Transfer  $T_h$  (red) and degree of polarisation  $P_\gamma^{circ} = P_e \cdot T_h$  (green) for the 2 electron beam energies used: LEFT: 883.25 MeV, RIGHT: 570.19 MeV

$$\begin{aligned} \cos \phi &= \frac{(\vec{k} \times \vec{q}) \cdot (\vec{q} \times \vec{p}_{\pi^0})}{|\vec{k} \times \vec{q}| |\vec{q} \times \vec{p}_{\pi^0}|} \\ \sin \phi &= -\frac{((\vec{k} \times \vec{q}) \times \vec{q}) \cdot (\vec{q} \times \vec{p}_{\pi^0})}{|(\vec{k} \times \vec{q}) \times \vec{q}| |\vec{q} \times \vec{p}_{\pi^0}|} \end{aligned} \quad (5.16)$$

with  $\vec{q} \equiv \vec{p}_{\pi^0} + \vec{p}_{\gamma'}$ , and with all the momenta in the overall center of mass frame.

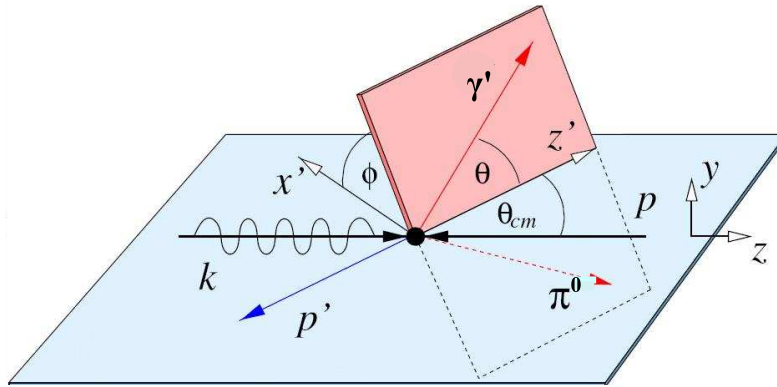


Figure 5.23: Definition of the angle  $\phi$ , on which the circular asymmetry is built.  $\phi$  corresponds to the opening angle between 2 reaction planes. One plane is defined by the beam and the outgoing proton, another plane is defined by the outgoing pion and the radiative photon.

## 5.5 Extractions of Cross Sections

### 5.5.1 The Components of the Cross Sections

The important cross sections of this work are two differential cross sections based on the kinematics of the radiative photon, the latter being the key to the  $\Delta$  magnetic moment. The first differential cross section is built on  $\theta_{\gamma'}$ , the second on  $E_{\gamma'}$ , both variables being considered in the CM frame.

For the single  $\pi^0$  analysis only the differential cross section for the  $\theta_{\pi^0}$  is needed, as this one provides a reliable feedback of the all  $\gamma p \rightarrow \pi^0 p$  analysis and is essential for the determination of the  $\mathbf{R}$  distribution (see chapter 6.2.2).

Cross sections given in an area unit basically describe the surface that would have the target if each photon reaching a target proton would induce the studied reaction. They are roughly obtained by dividing the statistics of the wanted variable by the number of protons present in the target and the number of disposable photons.

Looking more in detail, the extraction of cross section requires several additional steps in comparison to asymmetries. All the needed parameters are summarized in the following cross section formula:

$$\sigma = \frac{N_{events}}{N_{e^-} \cdot \eta_{tagg} \cdot \epsilon_{CBTAPS} \cdot \Lambda_{\pi^0 \rightarrow \gamma\gamma} \cdot \rho_t} \quad (5.17)$$

- The number of events  $N_{events}$  corresponds to the statistics of the wanted variable at the end of the analysis.
- $N_{e^-}$  is delivered by the scalers, registering the recoil electrons in the tagger.
- The tagging efficiency  $\eta_{tagg}$  is obtained via the procedure described in chapter 3.2.3.
- The branching ratio  $\Lambda_{\pi^0 \rightarrow \gamma\gamma}$  of the pion decay in 2 photons is a value of 0.998
- The target area density, i.e the number of scattering centers (protons) for a given area:



$$\begin{aligned}
\rho_t &= \frac{2\rho(LH_2)N_A \cdot L}{M_{mol}(LH_2)} & (5.18) \\
&= \frac{2 \cdot 0.0708g/cm^3 \cdot 6.022 \cdot 10^{23}/mol \cdot 4.76cm}{2.01588g/mol} \cdot \frac{1}{10^{24}barn/cm} \cdot \frac{1}{10^9nb/barn} \\
&= 2.013475 \cdot 10^{-10}/nb
\end{aligned}$$

- The experiment efficiency  $\epsilon_{CBTAPS}$  is obtained by using simulated data. The latter efficiency consists of the ratio of the distribution of raw generated events and the same distribution after having passed through the simulated detectors and having been analysed with the analysis code described in chapter 5.1.3. In the present work, the needed efficiencies are the one on the azimuthal distribution  $\theta_\gamma$  of the radiative photon and its energy distribution. We see here an example for this efficiency :

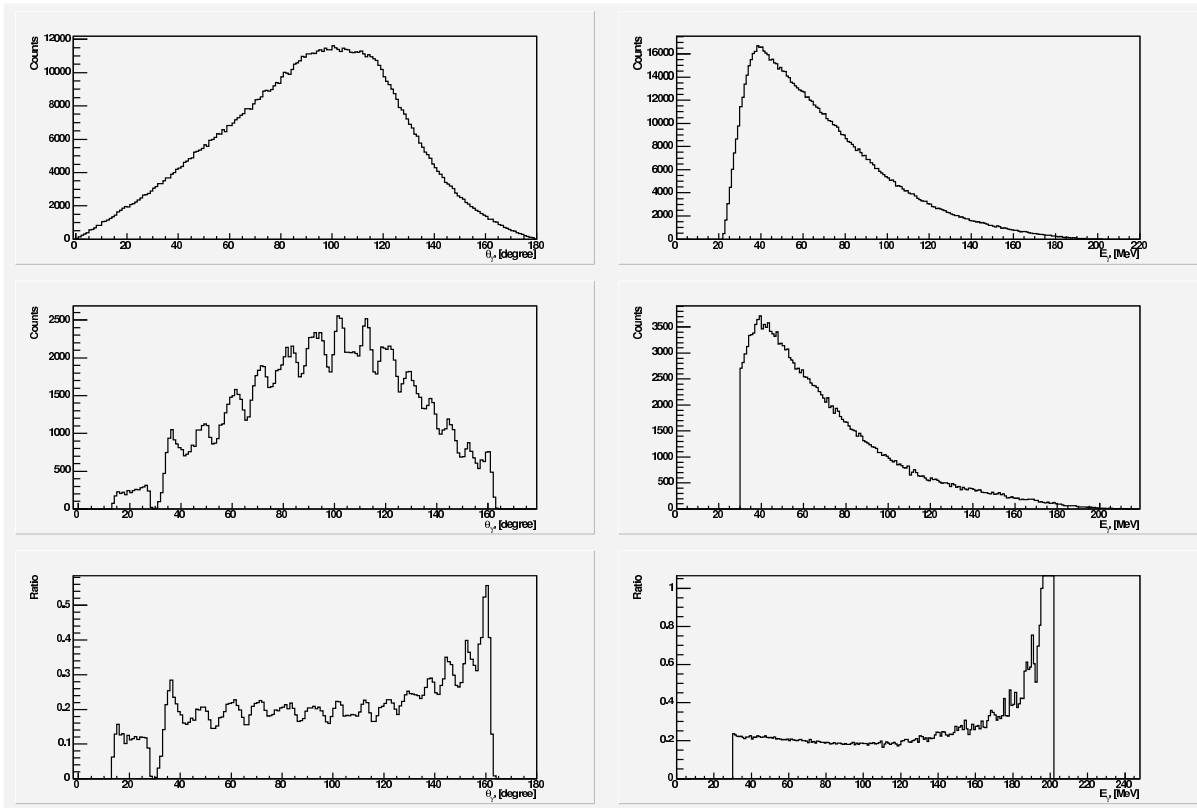


Figure 5.24: Example of detector efficiencies. The left column concerns the  $\theta_\gamma$ , the right column concerns the  $E_\gamma$ . The distributions on the top are the start distribution delivered by the event generator, the ones in the middle are obtained after passing through the simulated detectors and the analysis code. The bottom distributions show the efficiencies obtained by dividing the middle distributions by the top ones. Incoming beam energy: 400 MeV.

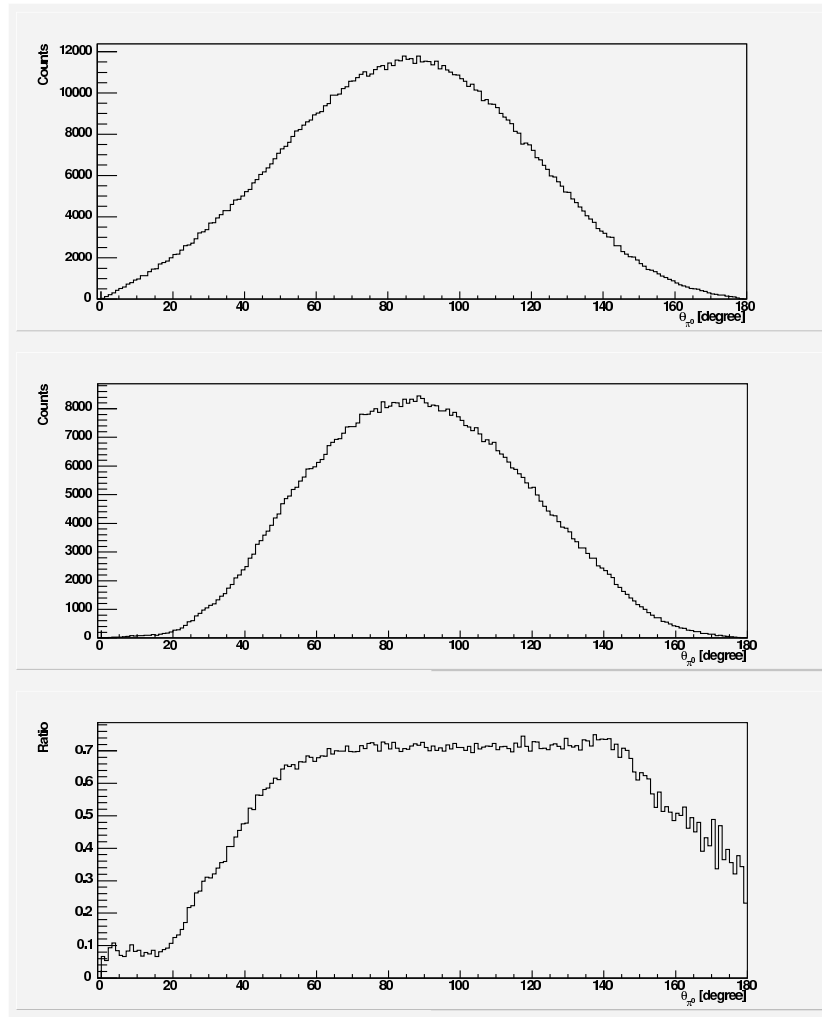


Figure 5.25: Detector efficiency used for the extraction of the  $\theta_{\pi^0}$  differential cross section. Incoming beam energy: 400 MeV.

Practically the cross section extraction is performed via several ROOT macros achieving the following steps:

- 1) The readout of the remaining statistics of the wanted variable.  $\rightarrow N_{events}$
- 2) The readout of the scalers  $N_{e^-}$  and the tagging efficiency  $\eta_{tagg}$  in the file corresponding to the beamtime
- 3) The multiplication of the tagging efficiency with the scalers  $\rightarrow N_{e^-} \cdot \eta_{tagg}$
- 4) The addition of the statistics obtained by 1) and 3) for all beamtimes

- 5) The division of the sums obtained by 1) by the sum of 3)  $\rightarrow \frac{N_{events}}{N_{e^-} \cdot \eta_{tagg}}$
- 6) The readout of the detector efficiency  $\epsilon_{CBTAPS}$  in the file corresponding to the wanted energy range (325-375, 375-425, 425-475 MeV)
- 7) The division of 5) by the detector efficiency  $\epsilon_{CBTAPS} \rightarrow \frac{N_{events}}{N_{e^-} \cdot \eta_{tagg} \cdot \epsilon_{CBTAPS}}$
- 8) The division of 6) by the constant factor  $\Lambda_{\pi^0 \rightarrow \gamma\gamma}$  and  $\rho_t$

### 5.5.2 Final Background Substraction

As seen in the chapter "Channel Identification", it is not possible to remove all the background with the cuts. We can notice on the final plots of background channels (see *Cut Overview*) an excellent removal of single  $\gamma p \rightarrow \pi^0 p$  but, however, a not negligible remaining  $\gamma p \rightarrow \pi^0 \pi^0 p$  background. Due to this fact, the cross section related to latter background has to be estimated and subtracted from our  $\gamma p \rightarrow \pi^0 p \gamma'$  cross sections. This is reached by determining fraction of  $\gamma p \rightarrow \pi^0 \pi^0 p$  events surviving the cuts and combine it with its start cross section (known from [Zeh08]). Detailed way to proceed:

- 1) We build a kind of "background double  $\pi^0$  efficiency"  $\epsilon_{2\pi^0}^{bg}$  by dividing the final beam energy spectrum of the simulated  $\gamma p \rightarrow \pi^0 \pi^0 p$  events by its start distribution. See figure 5.26.
- 2) For each energy range (350,400,450), we determine a  $\sigma_{2\pi^0}^{bg}$ , which is the remaining *background* total cross section of the double  $\pi^0$  channel and obtained via:

$$\sigma_{2\pi^0}^{bg} = \epsilon_{2\pi^0}^{bg} \cdot \sigma_{2\pi^0}^{real} \quad (5.19)$$

Where  $\sigma_{2\pi^0}^{real}$  is the known total cross section of the double  $\pi^0$  for the wanted energy range. The used  $\sigma_{2\pi^0}^{real}$  values are taken from figure 5.12.

- 3) We then have to distribute our total cross section  $\sigma_{2\pi^0}^{bg}$  in an angular/energy distribution. In an analysed  $\gamma p \rightarrow \pi^0 \pi^0 p$  simulation file, we register from the  $E_{\gamma'}$  and  $\theta_{\gamma'}$  the number of counts  $N_{2\pi^0}$  in each Energy/ $\theta$  bin. We then integrate these distributions to get a kind of total "Total Cross Section"  $N_{2\pi^0}^{tot}$  for the wanted energy range.

Building the ratio:  $N_{2\pi^0}^{tot} / \sigma_{2\pi^0}^{tot}$  for the accordant energy range we obtain the scale factor between the number of counts  $N_{2\pi^0}$  of the histogram bin and

the corresponding  $\gamma p \rightarrow \pi^0 \pi^0 p$  differential cross section value of this. Finally multiplying this scale factor with each of the  $N_{2\pi^0}$ , we obtain for each bin (Energy or  $\theta$ ) of our differential cross section, the corresponding remaining cross section of the background double  $\pi^0$  channel.

4) We finally subtract for each bin this background contribution.

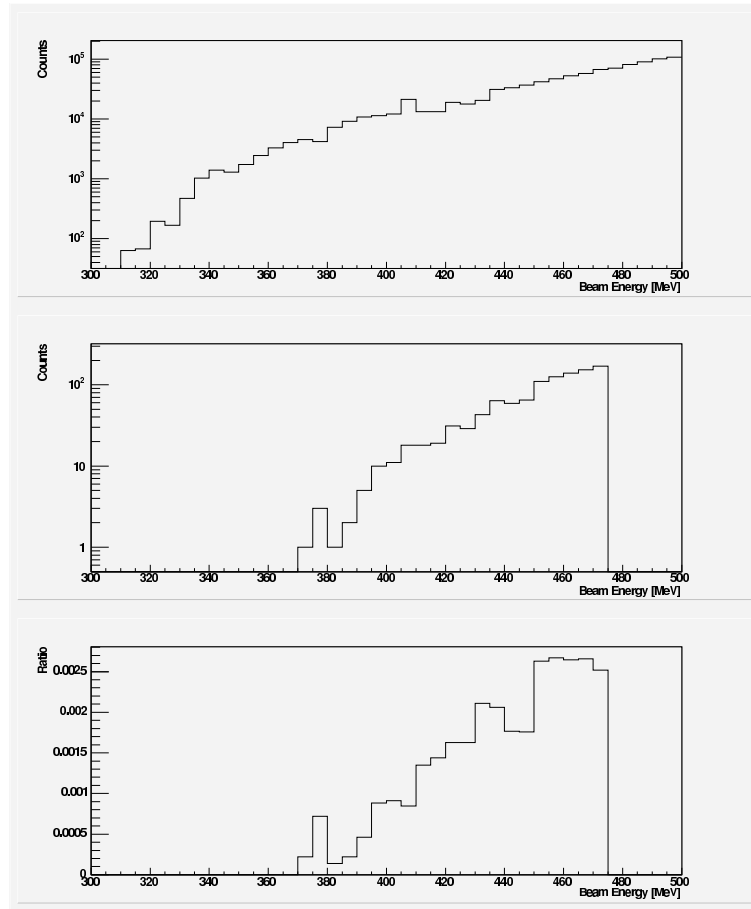


Figure 5.26:  $\epsilon_{2\pi^0}^{bg}$  : View of remaining  $\gamma p \rightarrow \pi^0 \pi^0 p$  background depending on the beam energy. TOP: Raw Generated  $\gamma p \rightarrow \pi^0 \pi^0 p$  events. MIDDLE: Remaining distribution after detection and all the cuts. BOTTOM: Ratio of the first and second distribution: Proportion of remaining background depending on the incoming beam energy.

### 5.5.3 The Empty Target Runs Substraction

As already mentioned in the *Setup* chapter concerning the target, an ice layer appeared during our measurements on the surface of the target. In order to remove the part of cross sections due to this effect and generally to remove any cross section participation due to the kapton target window, several *empty target* runs have been taken.

These runs have then been analysed and differential cross sections have been extracted in the same way as for standard runs. The obtained empty target cross section has been finally subtracted from the MDM and single  $\pi^0$  cross sections.

In order to obtain reasonable statistics, empty target runs of all the beam-times are added and analysed. For the  $\gamma p \rightarrow \pi^0 p \gamma'$  where the statistics remains very low, the empty target differential cross sections have been fitted before the subtraction. The applied fit was a constant fit for the energy differential cross section and an *ABC - Fit* for the angular distributions. The *ABC - Fit* is a function:  $A + B \cdot \cos(\theta) + C \cdot \cos^2(\theta)$  and is currently used of angle distributions.

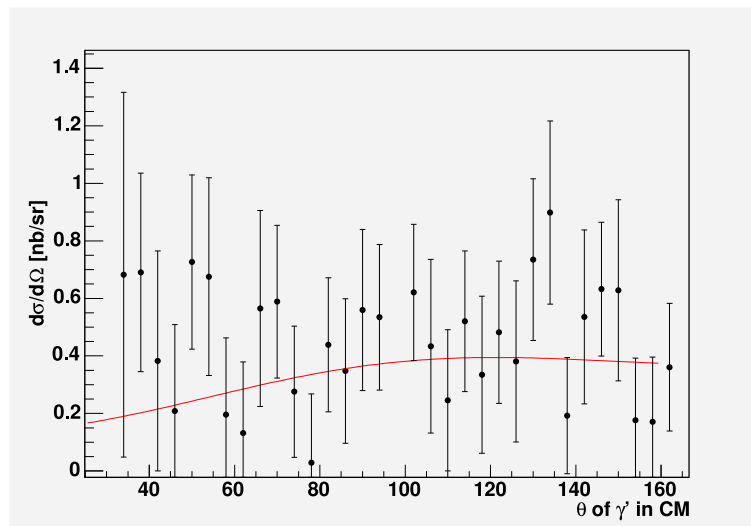


Figure 5.27: Example of  $\gamma p \rightarrow \pi^0 p \gamma'$  empty target differential cross section with the applied fit. Energy of incoming beam: 375-425 MeV.

## 5.5.4 Systematic Errors

### Asymmetries

Parameters inducing systematic errors in the determination of asymmetries are the following:

- The uncertainty on the degree of polarisation of the electrons: **5%** (see chapter 3.2.2)
- The remaining  $\gamma p \rightarrow \pi^0 \pi^0 p$  background estimated from figure 5.26 for the two beam energy ranges:
  - $E_\gamma = 400$  MeV: **0.009 %**
  - $E_\gamma = 475$  MeV: **0.25 %**

Multiplying this with the highest measured circular asymmetry of this channel [Kram07]: **8 %**

This leads to a total systematic error for the circular asymmetry of **6.5 %**.

### Differential Cross Sections

Parameters inducing systematic errors in the determination of differential cross sections are the following:

- The tagging efficiency variation determined for each beamtime reaches its highest value by **2%** (from [Dow07])
- The error from the photon flux and the target density have been estimated in [Dow07] with a value of **4.5 %**
- The error due to the tagger 4x4 structure can be rated from figure 4.22 to **7%**
- The detector efficiency uncertainty can be evaluated by comparing the efficiency resulting with different start distributions and cuts combinations. This value depends on the analyzed channel:

- Detector efficiency discrepancy in the  $\gamma p \rightarrow \pi^0 p \gamma'$  analysis: **12 %**
- Detector efficiency discrepancy in the  $\gamma p \rightarrow \pi^0 p$  analysis: **5 %**

Total systematic error of the differential cross sections of  $\gamma p \rightarrow \pi^0 p \gamma'$  analysis: **15 %**

Total systematic error of the differential cross sections of  $\gamma p \rightarrow \pi^0 p$  analysis: **10 %**

# Chapter 6

## Results and Discussion

### 6.1 Asymmetries

The circular asymmetries  $\Sigma_{circ}$  have been determined for two different incoming photon beam energy ranges. They were first extracted for  $E_\gamma = 375 - 425$  MeV, this beam energy being the most appropriate range for our  $\gamma p \rightarrow \pi^0 p \gamma'$  reaction. Another  $\Sigma_{circ}$  has been subsequently extracted with  $E_\gamma > 450$  MeV, i.e. with a beam energy range of 450-475 MeV, as our analysis incoming beam condition stops by 475 MeV. This second extraction was done in the view to have a circular asymmetry in a region that is not disturbed by the linear polarisation edge at 400 MeV.

The present results are based on two different polarisation setups:

- 1) 87 % of our data have been taken with an incoming electron beam energy of 883 MeV and a circular polarisation degree between 20 % and 47% (in our photon beam range of interest), see figure 5.22. For these beamtimes, the photon linear polarisation was in priority of interest and polarisation edge lay by  $E_\gamma = 400$  MeV.
- 2) 13 % of our data have been taken in January 2004 with a special setup privileging the *circular* polarisation with an electron beam energy of 570 MeV and thus a circular polarisation degree between 35 % and 82 % (in our photon beam range of interest), see figure 5.22. Moreover, the photons were not linear polarised.

Circular asymmetries have been extracted from these two data packages separately, as due to participation of linear polarisation in the first package, the corresponding outgoing asymmetries can not be compared. Note that the polarisation bit by January beamtime had to be inversed [Kram07].

## 1) Circular Asymmetry with data from "standard" setup (1):

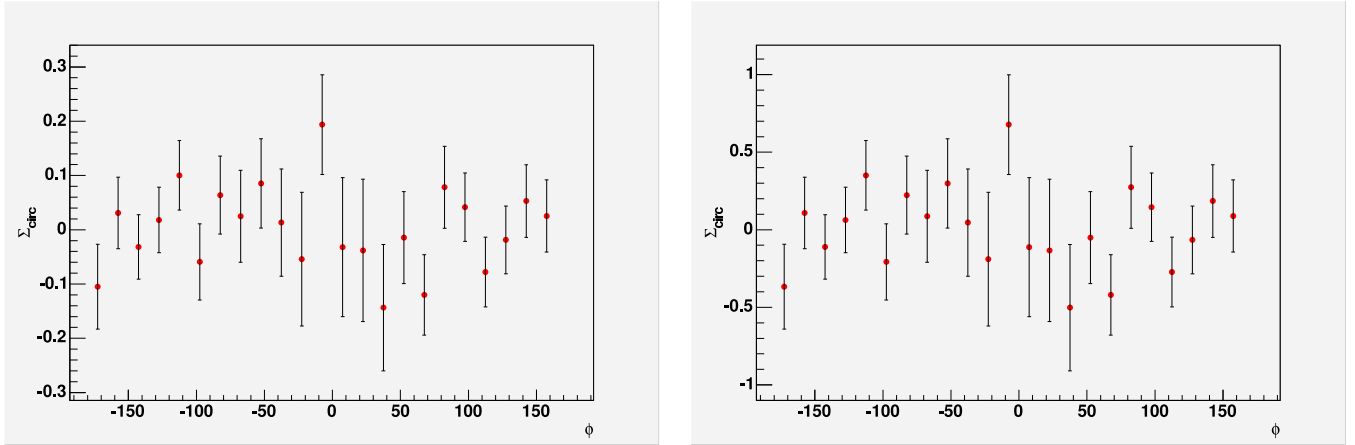


Figure 6.1: Circular asymmetry on the  $\phi$  angle between reaction planes, incoming beam energy: 375-425 MeV. LEFT: No consideration of degree of polarisation. RIGHT: With degree of polarisation.

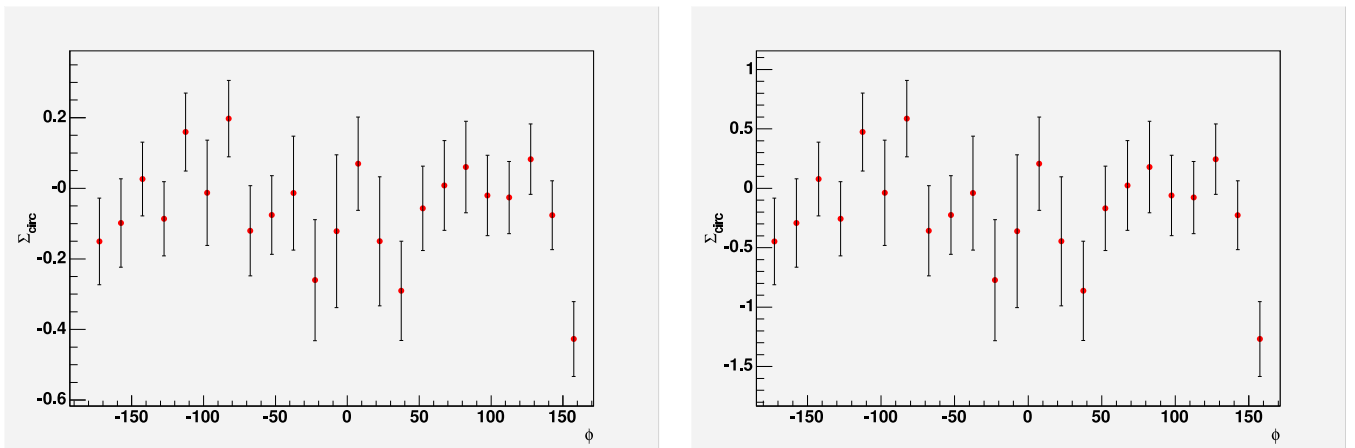


Figure 6.2: Circular asymmetry on the  $\phi$  angle between reaction planes, incoming beam energy: 450-475 MeV. LEFT: No consideration of degree of polarisation. RIGHT: With degree of polarisation.



## 2) Circular Asymmetry with data from "special" January setup (2):

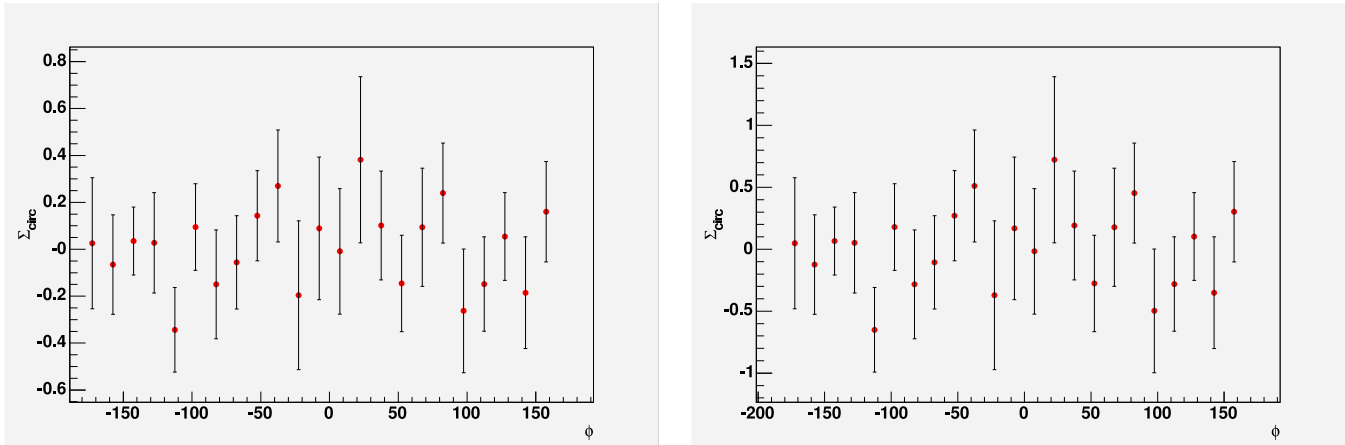


Figure 6.3: Circular asymmetry on the  $\phi$  angle between reaction planes, incoming beam energy: 375-425 MeV. LEFT: No consideration of degree of polarisation. RIGHT: With degree of polarisation.

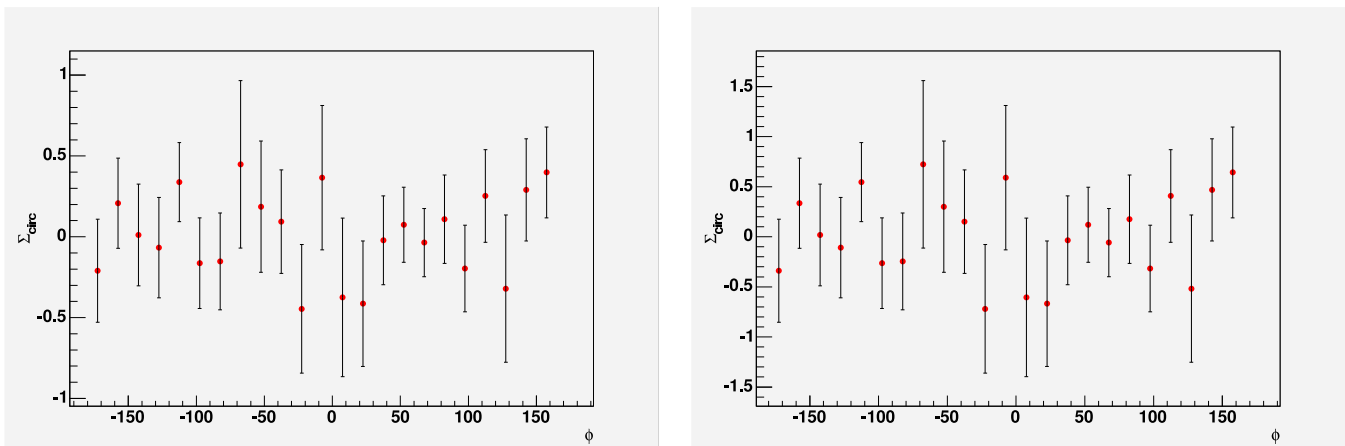


Figure 6.4: Circular asymmetry on the  $\phi$  angle between reaction planes, incoming beam energy: 450-475 MeV. LEFT: No consideration of degree of polarisation. RIGHT: With degree of polarisation.

Apart from the lower statistics due to the narrow photon beam window of the second asymmetries, the fluctuations observed for  $E_\gamma = 375 - 425$  MeV are mainly reproduced for  $E_\gamma = 450 - 475$  MeV.

It is difficult to distinguish a structure on the present asymmetries, especially because of the large statistical error. The latter can be attributed on one hand to the fact that the high statistics part of our data (setup 1)) has a low polarisation degree and on the other hand to the only low amount of data owning a high polarisation degree (setup 2)).

## 6.2 Cross Sections

### 6.2.1 The single $\pi^0$ Differential Cross Sections

For this *background* channel, only the differential cross sections depending on the  $\theta$  angle of the  $\pi^0$  have been determined. They are an important cross check for the general analysis frame and essential for the determination of the final **R**-ratio cross sections shown later.

They are for this latter purpose determined for exactly the same beam energy ranges as the MDM differential cross sections.

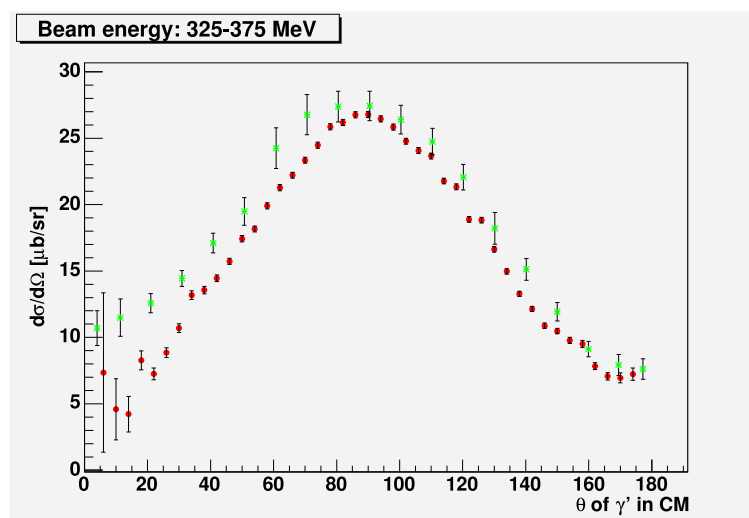


Figure 6.5: Angular differential cross section of the single  $\pi^0$  channel. Photon beam energy range: 325-375 MeV. The green dots are from [Leu01].

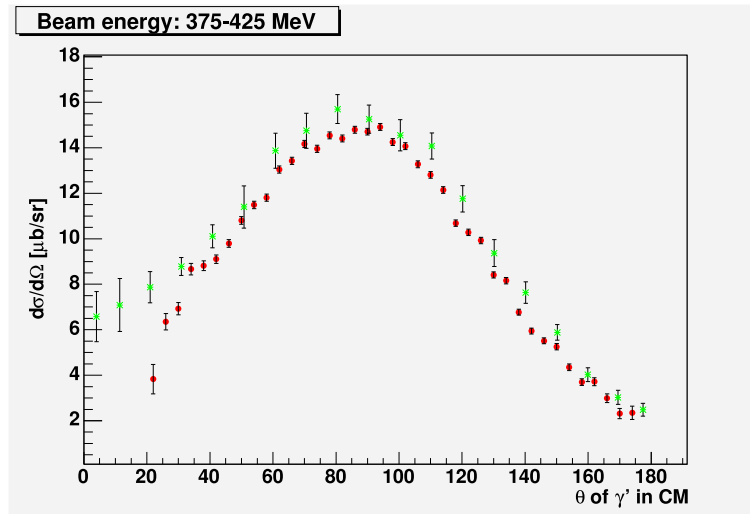


Figure 6.6: Angular differential cross section of the single  $\pi^0$  channel. Photon beam energy range: 375-425 MeV. The green dots are from [Leu01].

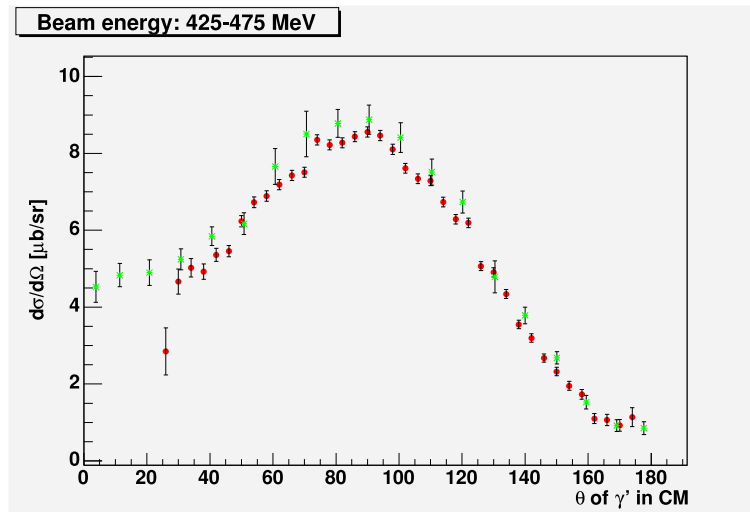


Figure 6.7: Angular differential cross section of the single  $\pi^0$  channel. Photon beam energy range: 425-475 MeV. The green dots are from [Leu01].

The present cross check analysis of the  $\gamma p \rightarrow \pi^0 p$  channel shows a good agreement with the previous measurement of [Leu01] and thus brings a reliable basis for the extraction of our R-ratio differential cross sections shown later.

## 6.2.2 The $\gamma p \rightarrow \pi^0 p \gamma'$ Differential Cross Sections

### The angular differential Cross Sections

The angular differential cross sections can be used for the estimation of the  $\mu_{\Delta^+}$ , but are especially an additional check of our  $\gamma p \rightarrow \pi^0 p \gamma'$  analysis. Theoretical curves from [Pas05] are shown as comparison, as well as the similar differential cross from the pioneer measurement of M.Kotulla [Kot01].

They are produced for the usual three incoming beam energy ranges: 325-375 MeV, 375-435 MeV, 425-475 MeV

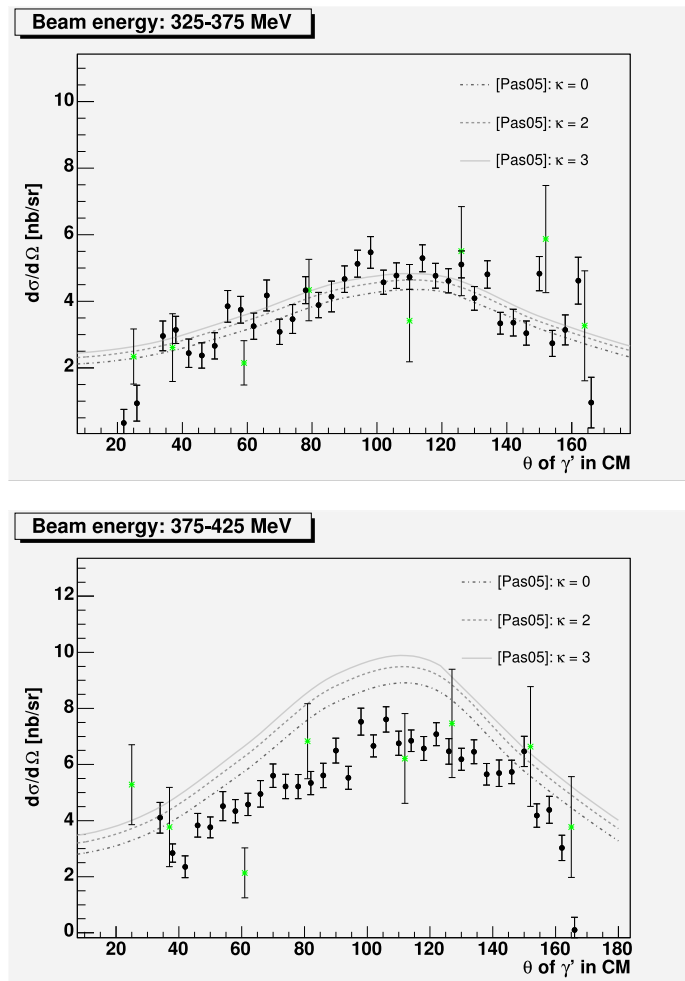


Figure 6.8: Angular differential cross section of the radiative photon  $\gamma'$ . Photon beam energy range: UP: 325-375 MeV, BOTTOM: 375-425 MeV. The green dots are from [Kot01].

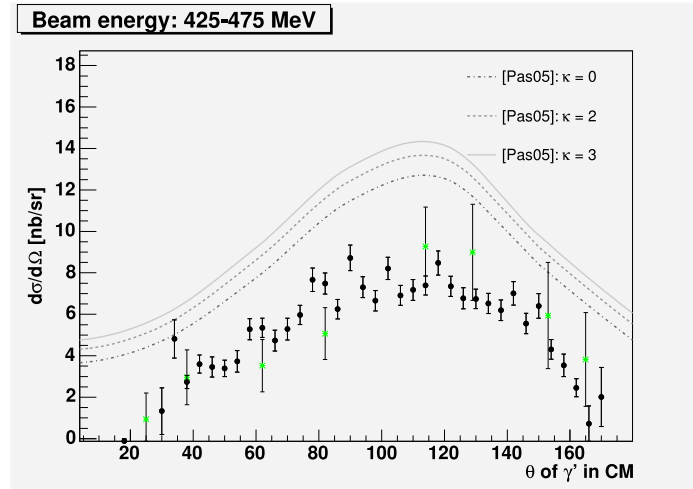


Figure 6.9: Angular differential cross section of the radiative photon  $\gamma'$ . Photon beam energy range: 425-475 MeV. The green dots are from [Kot01].

We first notice the great improvement in statistics, in comparison to the previous measurement.

Moreover, we see a good agreement with the previous measurement as well as with theoretical calculations in the low beam energy range of 325-375 MeV. The discrepancy with the theoretical curves in the high beam ranges remains considerable, although this may be improved with forthcoming calculations, as this will be shown by the energy differential cross sections.

### The Energy differential Cross Sections

The differential cross sections built on the energy of the radiative photon  $\gamma'$  are part of the key for the extraction of  $\mu_{\Delta^+}$ , as they are the basis of our R-ratio cross sections. They are built for the three usual energy ranges and are compared with the previous measurement of the  $\gamma p \rightarrow \pi^0 p \gamma'$  channel and theoretical calculations from [Pas05]. Moreover, we own for the present variable most recent calculations from [Pas07] showing a promising future.

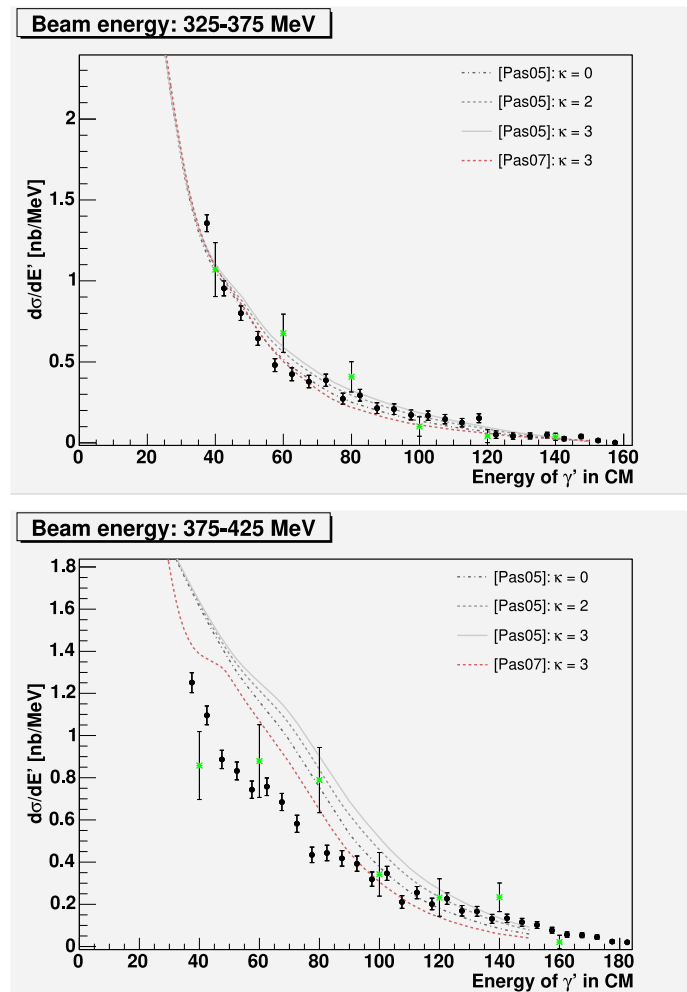


Figure 6.10: Energy differential cross section of the radiative photon  $\gamma'$ . Photon beam energy range: UP: 325-375 MeV, BOTTOM: 375-425 MeV. The green dots are from [Kot01].

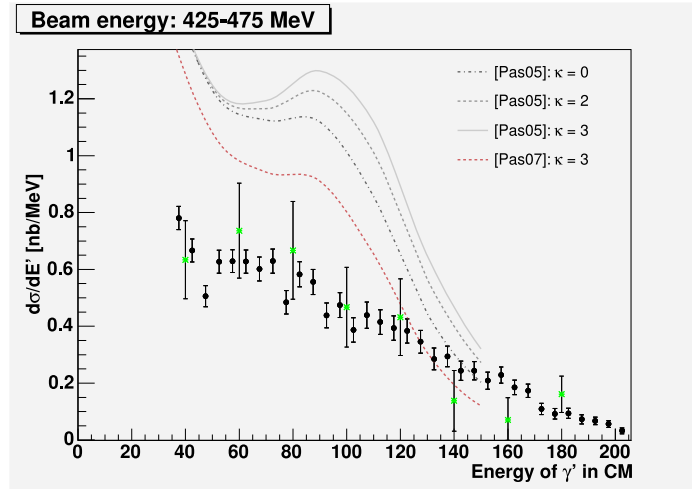


Figure 6.11: Energy differential cross section of the radiative photon  $\gamma'$ . Photon beam energy range: 425-475 MeV. The green dots are from [Kot01].

Consistently to the angular differential cross sections, the agreement of the energy differential cross section with the theoretical calculations is optimal for the low beam energy range of 325-375 MeV. The similarity with the previous measurement is also visible, the largest discrepancy being for the middle energy range of 375-425, as it is the case for the angular DCS.

Recent published theoretical calculations involving more diagrams at NLO in the  $\delta$  expansion (fig. 5.11) and rescattering loops (fig. 5.12) show a promising accordance evolution between the theory and our data. An example for  $\kappa = 3$  is shown on the upper energy differential cross sections. As a matter of fact, we notice a visible shift of these latest calculations towards our data, as the theory curves remain almost unchanged for the low beam energy range and particularly drop for the high energy range.



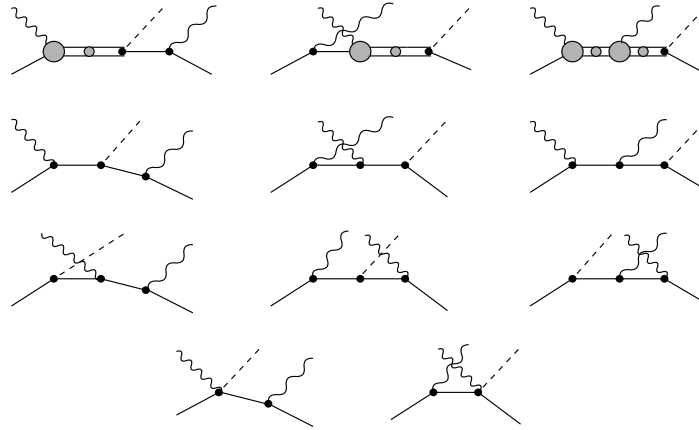


Figure 6.12: ]

Diagrams for  $\gamma p \rightarrow \pi^0 p \gamma'$  reaction at NLO in the  $\delta$  expansion considered in [Pas07]. Double lines represent the  $\Delta$  propagators.

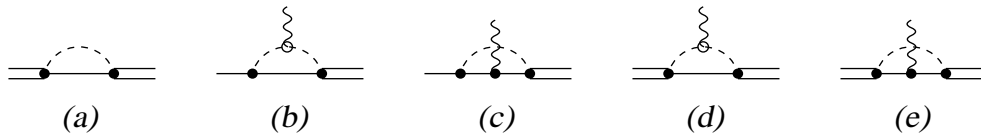


Figure 6.13: Chiral loop corrections considered in [Pas07], additional diagrams are noticed in comparison to figure 2.10.

### The $R$ differential Cross Sections

In order to obtain the best conditions for comparing our differential cross sections with the theoretical models and especially to fulfill the behavior at the soft photon limit where  $E_{\gamma'}$  tends to 0 and  $\gamma p \rightarrow \pi^0 p \gamma'$  goes to  $\gamma p \rightarrow \pi^0 p$ ,  $R$ -ratio cross sections are produced. These differential cross sections are based on the energy of the radiative photon and use single  $\pi^0$  differential cross sections (See eq. 2.19):

Condition at the soft-photon limit:

$$\lim_{E_{\gamma'} \rightarrow 0} \left( \frac{d\sigma}{dE_{\gamma'}} \right) = \frac{1}{E_{\gamma'}} \cdot \sigma_0 \quad (6.1)$$

$$R = \frac{d\sigma}{dE_{\gamma'}} \cdot E_{\gamma'} / \sigma_0 \quad (6.2)$$

With:

$$\begin{aligned} \sigma_0 &= \int d\Omega_{\pi^0}^{CM} \left( \frac{d\sigma}{d\Omega_{\pi^0}} \right)^{CM} \cdot \frac{2\alpha_{em}}{\pi} \cdot W(v) \quad (6.3) \\ W(v) &= -1 + \frac{v^2 + 1}{2v} \cdot \ln\left(\frac{v+1}{v-1}\right) \\ v &= \sqrt{1 - \frac{4m_p^2}{t}} \quad , \\ t &= (k - p_{\pi^0})^2 \quad (6.4) \end{aligned}$$

$d\sigma/d\Omega_{\pi^0}$  labels the differential cross section for  $\pi^0 p$  production,  $m_p$  the proton mass,  $t$  the four momentum transfer between the initial photon and the  $\pi^0$  meson and  $\alpha_{em} = e^2/4\pi \approx 1/137$ . The energy differential cross section divided by  $\sigma_0/E_{\gamma'}$  should be equal to 1 in the limit of zero photon energy  $E_{\gamma'}$ .

The weight function  $W(v)$  is produced in a macro and we see here its dependence on  $\theta_{\pi^0}^{CM}$  for our three energy ranges:

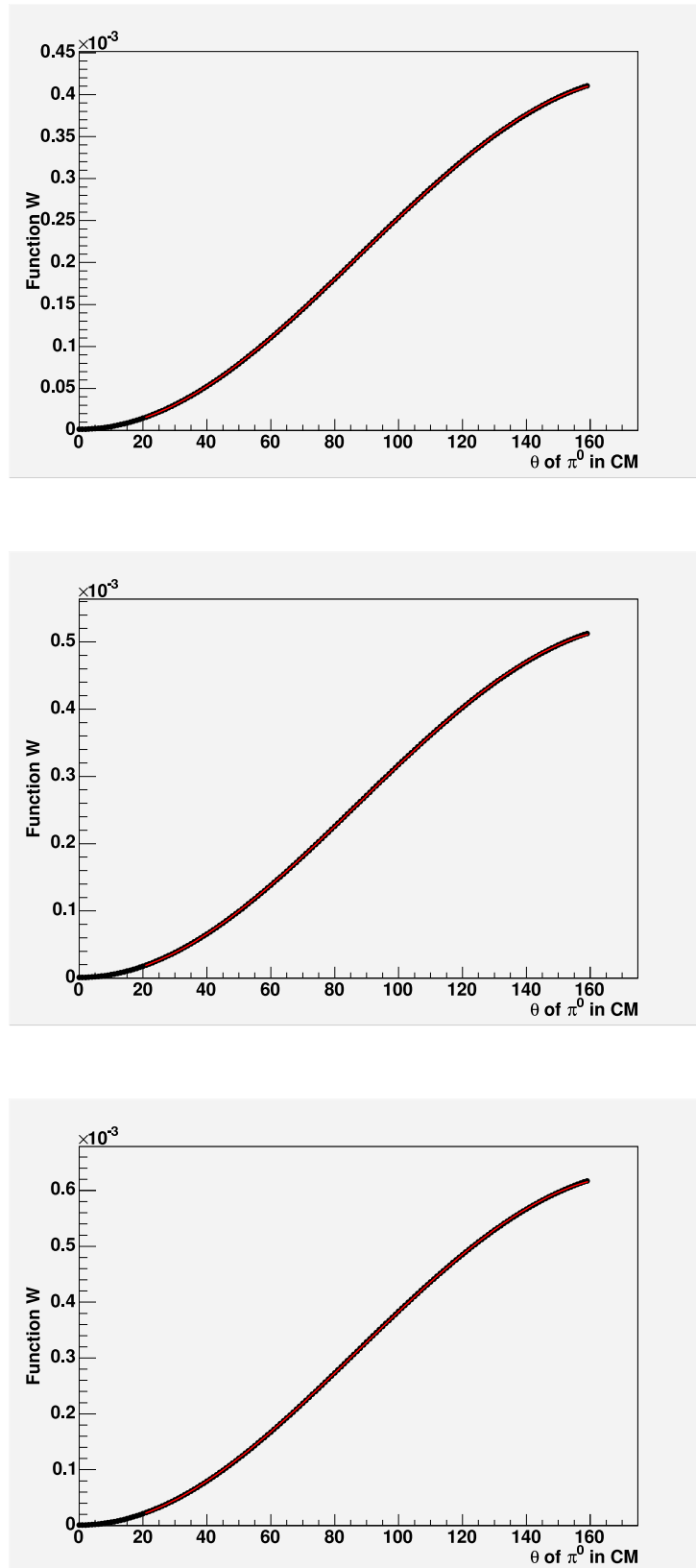
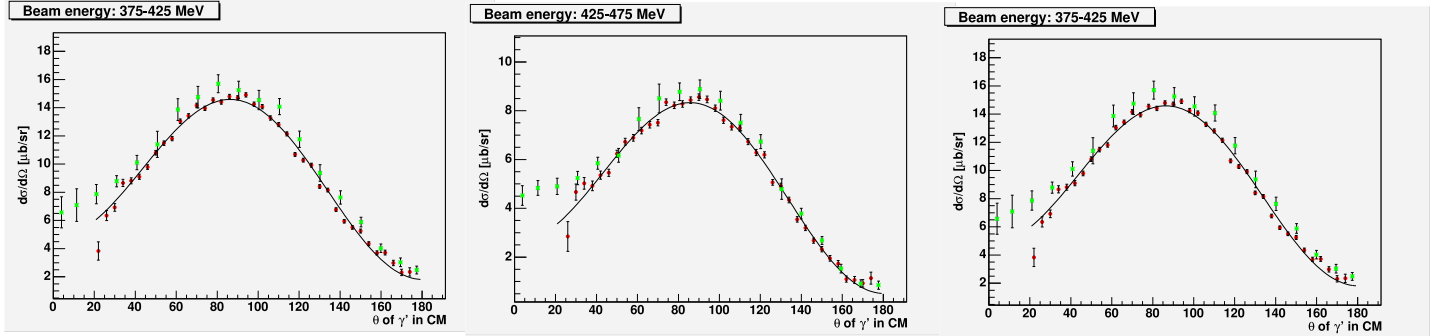


Figure 6.14: View of the weight function used for the  $\sigma_0$  determination. Note that the factor  $\frac{2\alpha_{em}}{\pi}$  is already implemented in  $W(v)$ . The applied  $P3$  fit is used to simplify the integration of the  $\gamma p \rightarrow \pi^0 p$  over the solid angle  $\Omega$ .

In order to optimize the integration for the determination of  $\sigma_0$  (see equ.5.3), the  $W(v)$  function has been fitted as well as the  $\gamma p \rightarrow \pi^0 p$  differential cross sections. These 2 fits have finally been multiplied and integrated over the solid angle  $\Omega$ .



The obtained  $\sigma_0$  values for 3 different ways to proceed have been compared:

- 1) We integrate data point per data point of the differential cross sections multiplied with  $w(v)$ . Under 25 degrees, where the DCS begins to fluctuate, we replace the data points by the ones produced with the fit.
- 2) We create new points from the fit, using the same binning as for the data points and then sum them in the same way as for data points.
- 3) We create the function `Final_Funct` which is a multiplication of the ABC Fit by the  $P3$  fit of the  $W(v)$ . We then integrate this `Final_Funct` from 0 to 180 degrees and apply the constant factors for an integration over the all solid angle  $\Omega$  in radians.

Result of  $\sigma_0$  ([nb]) for the three energy ranges, using the different methods:

beam energy	way 1)	way 2)	way 3)
350	65.957	64.930	65.761
400	42.836	43.014	43.624
450	27.835	27.961	28.372

We notice an only minimal difference between the integration methods and thus the third way to proceed was finally chosen. Note that the fluctuations of the DCS below  $25^\circ$  are not much disturbing our  $\sigma_0$ , as the multiplicative weight function  $W(v)$  has its minimum in this region.

We see here on the one side a comparison between M. Kotulla's R-ratios and the theoretical curves from [Pas05] and on the other side our results for the R-ratios compared with the same theoretical calculations.

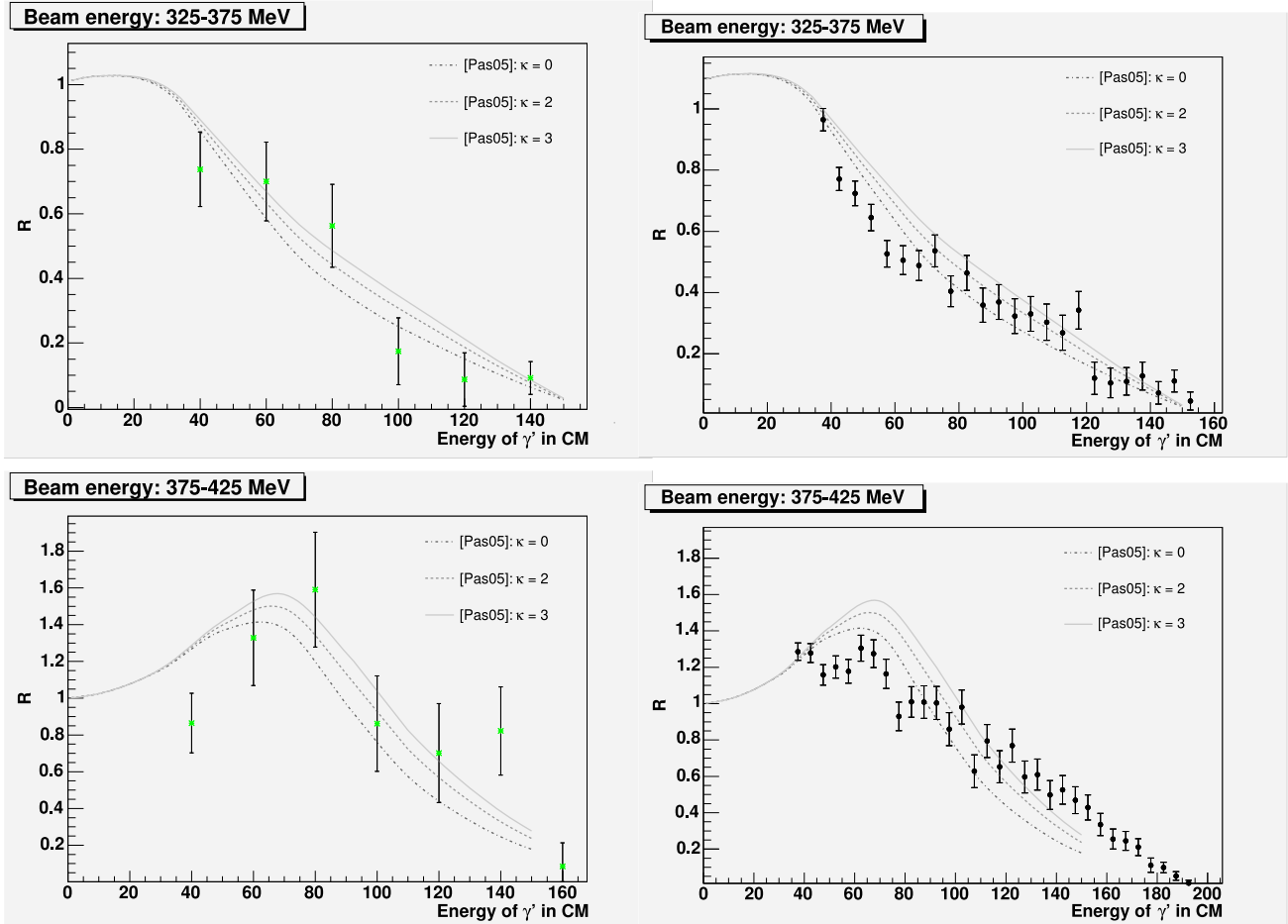


Figure 6.15: Ratio differential cross section on the energy of the radiative photon  $\gamma'$ . LEFT: Data from [Kot1], RIGHT: Data of the present work. Photon beam energy range: UP: 375-425 MeV, BOTTOM: 375-425 MeV.

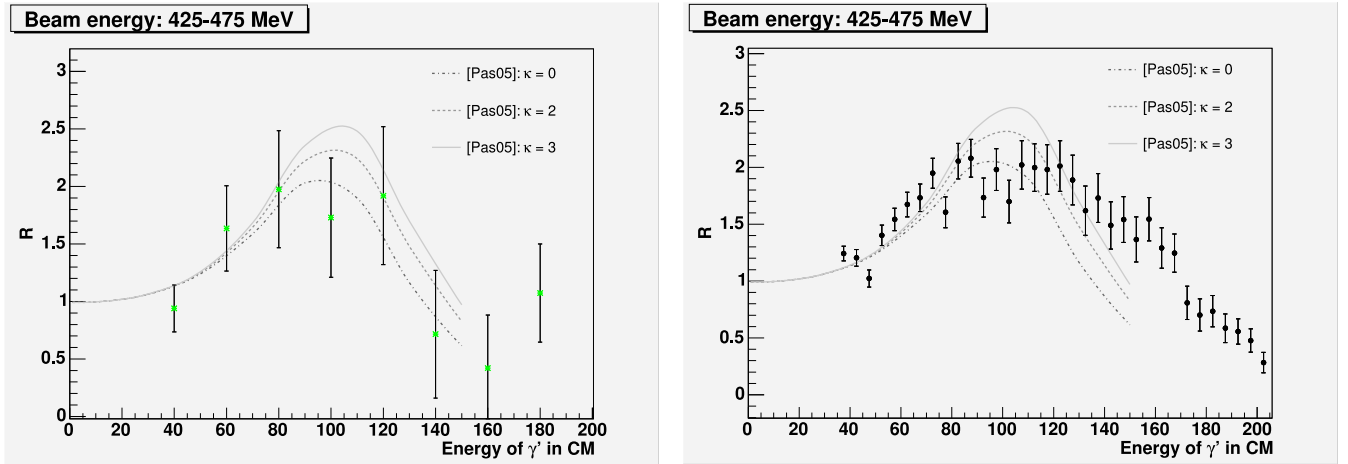


Figure 6.16: Ratio differential cross section on the energy of the radiative photon  $\gamma'$ . LEFT: Data from [Kot1], RIGHT: Data of the present work. Photon beam energy range: UP: 375-425 MeV, MIDDLE: 375-425 MeV, BOTTOM: 425-475 MeV.

We first notice here the consistency of our R-ratios with the expected value of 1 at the soft photon limit. The discrepancy of our data with [Kot01] and [Pas05] in the beam energy range of 375-425 MeV remains considerable. However, the R-ratio variable brings theory curves closer to the data for the higher energy range of 425-475 MeV.

We may, for the determining variable, expect an even broader improvement with the new calculations, as these have also been improved by the description of the  $\gamma p \rightarrow \pi^0 p$  (fig. 5.16) channel that takes part of this cross section.



Figure 6.17: Diagrams for  $\gamma N \rightarrow \pi N$  reaction at NLO in the  $\delta$  expansion considered in [Pas07]. Double lines represent the  $\Delta$  propagators.

## 6.3 Conclusion and Outlook

Considering the aim of this work, i.e the determination of the  $\Delta^+$  dipole moment with a much higher statistics, the present results *partially* reached this goal. The comparison of the present cross section with the previous ones of [Kot01] reflects a clear improvement in the statistics, as well as a confirmation of the previous values built on a limited amount of data. The today's poor agreement between the data and the theoretical calculations restrains strongly the extraction of the  $\mu_{\Delta^+}$ . The only weak difference between the differential cross sections curves with the different values of the anomalous moment  $\kappa$  asks for a near to perfect agreement of the data with one of the  $\kappa$  theoretical distribution. The expected large effect of the MDM on the *circular asymmetry* delivered by the theoretical calculations presaged a much easier  $\mu_{\Delta^+}$  extraction via this latter variable. The present experimental determination of  $\Sigma_{circ}$  however does not show an enough reliable structure demonstrating a real presence of circular asymmetry in the  $\gamma p \rightarrow \pi^0 p \gamma'$  channel.

The reproduction of  $\gamma p \rightarrow \pi^0 p \gamma'$  and  $\gamma p \rightarrow \pi^0 p$  cross sections in comparison to previous measurements however shows reliability of the experimental setup and analysis.

Possible improvements that could allow the extraction of  $\mu_{\Delta}$  based on the present data are the following:

The fact that the differential cross sections of  $\gamma p \rightarrow \pi^0 p \gamma'$  and minimal of  $\gamma p \rightarrow \pi^0 p$  tend to lie lower than the previous ones, a check on a possible data loss could be performed. The particle identification could be improved, as on one hand the TAPS vetos delivered a low efficiency and on the other hand some of the PID fibers broke down during the September beamtime. The basic condition for a  $\gamma p \rightarrow \pi^0 p \gamma'$  event being to own a proton, a not perfect identification of the latter can lead to a loss of events in this channel.

The highest improvement expectations concern the evolution of the theoretical calculations. The last published results [Pas07] including more chiral loop corrections and NLO diagrams in the  $\delta$  - *expansion* show a clear decrease of the differential cross sections, this decrease growing with the incoming energy, see figure 5.9, 5.10. The latter evolution corresponds to the evolution of the discrepancy between the results of the present work and the theoretical curves from [Pas05].

Meliorations for forthcoming experiments could be the following:

- Concentrate more beamtime in view of circular asymmetry, i.e., take more data with lower beam energy ( 500 MeV), higher degree of circular polarisation and no linear polarisation. The short January 2004 beamtime with a similar setup did not deliver enough statistics to extract an asymmetry from these data only and thus avoid a possible disturbance, due to the linear polarisation edge around 400 MeV.
- A remedy should be found against the large forward direction electromagnetic background present in TAPS.
- The area between the two detectors TAPS and CB should be arranged in another way to avoid rescattering background with experiment material therein. This has already been done for the today's running experiments in A2.

In the view of coming research this now twice tested way of dipole moment extraction using a radiative photon emission opens the door to the study of other  $N^*$  resonances. A proposal has already been submitted about the extraction of the MDM of the  $S_{11}$  (1535) (see figure 6.16) studying the reaction:

$$\gamma p \rightarrow S_{11} \rightarrow S_{11} \gamma' \rightarrow \eta \gamma' p$$

This study is of special interest, as it could deliver key about the controverted non-qq nature of this hadronic system.

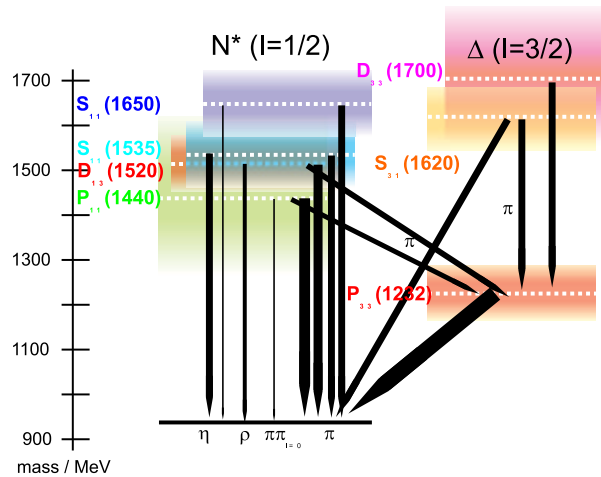


Figure 6.18:  $N^*$  excitations in the  $\Delta$  resonance region



# Acknowledgments

Mein allererster Dank geht an meinen Doktorvater *Bernd Krusche*. Er hat mir die Chance gegeben, auf seinem ausserordentlichen Forschungsgebiet zu arbeiten. Er hat mir sehr viel Disponibilität angeboten und gezeigt, wie Schwierigkeiten überwinden und nach Lösungen zu suchen.

Gleich danach geht meine Dankbarkeit an *Martin Kotulla*, mein Postdoc. In Basel und später in Giessen ist er mir als "MDM-Spezialist" mit sehr viel Geduld zur Seite gestanden. Grosse und wichtige Fortschritte haben mir meine Aufenthalte im *Justus Liebig - Physik Institut II* erlaubt. Soviele Male ich dort wieder auftauchte, immer wurde ich von den Mitarbeitern der *Volker Metags Gruppe* mit Wohlwollen empfangen. Ihre stets warme Unterstützung habe ich sehr geschätzt. Ein besonderer Dank geht an *Ralf* und *Stefan*, die ich gelegentlich der "Schwitzstunden" beim TAPS - Aufbau kennengelernt habe, und mit denen ich dann unvergessliche Arbeit- aber auch Spassmomente geteilt habe.

Die *A2-Kollaboration* bringt mich nach Mainz zu *Sven*. Tausende von hilfreichen Mailzeilen verdanke ich ihm, sowie eine privilegierte und nette ;-) Arbeitszeit im *Institut für Kernphysik*.

In Mainz konnte jede(r) auch auf *Dirk* zählen. Bei der Experimentszeit war jeweils bei ihm Hilfe zu finden, und er hatte immer eine Lösung bereit. Mit ihm versüsste sich die trockene Welt der Physik mit Schweizer Kakao ;-) Das bringt mich zur *Grossen Evie* and yes, Evie, you are! It was great for me to spend this PhD time with you, the "Born Physicist" and "Wonderwoman".

My gratitude to the whole *A2-Collaboration*. I was very lucky to accomplish my PhD work in a such helpful and friendly team.

Retour à Bâle, pour finir d'où je viens. Une grande reconnaissance à *Cédric Carasco*, le "Maître Yoda" de mon diplôme devenu postdoc hors pair, riche en conseils, soutien moral et délires de la vie. *Francis* et *Yasser*, merci pour ces heures passées aux *FSC*, au "Cargo", à Delémont et au bureau, souvenirs radieux

de mon parcours de thèse. Gratitude à toi *Fabien*, qui m'as supportée durant toutes ces années de thèse avec mes humeurs et mes questions de "Madame tête en l'air". Le bureau 2.12 n'en finit pas résonner de bons souvenirs et de précieux conseils, à vous *Domi, Igal, Thierry* et *Kristoff*, merci. A l'étage au-dessous, j'adresse un merci particulier à *Roman*: dans mes premières hésitations de doctorante il m'a activement soutenue; il a donné d'innombrables heures de son temps afin que nous disposions d'outils informatiques performants.

Plus encore retour aux sources: Delémont et les copines. Maintes fois j'ai eu recours à toi *Chris*, pour me sortir de mes moult crises de thèse, tu es juste la meilleure. Mille merci à *Nathalie* qui m'a tellement soutenue moralement, jusqu'à sacrifier un samedi après-midi au bureau... *Lala, Cotr*, vos messages de soutien et vos coup de fils m'ont considérablement aidée à tenir bon et "continuer le combat".

Mais il y en a deux sans qui je n'en serais pas là aujourd'hui et ce n'est pas seulement parce qu'ils m'ont engendrée: *Papa, Maman*, vous m'avez soutenue dans ce projet de la première à la dernière à heure, mettant à contibution vos très nombreuses qualités, vous avez simplement été *extraordinaires*.

Et parce que c'est avec un soleil au coeur que l'on peut donner le meilleur de soi-même... Merci à toi, *Chou!*

# Appendix

## Determination of the theoretical weight function "W(v)"

$$t = (\mathbf{p}_{beam} - \mathbf{p}_{\pi^0})^2 = m_{beam}^2 - 2E_{beam}E_2 + 2p_{beam}\vec{p}_{\pi^0} + m_{\pi^0}^2$$

in CM :

$$t = (E_{beam}^{CM} - E_{\pi^0}^{CM})^2 - (p_{beam}^{CM} - p_{\pi^0}^{CM})^2 - 4p_{beam}^{CM}p_{\pi^0}^{CM} \sin^2(\theta^{CM}/2)$$

With  $\theta$ , angle between beam and  $\pi^0$  i.e  $\theta_{\pi^0}^{CM}$

$$E_{beam}^{CM} = \frac{s + m_{beam}^2 - m_{target}^2}{2\sqrt{s}}$$

$$= \frac{s - m_{target}^2}{2\sqrt{s}}$$

$$\text{With } s = m_p^2 + 2E_{beam}^{Lab} \cdot m_p$$

$$E_{beam}^{CM} = \frac{2E_{beam}^{Lab} \cdot m_p}{2 \cdot \sqrt{m_p^2 + 2E_{beam}^{Lab} m_p}}$$

$$E_{\pi^0}^{CM} = \frac{s + m_{\pi^0}^2 - m_p^2}{2\sqrt{s}}$$

With the determination of  $t$ , we have all the needed informations to obtain  $v$  and subsequently the weight function  $w(v)$ .



# Tables

## Circular Asymmetries

Data With Standard Setup, Electron Beam = 883 MeV

Incoming Photon Beam Energy:375-425 MeV

Angle $\phi$	Asymmetry No Pol.Deg.	Error No. Pol.	Asymmetry with Pol.Deg.	Error with Pol.
-172.5	0.025210	0.279287	0.047729	0.528762
-157.5	-0.065217	0.212130	-0.123473	0.401617
-142.5	0.035144	0.144710	0.066536	0.273973
-127.5	0.027624	0.213810	0.052300	0.404797
-112.5	-0.343511	0.180518	-0.650355	0.341767
-97.5	0.094650	0.184870	0.179197	0.350006
-82.5	-0.149701	0.232343	-0.283422	0.439884
-67.5	-0.055838	0.198618	-0.105715	0.376036
-52.5	0.142857	0.192354	0.270465	0.364175
-37.5	0.269461	0.238647	0.510159	0.451821
-22.5	-0.196078	0.317159	-0.371227	0.600463
-7.5	0.089109	0.303964	0.168706	0.575483
7.5	-0.008696	0.267369	-0.016463	0.506197
22.5	0.381443	0.354389	0.722170	0.670950
37.5	0.101266	0.231724	0.191722	0.438713
52.5	-0.145833	0.205783	-0.276100	0.389601
67.5	0.093525	0.251933	0.177067	0.476974
82.5	0.239583	0.212863	0.453593	0.403004
97.5	-0.262500	0.263804	-0.496980	0.499448
112.5	-0.148325	0.200910	-0.280818	0.380374
127.5	0.054393	0.186720	0.102980	0.353510
142.5	-0.185185	0.238479	-0.350603	0.451502
157.5	0.160221	0.213792	0.303339	0.404763

**Incoming Photon Beam Energy: 450-475 MeV**

Angle $\phi$	Asymmetry No Pol.Deg.	Error No. Pol.	Asymmetry with Pol.Deg.	Error with Pol.
-172.5	-0.209877	0.319231	-0.338717	0.515202
-157.5	0.208333	0.279085	0.336227	0.450412
-142.5	0.011494	0.315043	0.018550	0.508444
-127.5	-0.066667	0.310440	-0.107593	0.501016
-112.5	0.338462	0.244750	0.546239	0.395000
-97.5	-0.163265	0.280319	-0.263492	0.452404
-82.5	-0.152174	0.299428	-0.245592	0.483243
-67.5	0.448276	0.518100	0.723467	0.836156
-52.5	0.186441	0.405470	0.300894	0.654383
-37.5	0.093333	0.320023	0.150630	0.516481
-22.5	-0.446154	0.397804	-0.720042	0.642011
-7.5	0.365854	0.446173	0.590447	0.720073
7.5	-0.375000	0.490192	-0.605208	0.791116
22.5	-0.413793	0.388409	-0.667816	0.626849
37.5	-0.021277	0.274937	-0.034338	0.443718
52.5	0.074380	0.232421	0.120041	0.375101
67.5	-0.035971	0.210839	-0.058054	0.340270
82.5	0.108911	0.273453	0.175770	0.441323
97.5	-0.196262	0.268589	-0.316744	0.433473
112.5	0.252525	0.286183	0.407548	0.461868
127.5	-0.320755	0.455630	-0.517662	0.735336
142.5	0.290323	0.316056	0.468548	0.510080
157.5	0.398230	0.281534	0.642699	0.454364

**January Data With special Setup, Electron Beam = 570 MeV****Incoming Photon Beam Energy:375-425 MeV**

Angle $\phi$	Asymmetry No Pol.Deg.	Error No. Pol.	Asymmetry with Pol.Deg.	Error with Pol.
-172.5	-0.104854	0.078220	-0.366878	0.273686
-157.5	0.030970	0.065796	0.108363	0.230217
-142.5	-0.031802	0.059345	-0.111273	0.207643
-127.5	0.017971	0.060348	0.062879	0.211152
-112.5	0.100251	0.064084	0.350770	0.224225
-97.5	-0.059155	0.070227	-0.206979	0.245718
-82.5	0.063891	0.071843	0.223550	0.251373
-67.5	0.024823	0.084547	0.086853	0.295823
-52.5	0.085194	0.082263	0.298089	0.287832
-37.5	0.013198	0.098761	0.046179	0.345558
-22.5	-0.054054	0.123103	-0.189131	0.430728
-7.5	0.193694	0.091819	0.677721	0.321269
7.5	-0.032040	0.128264	-0.112107	0.448786
22.5	-0.038095	0.131101	-0.133293	0.458713
37.5	-0.143558	0.116363	-0.502300	0.407146
52.5	-0.014419	0.084607	-0.050451	0.296033
67.5	-0.120060	0.074189	-0.420080	0.259584
82.5	0.078313	0.075465	0.274013	0.264047
97.5	0.041514	0.063110	0.145255	0.220817
112.5	-0.077987	0.064183	-0.272873	0.224571
127.5	-0.018727	0.062356	-0.065523	0.218179
142.5	0.052921	0.066946	0.185167	0.234239
157.5	0.025388	0.066622	0.088830	0.233105

**Incoming Photon Beam Energy: 450-475 MeV**

Angle $\phi$	Asymmetry No Pol.Deg.	Error No. Pol.	Asymmetry with Pol.Deg.	Error with Pol.
-172.5	-0.150358	0.122717	-0.446497	0.364417
-157.5	-0.098398	0.125372	-0.292199	0.372300
-142.5	0.026270	0.104287	0.078009	0.309686
-127.5	-0.086116	0.105123	-0.255726	0.312169
-112.5	0.159370	0.110396	0.473257	0.327827
-97.5	-0.012469	0.149172	-0.037027	0.442975
-82.5	0.197368	0.108326	0.586097	0.321682
-67.5	-0.120163	0.127859	-0.356831	0.379685
-52.5	-0.075885	0.111474	-0.225346	0.331029
-37.5	-0.013477	0.161495	-0.040021	0.479570
-22.5	-0.260188	0.171538	-0.772644	0.509391
-7.5	-0.121495	0.216543	-0.360787	0.643036
7.5	0.069652	0.132137	0.206835	0.392389
22.5	-0.150000	0.182744	-0.445434	0.542669
37.5	-0.290466	0.140648	-0.862555	0.417663
52.5	-0.056940	0.119421	-0.169085	0.354629
67.5	0.007843	0.127210	0.023291	0.377759
82.5	0.060543	0.129653	0.179785	0.385012
97.5	-0.020258	0.114119	-0.060157	0.338882
112.5	-0.026230	0.102278	-0.077890	0.303721
127.5	0.082426	0.099878	0.244769	0.296593
142.5	-0.076443	0.097661	-0.227002	0.290009
157.5	-0.426945	0.106099	-1.267838	0.315067



### 6.3.1 Degree of Polarisation for Electron Incoming Beam Energy of 570.19

Photon Beam Energy	Transfer 570.19	Degree Pola 570.10	Transfer 883.25	Degree Pol 883.25
300.0	0.429663	0.352323	0.236519	0.193946
310.0	0.449979	0.368983	0.246952	0.202501
320.0	0.470610	0.385900	0.257559	0.211198
330.0	0.491533	0.403057	0.268337	0.220037
340.0	0.512728	0.420437	0.279288	0.229016
350.0	0.534171	0.438020	0.290410	0.238136
360.0	0.555836	0.455786	0.301702	0.247396
370.0	0.577696	0.473711	0.313162	0.256793
380.0	0.599720	0.491770	0.324790	0.266328
390.0	0.621877	0.509940	0.336583	0.275998
400.0	0.644135	0.528190	0.348539	0.285802
410.0	0.666456	0.546494	0.360655	0.295737
420.0	0.688806	0.564821	0.372930	0.305803
430.0	0.711146	0.583140	0.385360	0.315995
440.0	0.733436	0.601418	0.397941	0.326312
450.0	0.755636	0.619622	0.410671	0.336750
460.0	0.777704	0.637718	0.423546	0.347307
470.0	0.799599	0.655671	0.436560	0.357979
480.0	0.821277	0.673447	0.449710	0.368762
490.0	0.842695	0.691010	0.462991	0.379652
500.0	0.863811	0.708325	0.476397	0.390645
510.0	0.884582	0.725357	0.489923	0.401737
520.0	0.904965	0.742071	0.503563	0.412921
530.0	0.924920	0.758434	0.517310	0.424195
540.0	0.944405	0.774412	0.531159	0.435551
550.0	0.963383	0.789974	0.545102	0.446984
560.0	0.981815	0.805088	0.559132	0.458488
570.0	0.999667	0.819727	0.573241	0.470058
580.0			0.587421	0.481686
590.0			0.601665	0.493365

## 6.4 The $\gamma p \rightarrow \pi^0 p$ Differential Cross Sections

### 6.4.1 Incoming Photon Beam Energy: 325-375 MeV

$\theta_{\pi^0}$	$d\sigma/d\Omega$ [nb/sr]	Error
14.0	4.219555	1.339238
18.0	8.269921	0.706522
22.0	7.250696	0.446053
26.0	8.851669	0.368855
30.0	10.698201	0.322902
34.0	13.185893	0.321991
38.0	13.562691	0.281621
42.0	14.461419	0.250245
46.0	15.727849	0.238029
50.0	17.430991	0.233679
54.0	18.170647	0.222949
58.0	19.905174	0.226717
62.0	21.272425	0.223391
66.0	22.215375	0.222326
70.0	23.336893	0.222348
74.0	24.475875	0.225883
78.0	25.853423	0.232291
82.0	26.188547	0.230064
86.0	26.760114	0.231069
90.0	26.792012	0.232043
94.0	26.450263	0.230202
98.0	25.837564	0.226527
102.0	24.772328	0.224951
106.0	24.073707	0.220663
110.0	23.655876	0.222880
114.0	21.781319	0.214381
118.0	21.336088	0.219254
122.0	18.886778	0.206109
126.0	18.823269	0.215330
130.0	16.632865	0.207610
134.0	14.973145	0.200802
138.0	13.274019	0.195164
142.0	12.145340	0.197187
146.0	10.879886	0.198725
150.0	10.476883	0.210443
154.0	9.771180	0.234382
158.0	9.502463	0.264144
162.0	7.837374	0.260860
166.0	7.069278	0.283062
170.0	6.944869	0.376778
174.0	7.237125	0.461660
178.0	6.293695	0.775669

**6.4.2 Incoming Photon Beam Energy: 375-425 MeV**

$\theta_{\pi^0}$	$d\sigma/d\Omega$ [nb/sr]	Error
18.0	-3.158555	2.461388
22.0	3.829901	0.649180
26.0	6.352371	0.359806
30.0	6.925347	0.270157
34.0	8.665576	0.251786
38.0	8.816647	0.212124
42.0	9.102090	0.183004
46.0	9.792498	0.170316
50.0	10.806607	0.168195
54.0	11.487394	0.159660
58.0	11.808391	0.154082
62.0	13.042291	0.157657
66.0	13.425307	0.154754
70.0	14.163608	0.157547
74.0	13.953354	0.154054
78.0	14.543733	0.155743
82.0	14.405385	0.151030
86.0	14.793108	0.154199
90.0	14.707913	0.151707
94.0	14.914462	0.154710
98.0	14.248819	0.153387
102.0	14.071208	0.153681
106.0	13.275181	0.149994
110.0	12.803766	0.147412
114.0	12.141401	0.147263
118.0	10.684770	0.138061
122.0	10.279558	0.138775
126.0	9.925456	0.140902
130.0	8.413100	0.132539
134.0	8.157009	0.137479
138.0	6.770568	0.127755
142.0	5.943742	0.126419
146.0	5.511180	0.129227
150.0	5.253549	0.143523
154.0	4.352528	0.146299
158.0	3.698416	0.148770
162.0	3.718930	0.173392
166.0	2.986003	0.191659
170.0	2.317463	0.224354
174.0	2.344242	0.293492
178.0	2.106594	0.486152

### 6.4.3 Incoming Photon Beam Energy: 425-475 MeV

$\theta_{\pi^0}$	$d\sigma/d\Omega$ [nb/sr]	Error
26.0	2.847045	0.609818
30.0	4.664948	0.328244
34.0	5.023357	0.237729
38.0	4.922780	0.198619
42.0	5.359921	0.166728
46.0	5.456799	0.147099
50.0	6.234809	0.146478
54.0	6.728998	0.141172
58.0	6.888905	0.135623
62.0	7.187350	0.134337
66.0	7.427698	0.132229
70.0	7.507149	0.129384
74.0	8.351537	0.134566
78.0	8.221821	0.132559
82.0	8.276936	0.130275
86.0	8.435212	0.132149
90.0	8.558666	0.133397
94.0	8.465711	0.135064
98.0	8.103614	0.132332
102.0	7.611805	0.126440
106.0	7.339770	0.126237
110.0	7.289553	0.128378
114.0	6.734951	0.123949
118.0	6.286826	0.124896
122.0	6.193163	0.125114
126.0	5.065037	0.117051
130.0	4.907217	0.119565
134.0	4.339602	0.116911
138.0	3.547098	0.110175
142.0	3.195859	0.108707
146.0	2.674951	0.107182
150.0	2.323723	0.108653
154.0	1.951913	0.115538
158.0	1.731569	0.127802
162.0	1.100516	0.128833
166.0	1.064340	0.144189
170.0	0.924818	0.153055
174.0	1.136666	0.246956
178.0	0.388504	0.474774

## 6.5 The $\gamma p \rightarrow \pi^0 p \gamma'$ Angular Differential Cross Sections

### 6.5.1 Incoming Photon Beam Energy: 325-375 MeV

$\theta_{\gamma'}$	$d\sigma/d\Omega$ [nb/sr]	Error
22.0	0.342665	0.405447
26.0	0.937029	0.536751
30.0	-	-
34.0	2.956564	0.447766
38.0	3.137693	0.406921
42.0	2.439045	0.427289
46.0	2.368673	0.379937
50.0	2.659284	0.392482
54.0	3.846711	0.475738
58.0	3.746019	0.402385
62.0	3.252911	0.396046
66.0	4.175306	0.465387
70.0	3.082943	0.382913
74.0	3.465259	0.431933
78.0	4.331956	0.405744
82.0	3.883583	0.381958
86.0	4.140391	0.460344
90.0	4.664680	0.397561
94.0	5.126211	0.406323
98.0	5.467396	0.474585
102.0	4.570306	0.362850
106.0	4.770404	0.385682
110.0	4.728652	0.372396
114.0	5.290533	0.405339
118.0	4.764798	0.373949
122.0	4.612568	0.362443
126.0	5.104189	0.404748
130.0	4.085971	0.355017
134.0	4.805500	0.412999
138.0	3.336971	0.328387
142.0	3.354429	0.401098
146.0	3.043403	0.363188
150.0	4.830089	0.512004
154.0	2.734231	0.388642
158.0	3.140617	0.450919
162.0	4.616192	0.704183
166.0	0.955086	0.757853
170.0	0.000000	0.000000
174.0	0.000000	0.000000
178.0	0.000000	0.000000

### 6.5.2 Incoming Photon Beam Energy: 375-425 MeV

$\theta_{\gamma'}$	$d\sigma/d\Omega$ [nb/sr]	Error
18.0	0.000000	0.0
22.0	0.066747	0.290945
26.0	-	-
30.0	-	-
34.0	4.103082	0.657644
38.0	2.844495	0.343652
42.0	2.353740	0.444009
46.0	3.833827	0.430165
50.0	3.761008	0.362944
54.0	4.515597	0.463739
58.0	4.335626	0.380796
62.0	4.575809	0.333364
66.0	4.950734	0.407410
70.0	5.601154	0.359848
74.0	5.218860	0.378806
78.0	5.214504	0.352810
82.0	5.341051	0.334877
86.0	5.610169	0.363125
90.0	6.494011	0.366246
94.0	5.527290	0.345822
98.0	7.526270	0.432533
102.0	6.660925	0.339532
106.0	7.603405	0.402338
110.0	6.755700	0.393003
114.0	6.844010	0.356613
118.0	6.569590	0.406446
122.0	7.078671	0.359243
126.0	6.467384	0.376168
130.0	6.186337	0.335322
134.0	6.452903	0.351091
138.0	5.648019	0.310455
142.0	5.690062	0.345332
146.0	5.737855	0.282160
150.0	6.466969	0.344047
154.0	4.180969	0.268828
158.0	4.383939	0.294447
162.0	3.028747	0.260368
166.0	0.103356	0.450517
170.0	0.000000	0.000000

**6.5.3 Incoming Photon Beam Energy: 425-475 MeV**

$\theta_{\gamma'}$	$d\sigma/d\Omega$ [nb/sr]	Error
30.0	1.327688	1.128918
34.0	4.812112	0.924487
38.0	2.732079	0.318673
42.0	3.599528	0.432757
46.0	3.457452	0.485618
50.0	3.389864	0.396961
54.0	3.731428	0.517524
58.0	5.276358	0.510997
62.0	5.344331	0.463564
66.0	4.732671	0.503896
70.0	5.286328	0.525402
74.0	5.967266	0.463872
78.0	7.667381	0.567339
82.0	7.487016	0.508010
86.0	6.246807	0.466218
90.0	8.723881	0.614183
94.0	7.308816	0.499222
98.0	6.65214	0.488351
102.0	8.213705	0.539976
106.0	6.911283	0.480535
110.0	7.176756	0.505894
114.0	7.392661	0.458979
118.0	8.478398	0.581115
122.0	7.345364	0.486114
126.0	6.772181	0.506912
130.0	6.741456	0.468556
134.0	6.527283	0.486282
138.0	6.195521	0.499766
142.0	7.007532	0.566042
146.0	5.554235	0.491251
150.0	6.402558	0.591633
154.0	4.306798	0.472012
158.0	3.540533	0.543183
162.0	2.456278	0.435763
166.0	0.722116	0.854420
170.0	2.012064	1.422744

## 6.6 The $\gamma p \rightarrow \pi^0 p \gamma'$ Energy Differential Cross Sections

### 6.6.1 Incoming Photon Beam Energy: 325-375 MeV

$E_{\gamma'}$	$d\sigma/dE$ [nb/MeV]	Error
37.5	1.356463	0.051641
42.5	0.954500	0.046719
47.5	0.801079	0.044735
52.5	0.644821	0.042974
57.5	0.480296	0.039803
62.5	0.424020	0.039500
67.5	0.378791	0.038046
72.5	0.387241	0.037702
77.5	0.272812	0.034051
82.5	0.294254	0.036168
87.5	0.214358	0.033473
92.5	0.208411	0.032246
97.5	0.173140	0.030493
102.5	0.168138	0.028874
107.5	0.147158	0.028886
112.5	0.124573	0.026481
117.5	0.151932	0.027407
122.5	0.050992	0.022500
127.5	0.042663	0.019923
132.5	0.042988	0.017709
137.5	0.048168	0.017366
142.5	0.026240	0.013438
147.5	0.039099	0.012802
152.5	0.015436	0.010055
157.5	0.001305	0.006439



**6.6.2 Incoming Photon Beam Energy: 375-425 MeV**

$E_{\gamma'}$	$d\sigma/dE$ [nb/MeV]	Error
37.5	1.251278	0.046906
42.5	1.095760	0.044712
47.5	0.887160	0.043213
52.5	0.831951	0.042248
57.5	0.743927	0.041238
62.5	0.757536	0.041426
67.5	0.685032	0.040961
72.5	0.581954	0.040293
77.5	0.434724	0.036528
82.5	0.443156	0.036782
87.5	0.417448	0.036958
92.5	0.392706	0.035610
97.5	0.319222	0.033738
102.5	0.346225	0.033148
107.5	0.211326	0.030137
112.5	0.255329	0.029236
117.5	0.201003	0.027149
122.5	0.226978	0.026892
127.5	0.169161	0.024736
132.5	0.166340	0.023388
137.5	0.130811	0.020757
142.5	0.133301	0.019981
147.5	0.114851	0.018154
152.5	0.101684	0.016342
157.5	0.076847	0.014055
162.5	0.056765	0.012157
167.5	0.052982	0.011221
172.5	0.044165	0.009812
177.5	0.022643	0.008034
182.5	0.019522	0.005695
187.5	0.010016	0.004524
192.5	0.002551	0.002777

### 6.6.3 Incoming Photon Beam Energy: 425-475 MeV

$E_{\gamma'}$	$d\sigma/dE$ [nb/MeV]	Error
37.5	0.780766	0.041035
42.5	0.666932	0.040353
47.5	0.505991	0.037122
52.5	0.627103	0.040220
57.5	0.629121	0.040270
62.5	0.627586	0.040607
67.5	0.601110	0.042039
72.5	0.629429	0.042545
77.5	0.484723	0.041110
82.5	0.582818	0.044268
87.5	0.555984	0.044199
92.5	0.438363	0.043610
97.5	0.474608	0.044025
102.5	0.387331	0.042760
107.5	0.439319	0.046211
112.5	0.414838	0.043573
117.5	0.393788	0.043099
122.5	0.383504	0.042447
127.5	0.345849	0.040116
132.5	0.285202	0.038247
137.5	0.293756	0.036358
142.5	0.243904	0.033963
147.5	0.243820	0.031904
152.5	0.209003	0.030214
157.5	0.228682	0.028334
162.5	0.185423	0.025494
167.5	0.173495	0.023429
172.5	0.109389	0.019768
177.5	0.092240	0.018576
182.5	0.093962	0.017611
187.5	0.072775	0.015687
192.5	0.067432	0.013494
197.5	0.056363	0.012129
202.5	0.032626	0.010352
207.5	0.033822	0.008933
212.5	0.005181	0.006699

## 6.7 The R-ratio Differential Cross Sections

### 6.7.1 Incoming Photon Beam Energy: 325-375 MeV

$E_{\gamma'}$	R	Error
37.5	0.965176	0.036745
42.5	0.770943	0.037735
47.5	0.724052	0.040434
52.5	0.644821	0.042974
57.5	0.526478	0.043630
62.5	0.505562	0.047096
67.5	0.488058	0.049021
72.5	0.536180	0.052202
77.5	0.403972	0.050421
82.5	0.464016	0.057034
87.5	0.358637	0.056002
92.5	0.368727	0.057050
97.5	0.322973	0.056881
102.5	0.329809	0.056638
107.5	0.302805	0.059439
112.5	0.268310	0.057037
117.5	0.341848	0.061665
122.5	0.119635	0.052789
127.5	0.104196	0.048658
132.5	0.109124	0.044953
137.5	0.126905	0.045752
142.5	0.071655	0.036697
147.5	0.110531	0.036191
152.5	0.045119	0.029392
157.5	0.003940	0.019440

### 6.7.2 Incoming Photon Beam Energy: 375-425 MeV

$E_{\gamma'}$	R	Error
37.5	1.286035	0.048209
42.5	1.278386	0.052164
47.5	1.158236	0.056417
52.5	1.201707	0.061025
57.5	1.177885	0.065294
62.5	1.304645	0.071345
67.5	1.274921	0.076233
72.5	1.163908	0.080586
77.5	0.929826	0.078129
82.5	1.009411	0.083780
87.5	1.008832	0.089315
92.5	1.003582	0.091005
97.5	0.860125	0.090904
102.5	0.980971	0.093920
107.5	0.628108	0.089575
112.5	0.794356	0.090956
117.5	0.653261	0.088234
122.5	0.769204	0.091134
127.5	0.596764	0.087262
132.5	0.609914	0.085755
137.5	0.497807	0.078992
142.5	0.525797	0.078814
147.5	0.468976	0.074130
152.5	0.429332	0.069000
157.5	0.335138	0.061294
162.5	0.255444	0.054708
167.5	0.245778	0.052051
172.5	0.211009	0.046877
177.5	0.111330	0.039498
182.5	0.098692	0.028792
187.5	0.052026	0.023500
192.5	0.013605	0.014810

**6.7.3 Incoming Photon Beam Energy: 425-475 MeV**

$E_{\gamma'}$	R	Error
37.5	1.241974	0.065276
42.5	1.204262	0.072864
47.5	1.022424	0.075010
52.5	1.401949	0.089916
57.5	1.541698	0.098683
62.5	1.672843	0.108239
67.5	1.731487	0.121091
72.5	1.948361	0.131695
77.5	1.604630	0.136091
82.5	2.054648	0.156061
87.5	2.079563	0.165317
92.5	1.733850	0.172489
97.5	1.979233	0.183594
102.5	1.698527	0.187512
107.5	2.020944	0.212577
112.5	1.997500	0.209810
117.5	1.980789	0.216792
122.5	2.011499	0.222637
127.5	1.888343	0.219032
132.5	1.618513	0.217048
137.5	1.730204	0.214147
142.5	1.489010	0.207340
147.5	1.540907	0.201629
152.5	1.365799	0.197443
157.5	1.543553	0.191247
162.5	1.291421	0.177561
167.5	1.245645	0.168215
172.5	0.808895	0.146181
177.5	0.701911	0.141357
182.5	0.735217	0.137795
187.5	0.585080	0.126119
192.5	0.556620	0.111390
197.5	0.477363	0.102724
202.5	0.283340	0.089903
207.5	0.300997	0.079502
212.5	0.047217	0.061056



# Bibliography

- [A204] A2-Collaboration: *wwwa2.kph.uni-mainz.de: Experiments/ Standard Instruments/ Tagger Calibration.*
- [Ali00] T.M. Aliev, A. Özpineci and M. Savci: *Magnetic Moments of  $\Delta$  Baryons in Light Cone QCD Sum Rules*, Nucl. Phys. A 678 (200) 443-454.
- [Ami92] M. El Amiri, G. López Castro, and J. Pestieau,  *$\Delta^{++}$  Contribution to the Elastic and Radiative  $\pi^+p$  Scattering*. Nucl. Phys. A543 673, 1992.
- [Ann97] J.R.M. Annand, I. Anthony, A.H. Sibbald, K. Livingston: *ACQU Data acquisition system for nuclear physics, 3rd Edition*. University of Glasgow, 1997.
- [Ann05] J.R.M. Annand: *Data Analysis within AcqRoot Framework* University of Glasgow, 2005.
- [Ahr00] J. Ahrens et al., Phys. Rev. Lett. 84, 5950 (2000).
- [Aul99] K. Aulenbacher et al., Proceedings PST, International Workshop on polarized Sources and Targets, Erlangen, p. 288-292, 1999.
- [Aud91] G. Audit et al.: *DAPHNE: a Large-Acceptance Tracking Detector for the Study of Photoreactions at intermediate Energies*. Nuclear Instruments and Methods in Physics Research Section A, 301:473-481, 1991.
- [Aul00] K. Aulenbacher et al. Private Communication, 2000.
- [Ber04] K. Berger, R. F. Wagenbrunn and W. Plessas: *Covariant baryon charge radii and magnetic moments in a chiral constituent-quark model*, Phys. Rev. D 70, 094027 (2004).
- [Bec99] R.Beck et al. : *Measurement of the E2/M1 Ratio in the  $N \rightarrow \Delta$  Transition using the reaction  $p(\gamma \rightarrow, p)\pi^0$*  Phys. Rev.Lett. 78, 606, 1997.

- [But94] M.N. Butler, M.J. Savage and R.P. Springer: *Electromagnetic Moments of the Baryon Decuplet*, Phys. Rev.D 49 3459, 1994.
- [Chi05] Wen-Tai Chiang, M.Vanderhaeghen, Shin Nan Yang, D. Drechsel: *Unitary model for the  $\gamma p \rightarrow \text{gamma}\pi^0 p$  Reaction and the Magnetic Dipole Moment of the  $\Delta^+(1232)$* , Phys. Rev. C 71, 015204 (2005).
- [Cla97] M. Clajus: *Recent Changes to the Crystal Ball Simulation Code, Crystal Ball Note CB-97-004*, Department of Physics and Astronomy, University of California, Los Angeles, 1997B.
- [Dow06] E. Downie: *Radiative  $\pi^0$  Photoproduction in the Region of the  $\Delta^+$  Resonance*. PhD thesis, Glasgow University, 2006.
- [Dre01] D. Drechsel, M. Vanderhaeghen: *Magnetic dipole moment of the  $D^+(1232)$  from the  $\gamma p \rightarrow \pi^0 p \gamma'$  reaction*, Phys. Rev. C 64 065202 (2001).
- [Dre04] P. Drexler: *Entwicklung und Aufbau der neuen TAPS-Elektronik*, Doktorarbeit, II. Physikalisches Institut der Justus-Liebig-Universität Giessen, Januar 2004.
- [Fis96] K. G. Fissum et al., Phys. Rev. C 53, 1278 2, 1996.
- [Gab93] A. Ruth Gabler: *Ansprechverhalten des Detektorsystems TAPS für monochromatische Photonen im Energiebereich  $E = 50 - 780$  MeV*, Diplomarbeit, Universität Gießen, 1993.
- [Hor06] M. Horras: *Walk Correction for the Crystal Ball Detector at A2*, Projektarbeit, Universität Basel, 2006.
- [Kot01] M. Kotulla: *Experiment zur Bestimmung des magnetischen Moments der  $\Delta^+(1232)$  Resonanz*, Dissertation, II. Physikalisches Institut der Justus-Liebig-Universität Giessen, 2001.
- [Kram07] D. Krambrich: *Aufbau des Crystal Ball-Detektorsystems und Untersuchung der Helizitätsasymmetrie in  $\gamma p \rightarrow p\pi^0\pi^0$* . Dissertation, Universität Mainz, 2007.
- [Lei92] D.B. Leinweber, T. Draper and R.M. Woloshyn: *Decuplet Baryon Structure from Lattice QCD*, Phys. Rev. D 46 3067, 1992.
- [Leu01] R. Leukel: *Photoproduktion neutraler Pionen am Proton mit linear polarisierten Photonen im Bereich der  $\Delta^+(1232)$  Resonanz*, Dissertation, Institut für Kernphysik der Johannes Gutenberg-Universität Mainz, 2001



- [Kim98] H.C. Kim, M. Praszalowicz and K. Goeke: *Magnetic Moments of the SU(3) Decuplet Baryons in a Chiral Quark-Solution Model*, Phys. Rev. D 57 2859, 1998.
- [Mac07] A.I. Machavariani and Amand Faessler *Ward-Takahashi identity, soft photon theorem and the magnetic moment of the  $\Delta$  resonance*. nucl-th/0703080, March 2007.
- [MAI03] D. Drechsel, S.S. Kamalov, L. Tiator: *A Unitary Iso-bar Model for Pion Photo- and Electroproduction on the Nucleon*, <http://www.kph.uni-mainz.de/MAID>
- [MCo96] M. MacCormick et al., Phys. Rev. C 53, 41, 1996.
- [McP64] D. A. McPherson et al., Phys. Rev. 136, B1465, 1964.
- [Ols59] Olsen, H. und L.C. Maximon. Phys. Rev., 114:887, 1959.
- [Pas03] Vladimir Pascalutsa and Daniel R. Phillips: *Chiral effective field theory of (1232) and Compton scattering*, Phys. Rev. C 67, 055202, 2003.
- [Pas05] Vladimir Pascalutsa and Marc Vanderhaeghen: *Magnetic Moment of the  $\Delta(1232)$  Resonance in Chiral Effective-Field Theory*, Phys. Rev. Lett. 94, 102003, 2005.
- [Pas07] Vladimir Pascalutsa and Marc Vanderhaeghen: *Chiral Effective-Field Theory in the  $\Delta(1232)$  Resonance region: II. radiative pion photoproduction*, arXiv:0709.5583v2 [hep-ph], October 2007.
- [Roc05] Roca, L.: *Helicity asymmetries in double pion photoproduction on the proton*. Nucl. Phys., A748:192 205, 2005.
- [Rei99] A. Reiter: *Entwicklung und Test eines ortsauslösenden Detektors für die Photonenmarkierungsanlage*. Diplomarbeit, Institut für Kernphysik der Johannes Gutenberg-Universität Mainz, 1999.
- [SAI06] R.A. Arndt, I.I. Strakovsky, R.L. Workman: *Scattering Analysis Interactive Dialin*, <http://gwdac.phys.gwu.edu/>.
- [Sch93] F. Schlumpf: *Magnetic Moments of the Baryons Decuplet in a relativistic Quark Model*, Phys. Rev. D 48 9, 1993.
- [Schu08] S.Schumann: *Strahlungsbegleitete  $\pi^0$  Produktion am Proton*, Dissertation, Universität Bonn, 2008.

- [Tho04a] A. Thomas: *The Crystal Ball Hydrogen (Deuterium) Target Manual*, Juni 2004. <http://wwwa2.kph.uni-mainz.de/A2/> ! Experiments ! Crystal Ball ! Target Manual.
- [Tio02] Tioukine, V.: *Spin Manipulation at MAMI C*. In: *Proceedings of EPAC 2002*, Paris, France, 2002.
- [Unv04] M. Unverzagt: *Energie-Eichung des Crystal Ball-Detektors am MAMI*, Diplomarbeit, Institut für Kernphysik der Johannes Gutenberg-Universität Mainz, 2004.
- [Zeh08] F. Zehr: *in preparation*, PhD thesis, Institut für Physik, Universität Basel, 2008.

## CURRICULUM VITAE

### Personalien

Name: Bénédicte Boillat  
Adresse: Bachofenstrasse 1, 4053 Basel  
Geboren am: 21. Februar 1978  
Ort: Genf  
Nationalität: Schweiz

### Schule & Studium

1984 – 1988 Primarschule in Delémont (JU)  
1988 – 1993 Sekundarschule in Delémont (JU)  
1993 – 1996 Gymnasium in Porrentruy (JU)  
*Matura Typus C*  
1996 – 1998 Pharmaziestudium an der Universität Basel  
*1. Propedeutikum*  
1998-2003 Physikstudium an der Universität Basel  
März 2003 Abschluss der Diplomprüfungen mit Hauptfach *Physik*, Nebenfach *Mathematik*, Wahlfach *Chemie*  
03.2003-10.2003 Diplomarbeit im Bereich Kernphysik bei Prof. Dr. Ingo Sick, Physikalisches Institut der Universität Basel  
12.2003 - 03.2008 Doktorarbeit im Bereich Kern- und Teilchenphysik Bei Prof. Dr. Bernd Krusche, Physikalisches Institut der Universität Basel Im Rahmen der *A2-* und *CBTAPS-Collaboration*.

September 30, 2009